Anion Photoelectron Spectroscopy

by

Django H. Andrews

B.A., University of Oregon, 1999

A thesis submitted to the

Faculty of the Graduate School of the

University of Colorado in partial fulfillment

of the requirements for the degree of

Doctor of Philosophy

Physical Chemistry

2006

This thesis entitled:

Anion Photoelectron Spectroscopy

Written by Django H. Andrews

has been approved for the Physical Chemistry program by

_____

W. Carl Lineberger

_____

Veronica M. Bierbaum

Date: _____

The final copy of this thesis has been examined by both the signatories, and we find that both the content and the form meet acceptable presentation standards of scholarly work in the above mentioned discipline.

Andrews, Django H. (Ph.D. Physical Chemistry)

Anion Photoelectron Spectroscopy

Thesis directed by Professor W. Carl Lineberger

This thesis presents the results of anion photoelectron spectroscopy experiments conducted on three classes of anions. One class is that of heteronuclear coinage metal diatomic molecules. These include AgO^-, AuO^-, AuS^-, CuH^-, and CuD^-. The photoelectron spectra of these molecules are characterized by short vibrational progressions in transitions to the ground electronic states and confident assignments of the electronic state origins and electron affinities. The photoelectron spectra of these molecules measured for the first time the electron affinities of the corresponding neutral molecules. Frank-Condon simulation of the observed ground state vibrational structure coupled with observation of a well characterized excited state allowed for the assignment of the anion equilibrium bond lengths for AgO^-, CuH^-, and CuD^-. Because no excited electronic states were observed in the photoelectron spectra of AuO^- and AuS^-, only the magnitude of the bond length change between the anion and the neutral molecules was assigned. Observation of hot-bands in the photoelectron spectra allowed for the first assignment of anion harmonic vibrational frequencies for AgO^- and AuS^-. In addition, a predicted, yet previously unobserved, $^3\Sigma^+$ excited electronic state of CuD and CuH was observed in the photoelectron spectra of CuD^- and CuH^-.

The second class of molecules studied was that of copper anion complexes. These included Cu^-CD_3OD, $CuCD_3O^-$, CuH_2^-, and CuD_2^-. The photoelectron spectra of these complexes are characterized by extended vibrational progressions in the transitions to nearly all observed electronic states. These extended vibrational progressions are the product of large geometry changes between the anion and neutral complexes. The geometry change

between the anion and neutral of CuH_2 and CuD_2 is also very severe, as the anions are linear and the neutrals are bent. The spectra are dominated by a short vibrational progression in the symmetric stretch mode which allows determination of the electron affinities of CuH_2 and CuD_2.

The photoelectron spectra of two related organic compounds were also taken. Photoelectron spectra of the 1,2,3-triazolide anion were recorded and show signatures of strong vibronic coupling of the low lying electronic states of the neutral. Still, the vibrational origin of transitions to the ground electronic state of the neutral allowed for easy assignment of the neutral electron affinity. Combination of the measured electron affinity with the gas phase acidity measured elsewhere allowed for determination of the N-H bond dissociation energy of the parent molecule 1H-1,2,3-triazolide. In addition, the heat of formation of the 1,2,3-trizolyl radical was also determined. It was also found that, under the experimental source conditions used in these experiments, about 40% of the 1,2,3-triazolide anions ring open to form the E-iminodiazomethide anion, the structure of which was assigned on the basis of a simulation of the measured photoelectron spectrum. The simulation also allowed assignment of several normal mode frequencies of the anion and neutral.

Contents

Figures

Tables

—————————

Introduction to Anion Photoelectron Spectroscopy

—————————

1.1   Anion Photoelectron Spectroscopy Overview

Anion photoelectron spectroscopy is a powerful tool to study the geometries, vibrational modes, thermochemistry, and electronic structure of anions and neutrals.[1] Through the use of different ion sources, laser souces, and electron kinetic energy measurement techniques anion photoelectron spectroscopy has been applied to a wide range of systems.[1] These include atoms,[2] organic molecules,[3] metal-ligand systems,[4] and a wide variety of clustered systems.[5-8] As explained below, the electron affinity, vibrational frequencies, and electronic term energies of the photodetached neutral are readily measured in an anion photoelectron experiment. Often vibrational (and occasionally electronic) levels of the anion may be measured as well. Theoretical geometry and frequency calculations are often employed to simulate[9] a photoelectron spectrum in order to make spectral assignments and to identify the photoelectron signal carrier.

In an anion photoelectron spectroscopic experiment, a beam of molecular or atomic anions is prepared and laser light is used to photodetach electrons from the anion beam. The kinetic energy of the photodetached electrons is measured and, when combined with the photon energy of the photodetachement laser, the binding energy of the electrons to the anion is obtained. The process is simply defined for a molecular anion in equation 1.1 below.

$$AB^- + h\nu = AB + e^-(eKE) \qquad (1.1)$$

Here AB^- is the molecular anion energy, $h\nu$ is the photon energy, AB is the energy of the photodetached neutral, and $e^-(eKE)$ is the photodetached electron kinetic energy (eKE). It is clear from equation 1.1 that, given a well defined molecular anion energy state and a narrow

bandwidth photon source, measuring the electron kinetic energies directly gives the difference in energy between the initial anion state(s) and the final neutral state(s). This energy is the electron binding energy (eBE) of the anion and is found by subtracting the electron kinetic energy from the photon energy. Given sufficient photon energy, transitions to excited vibrational and electronic energy levels of the neutral may be accessed. The process is diagrammed in Figure 1.1 below. While the process is a direct photodetachment, it may be thought of as absorption of the photon by the anion followed by concurrent molecular relaxation and photoejection.
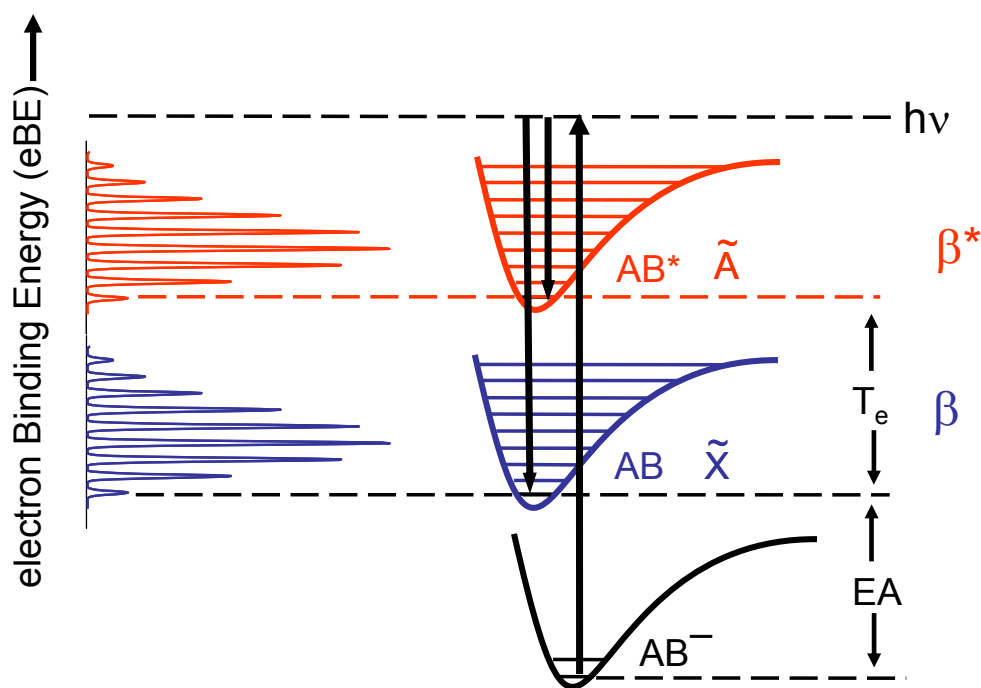
Figure 1.1   Schematic diagram depicting processes and energies present in photoelectron spectra.

In Figure 1.1 the electronic and vibrational features of the anion are represented by the potential labeled AB^-. The "absorption" process is depicted by the large upward pointing arrow, while relaxation to various vibronic energy levels and photoejection (as well as the eKE) is represented by the downward pointing arrows. The electron affinity of the neutral is

the energy of the $0 - 0$ transition between the anion and neutral and is labeled as "EA" in Figure 1.1. If energetically accessible, term energies for excited neutral electronic states may be directly measured and are represented by "T_e" in Figure 1.1.

1.2 Selection Rules

Since the electronic states of the neutral are accessed by removal of an electron, the only electronic selection rule is that the spin quantum number must change by ½ (i.e., removal of an electron from a doublet spin state will produce either a singlet or triplet spin state). The transition moment (**M**) for photodetachement, within the Frank-Condon approximation, is given by equation 1.2 below.[1]

$$\mathrm{M} = C \times \left| \left\langle \Psi''(Q'') \middle| \Psi'(Q') \right\rangle \right|^2$$
(1.2)

Here $\psi''(Q'')$ is the vibrational wavefunction of the initial anion state and $\psi'(Q')$ is the vibrational wavefunction of the final neutral state, both as a function of the normal vibrational coordinates Q. Note that only transitions to and from totally symmetric vibrational modes (or even quanta of non-totally symmetric modes) are allowed.

1.3 Frank-Condon Profiles

The transition moment is extremely sensitive to differences between vibrational normal coordinates between the anion and neutral and determines the profile for vibrational progressions observed in photoelectron spectra. This effect is demonstrated for a homonuclear diatomic molecule in Figure 1.2 below. For a homonuclear diatomic molecule, the normal vibrational coordinate is the bond length of the anion or neutral. Figure 1.2 displays the results of simulated[9] photoelectron transitions with increasing change in normal vibrational coordinates (bond length) between the anion and neutral.
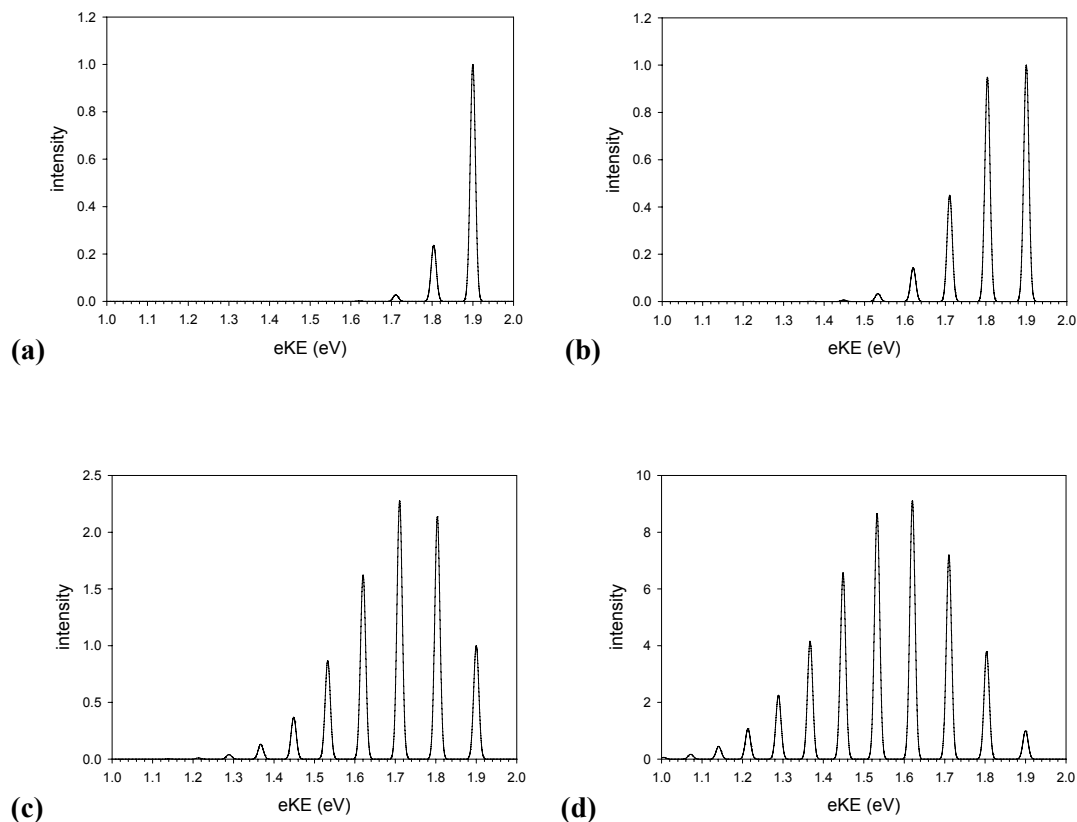
Figure 1.2   Simulated diatomic photoelectron spectra showing the effect of bond length change between the anion and neutral on the spectral profile. The spectra presented were simulated with a (a) 5%, (b) 10%, (c) 15%, and (d) 20% change in bond length between the anion and the neutral.

Notice that the vibrational progression increases with the change in bond length, as does the most likely final vibrational state of the neutral. By simulating the photoelectron spectrum the change in the normal vibrational coordinates between the anion and the neutral can be inferred. Matching the vibrational profiles and identifying transitions to different electronic states by examination of the β parameters[10] leads to accurate vibrational and electronic state assignments in the spectrum.

1.4 Anisotropy (β) Parameters

Electrons photodetached from orbitals of different symmetry (hence leading to different electronic states of the neutral) have different angular distributions defined[10] by equation 1.3 below.

$$I(\theta) = \frac{\sigma_o}{4\pi}\left(1 + \beta P_2\left(\cos\theta\right)\right)$$
(1.3)

Here $I(\theta)$ is the photoelectron intensity as a function of the angle between the electric field of the laser and the electron collection direction. σ_0 is the total photodetachment cross-section, P_2 is the second Legendre polynomial, and β is the anisotropy parameter. For atomic photodetachment, $\beta = 2$ for detachment from an s orbital, $\beta = 0$ for near threshold detachment from a p orbital, and negative β values result from photodetachment from p and d orbitals not near threshold, with a minimum value of -1. For molecular photodetachment, β is not as well defined. However, electrons photodetached from Σ orbitals will have positive β values and electrons photodetached from Π and Δ orbitals will have negative β values. Thus measurement of the anisotropy parameters for features in a photoelectron spectrum will help to assign transitions to different electronic states of the neutral.

1.5 Thesis Overview

This thesis contains photoelectron spectra of several different types of molecules taken with two different photoelectron spectrometer systems. The first system is cw, contains a flowing afterglow ion source, and employs a hemispherical electron kinetic energy analyzer. The second system is pulsed, employs a supersonic expansion ion source, and uses the velocity map imaging technique to measure the electron kinetic energies. Both of these systems are described in detail in chapter 2, along with theoretical methods for photoelectron spectral simulations.

As part of a research program conducted by the Lineberger and Bierbaum groups to learn about the thermodynamics of the azoles (five-membered nitrogen-containing rings), the pulsed photoelectron imaging spectrometer was used to study the 1,2,3-triazolide anion. These results are presented in chapter 3. Iminodiazomethide, a concurrently produced ring-opened isomer of 1,2,3-triazolide, was studied using both photoelectron spectrometers. These results are presented in chapter 4.

As part of a research program conducted with undergraduate physical chemistry students, the hemispherical analyzer photoelectron spectrometer was used to record the photoelectron spectra of AgO^-, AuO^-, and AuS^-. The results of the metal oxide and sulfide experiments are presented in chapter 5.

Photoelectron spectra of CuH^- and CuH_2^- recorded with the photoelectron imaging spectrometer are presented in chapter 6. The electronic structure and vibrational frequencies of the CuH molecule are compared frequently with high level theoretical calculations to better treat relativistic effects and transition metals in general. The electron affinity of this molecule has not been reported previously, as well as a low lying triplet state which is dark to traditional absorption or emission spectroscopies. Both are reported here for the first time.

In order to better understand time resolved photodetachment-photoionization (PDPI) studies of the Cu^- CD_3OD system, photoelectron spectra of Cu^- CD_3OD and $CuCD3O^-$ were recorded using the photoelectron imaging spectrometer. The results of this study are presented in chapter 7. A summary of the experimental results is given in chapter 8.

In order to protect the low pressure detection region of the photoelectron imaging spectrometer, a smart power backup vacuum interlock system was designed and built. The details of the design, interlock flow chart, and interlock program code are presented in appendix A.

References for Chapter I

[1]   K. M. Ervin and W. C. Lineberger, in *Advances in Gas Phase Ion Chemistry*, edited by N. G. Adams and L. M. Babcock (JAI Press, Greenwich, 1992), Vol. 1, pp. 121.

[2]   T. Andersen, H. K. Haugen, and H. Hotop, *Journal of Physical and Chemical Reference Data* **28** (6), 1511 (1999).

[3]   S. J. Blanksby and G. B. Ellison, *Accounts of Chemical Research* **36** (4), 255 (2003).

[4]   G. J. Rathbone, T. Sanford, D. Andrews, and W. C. Lineberger, *Chemical Physics Letters* **401** (4-6), 570 (2005).

[5]   J. Ho, K. M. Ervin, and W. C. Lineberger, *Journal of Chemical Physics* **93** (10), 6987 (1990).

[6]   F. Misaizu, K. Tsukamoto, M. Sanekata, and K. Fuke, *Surface Review and Letters* **3** (1), 405 (1996).

[7]   A. Nakajima, T. Taguwa, K. Nakao, K. Hoshino, S. Iwata, and K. Kaya, *Surface Review and Letters* **3** (1), 417 (1996).

[8]   D. Radisic, S. J. Xu, and K. H. Bowen, *Chemical Physics Letters* **354** (1-2), 9 (2002).

[9]   K. M. Ervin, T. M. Ramond, G. E. Davico, R. L. Schwartz, S. M. Casey, and W. C. Lineberger, *Journal of Physical Chemistry A* **105** (48), 10822 (2001).

[10]   J. Cooper and R. N. Zare, *Journal of Chemical Physics* **48**, 942 (1968).

_____

Hemispherical Analyzer and Velocity Map Imaging Methods

_____

2.1   Anion Photoelectron Spectrometers Overview

Two types of photoelectron spectrometers were used in the course of the experiments conducted here. The main difference between the two is the method used to measure the kinetic energy of photodetached electrons. One instrument employs a hemispherical analyzer while the other uses a velocity map imaging system. Because the hemispherical analyzer system detects only a small fraction (1/1000) of the photodetached electrons, the anion source and laser system must produce large amounts of anions and photons, respectively. The velocity map imaging system, in contrast, detects nearly all photodetached electrons, and thus requires only a moderate amount of anions and photons. The resolution of the velocity map imaging detector is approximately 2% of the electron kinetic energy, while the resolution of the hemispherical analyzer is about 10 meV for all electron kinetic energies.

Historically the two instruments were designed to study very different systems. The hemispherical analyzer instrument was initially designed to photodetach electrons from atomic negative ions. It has been used in recent years to study many small organic anions, through the use of rational gas phase reaction anion synthesis, as well as metal based anions. The velocity map imaging instrument was originally designed for time resolved photo-fragmentation studies of cluster anions, with the velocity map imaging capabilities only recently added. The hemispherical analyzer instrument uses a laser system with a maximum photon energy of 3.531 eV, while the velocity map imaging laser system can currently produce photon energies up to 5.904 eV. The resolution of the mass spectrometers used to select an anion mass are greatly different as well: the hemispherical analyzer can separate masses with a 1 amu difference up to 35 amu, while the velocity map imaging instrument can

separate masses with 1 amu difference up to several hundred amu. The anion temperatures are also very different between the two systems. The velocity map imaging instrument uses a pulsed supersonic expansion source which can produce cluster anions with temperatures as low as tens of Kelvin. Conversely, the hemispherical analyzer instrument uses a high pressure (~ 500 mtorr) source which produces anions with typical temperatures between 200 K and 400 K.

The advantages of the velocity map imaging instrument, then, are superior mass resolution, higher photon energies, and production of large anion clusters. The advantages of the hemispherical analyzer instrument are constant energy resolution, thermalized anions, and rational anion synthesis. The remainder of this chapter is devoted to description and methodology of both instruments. The hemispherical analyzer instrument is described in sections 2.2 – 2.7, while the velocity map imaging instrument is described in sections 2.8 – 2.13. Theoretical calculations and spectral simulation methods used to aid the interpretation of the photoelectron spectra are presented in section 2.14.

2.2 Hemispherical Analyzer Photoelectron Spectrometer Overview

The hemispherical analyzer photoelectron spectrometer and methodology used in the experiments presented here have been described in great detail previously,[1-4] thus a moderate description is given here. The apparatus is diagrammed in Figure 2.1. The spectrometer consists of an anion source coupled to a high pressure reaction flow tube to create anions via rational gas phase ion reactions. This region is described in section 2.3. Anions are extracted into a low pressure beam formation and mass selection region, which is presented in section 2.4. The mass-selected anion beam is crossed with a fixed frequency laser beam producing photoelectrons. The kinetic energy of the photoelectrons is measured by a hemispherical energy analyzer which is described in section 2.5. Section 2.6 describes the continuous wave

external build-up cavity laser system. Data manipulation and analysis are presented in section 2.7.
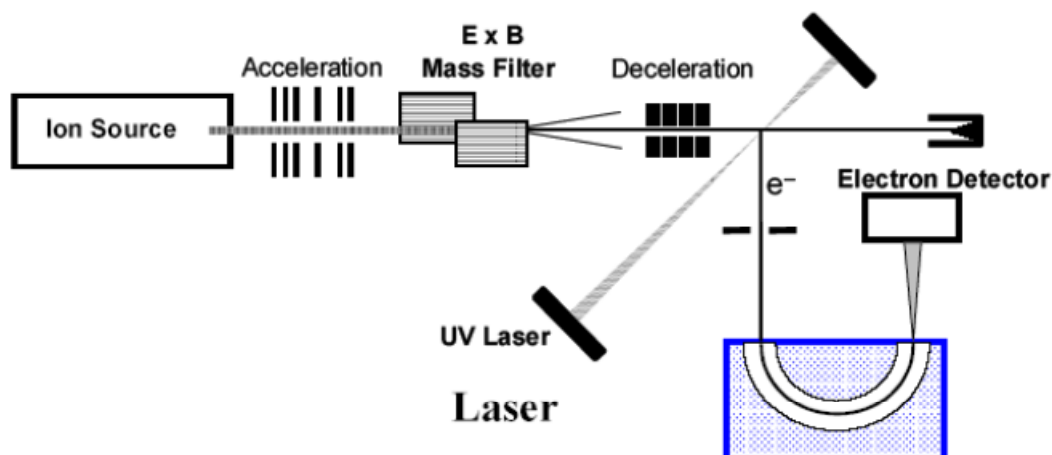
Figure 2.1   Hemispherical energy analyzer photoelectron spectrometer.

2.3   Hemispherical Analyzer Instrument Ion Sources

Two anion sources were used in the hemispherical analyzer photoelectron spectrometer experiments presented here. A cold cathode dc sputter source was used to produce AuS^-, AgO^- and AuO^-, while a microwave discharge source was used to produce 1,2,3-triazolide and its ring-opened isomer iminodiazomethide.

The cold cathode dc sputter source is described first and diagrammed in Figure 2.2. The source consists of a high purity metal rod which is biased up to –3,000 volts with respect to chamber ground in a helium and argon atmosphere of ∼ 500 mtorr. The rod is biased by an electrically ballasted dc power supply, with the ballast consisting of a 100 kΩ resistor and 4 H inductor in series. High purity helium seeded with 10% − 15% argon is introduced just above the metal rod, the flow of which is regulated by a Tylan flow controller with a flow of

6-7 standard liters per minute. The strong electric field between the metal rod and the chamber walls ionizes the argon atoms creating Ar^+. The Ar^+ ions are then accelerated into the metal rod, sputtering off metal atoms and clusters. The rod holder is cooled by a flow of water through the stainless steel tube to which the holder is attached (see Figure 2.2). In addition, the sputter source region is externally wrapped with a copper cooling water line. A glass cylinder around the rod holder prevents arcing between the holder and the chamber walls. Metal oxide (sulfide) anions are formed by adding a trace amount of O_2 (CS_2) to the He/Ar mixture.
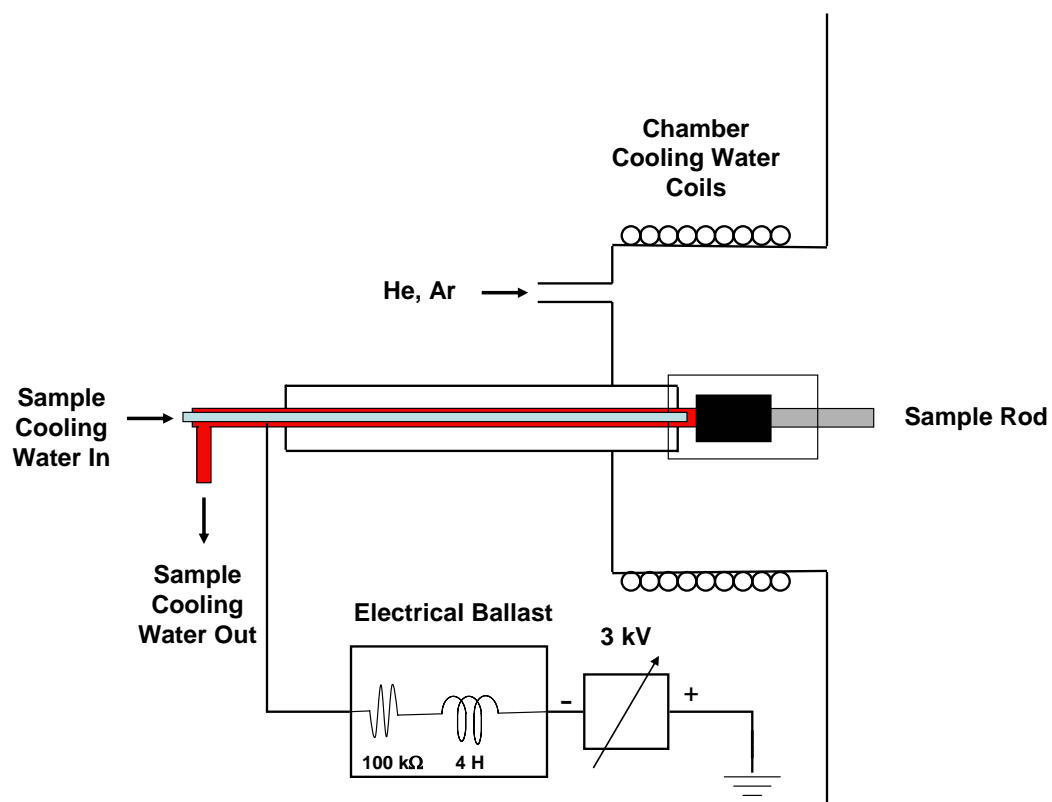
Figure 2.2   DC sputter ion source for the hemispherical analyzer instrument.

The microwave discharge ion source used to produce 1,2,3-triazolide and its ring-opened isomer iminodiazomethide is diagrammed in Figure 2.3. Atomic oxygen anion is formed by passing a trace of oxygen in 500 mtorr of helium through a resonant microwave cavity which is tuned with a ceramic tuning rod. A flow rate of 6 -7 standard liters per minute is maintained by a Tylan flow controller. The discharge is created by ignition with a Tesla coil and maintained by a 2.45 GHz microwave generator. Electrons from the Tesla coil are accelerated in the microwave field and create a plasma containing high energy He^+ metastable ions and O^- ions, as well as other neutrals and ions. The O^- anion is created via slow electron dissociative attachment to molecular oxygen.

Upon exiting the microwave discharge region the plasma enters a flowing afterglow ion reaction region. The ions may be reacted with neutral reagents introduced into the flow tube via two moveable neutral ring inlets. To create 1,2,3-triazolide and iminodiazomethide anions, O^- was first reacted with methane introduced via the first ring inlet to form HO^-. Gaseous 1H-1,2,3-triazole is introduced through the second ring inlet by flowing helium over a liquid sample of 1H-1,2,3-triazole (97%, Aldrich). The HO^- abstracts a proton from 1H-1,2,3,-triazole to form both 1,2,3,-triazolide and iminodiazomethide.
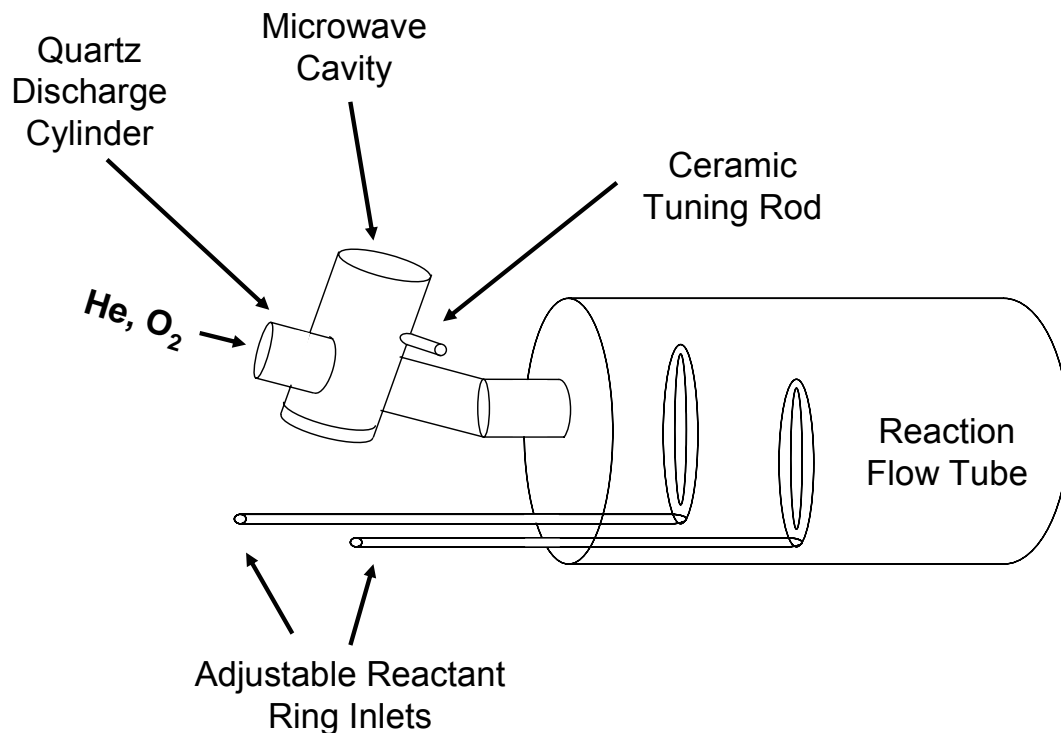
Figure 2.3   Microwave discharge ion source for the hemispherical energy analyzer instrument.

After formation the anions are thermalized by collisions with the helium buffer gas in the flow tube. The anions have a temperature which is near the temperature of the flow tube walls, usually around 300 K. The flow tube is surrounded by a jacket which may be filled with liquid nitrogen to cool the flow tube, reducing the anion temperature to near 200 K.

2.4   Hemispherical Analyzer Instrument Ion Beam Formation and Mass Selection

The flow tube is terminated by a 1 mm orifice in a nosecone which is biased near +1 volt to gently extract negative ions into a lower pressure (0.1 mtorr) region. This region consists of a series of lenses and deflectors for ion beam formation, acceleration, mass selection, and deceleration. In addition, apertures allow for differential pumping of this region, which is diagrammed in Figure 2.4. The left side of Figure 2.4 shows the successively decreasing pressure of this region, while the right side indicates the ion beam

potential in each section. Lenses are denoted by L's, deflectors by D's, quadrupoles by Q's, and apertures by A's.

The first set of lenses (L1 – L3) acts as an einzel lens, which accelerates and focuses the beam. The ions are accelerated and deflected both horizontally and vertically by a set of deflectors labeled D1. They then pass through an aperture (A1) and through another set of accelerating lenses (L3, L4) before being steered through deflector set D2. The ions then pass a second accelerating einzel lens set (L4 – L6), and are steered through a 10° bend in the instrument by deflector set D3. The purpose of the 10° bend is to remove any neutrals which may have formed after the ions were extracted through the nosecone. The ion beam potential after D3 is 735 eV and the beam is focused and deflected through aperture A2 by quadrupole lens Q1. Current induced by ions which impact A2 rather than traveling through the aperture is measured by an electrometer and is minimized to ensure a large portion of the ion beam passes through A2.
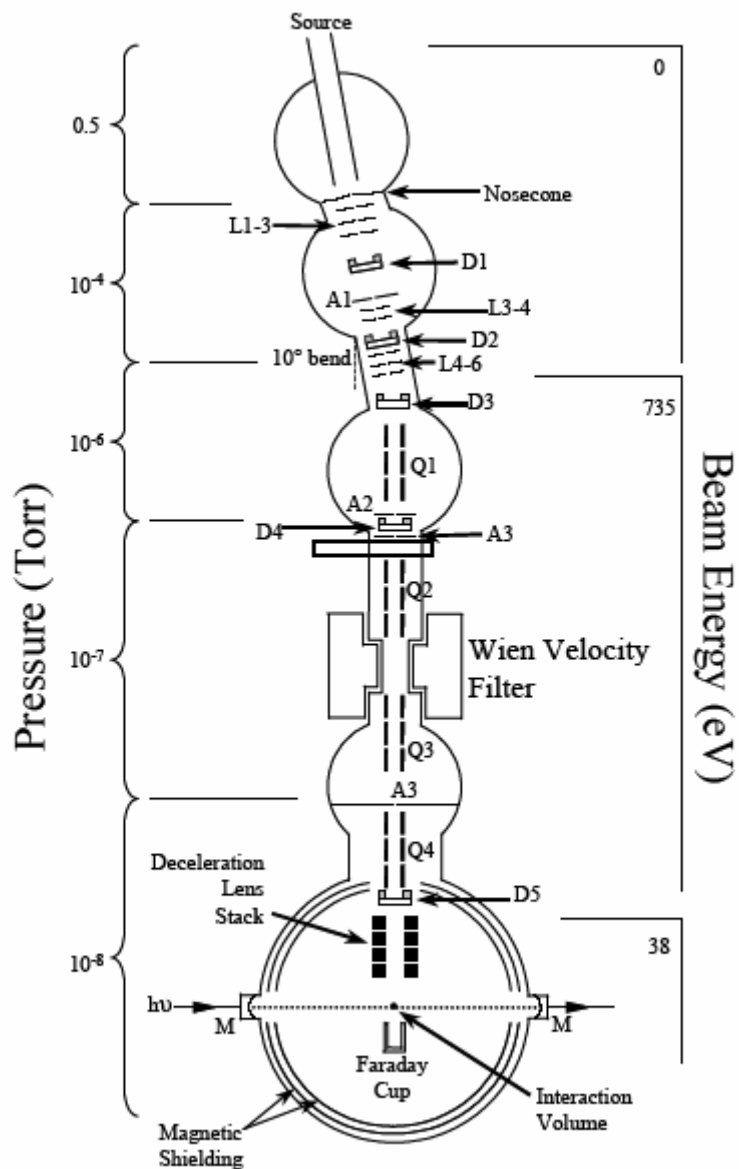
Figure 2.4 Hemispherical analyzer instrument ion optics, mass selection, and laser interaction regions. L = lens, D = deflector, A = aperture, and Q = quadrupole.

Once through A2, the ions pass a deflector set (D4), aperture (A3), and quadrupole (Q2). A gate valve between A3 and Q2 separates the chamber and allows the high pressure ion formation section of the chamber to be vented without risk to the low pressure detection region. The ions are separated according to their velocities by a velocity filter. This filter

consists of perpendicular electric and magnetic fields, each of which exerts a force on the ions. The electric field deflects the ions according to their charge, while the magnetic field deflects ions according to their velocity in a direction perpendicular to their velocity. Since all ions have the same energy (735 eV), they are distributed according to their masses by velocity. The magnetic field strength is tuned such that the electric and magnetic forces acting upon the anion of interest are equal and opposite, resulting in zero deflection. Anions of higher or lower velocity (mass) are deflected out of the beam path. The velocity filter has a mass resolution of $m/\Delta m \cong 35$.

After mass selection, the ion beam is focused and deflected by quadrupole Q3 through aperture A3. Quadruple Q4 and deflector D5 steer the ions into a set of deceleration lenses where the beam energy is reduced to 38 eV, greatly reducing the ion velocity. The ion beam passes through the laser interaction region after which the beam is terminated by a Faraday cup. The current on the cup is measured by an electrometer, with typical beam currents ranging from several picoamps to several nanoamps.

2.5   Hemispherical Analyzer Instrument Photoelectron Detection

The laser-anion interaction region of the chamber also serves as the first lens element of the photoelectron hemispherical kinetic energy analyzer. Photoelectrons produced in the laser-ion volume have velocities in all directions. An aperture with 5° half-angle cone acceptance angle sits below the anion-laser beam plane. The analyzer consists of acceleration and magnification input sets of lenses, a hemispherical analyzer, output acceleration and magnification lenses, and position sensitive electron detector with are diagrammed in Figure 2.5.

The hemisphere consists of an inner and outer sphere with static electron transmission energy. Electrons input into the analyzer with this energy will pass through, while those at higher or lower energies will impact either the inner or outer hemisphere. The

function of the input stack is to accelerate the sampled photoelectrons to the transmission energy and focus the beam onto the entrance of the hemisphere. The elements labeled V_{IR}, V1, and V2 in Figure 2.5 act as a three element accelerating and focusing lens, while V2, V3, and V_{HC} act as a three element focusing lens. The elements labeled V_{HC} are Herzog correctors which compensate for stray electric fields created by the hemisphere. Once through the analyzer, the electrons are accelerated (V_{HC}, V4) and focused (V4, V5, V6) onto a position sensitive detector.

The detector consists of five microchannel plates connected to a position sensitive resistive anode collector. A 3,400 volt potential is distributed evenly across the plates by an external voltage divider. A photoelectron spectrum is taken by changing the input stack electron acceleration voltage and measuring the photoelectron counts on the detector. The photoelectron counts are integrated for a short time (typically 1 second) per acceleration voltage and stored as X, Y data. The data for each acceleration voltage segment are added together using the often measured energy range of a single segment.

Photodetachment Volume

Position Sensitive Detector

V_{IR}

V6

Acceleration

V1

V5

Magnification

V2

V4

Magnification

V3

Acceleration

V_{HC}

Hemispherical Energy Analyzer
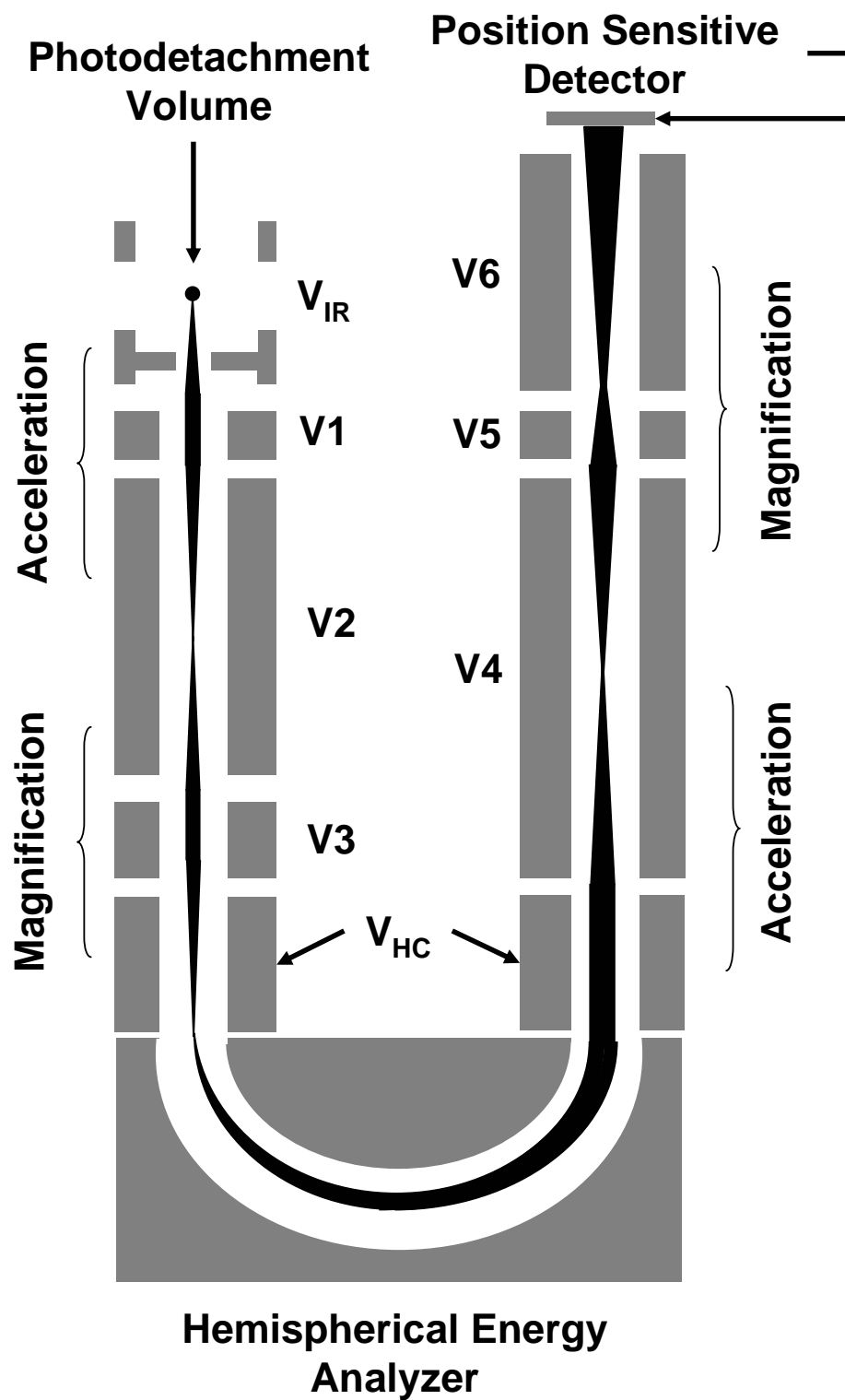
Figure 2.5   Hemispherical photoelectron kinetic energy analyzer.

2.6   Hemispherical Analyzer Instrument Laser System

The ultraviolet laser system used to produce either 363.8 nm or 351.1 nm laser radiation is presented in Figure 2.6. The system consists of a narrow line argon ion laser and external build-up cavity. The laser consists of an argon lasing medium excited by a 6 amp current.   The laser cavity is defined by an ultraviolet high reflecting mirror and output coupler. An etalon positioned in the laser cavity damps all but one longitudinal lasing mode below the lasing threshold. The remaining mode has a full width at half maximum in the kilohertz range. The power of the UV light which exits the laser cavity is typically 1 W, far below the amount needed to effectively conduct photoelectron spectroscopy experiments.

To increase the laser power, the interaction region of the chamber is used as an external build-up cavity. Laser light exits the lasing cavity and is relayed through a telescope by the mirrors labeled "M" in Figure 2.6. The beam then travels through an acousto-optical modulator (AOM in Figure 2.6), the first order output of which shifts the laser frequency by $55 - 85$ MHz. This first order output of the AOM is then steered through a half wave plate which allows for rotation of the laser polarization.   The laser beam then enters the photodetachment and electron detection portion of the vacuum chamber through the mirror labeled R1 in Figure 2.6. Mirror R1 is 99.6% reflective in the ultraviolet and together with mirror R2 (99.8% reflective) defines the external laser build-up cavity.

The 1 W laser light which enters the build-up cavity is increased to $150 - 200$ W inside the cavity by constructive interference. Build-up only occurs when the same mode which exits the laser is built-up in the cavity. Because small changes in either cavity length will change the resonance mode of the cavities, a system of electronics is in place to keep the two cavities in resonance. The light reflected from the external build-up cavity input mirror (R1) is monitored by a photodiode. The light reflected is at a minimum when the circulating power in the build-up cavity is at a maximum, thus decreases in the power measured by the

photodiode are preferred. There are three adjustments which can be made by the cavity resonance locking electronics. The first is the laser cavity length and is changed by moving the high reflecting optic (labeled "back mirror" in Figure 2.6) which is attached to a piezo electric mount. The input mirror of the external build up cavity (R1) is likewise held by a piezo electric mount in order to adjust the build-up cavity length. In addition, the frequency shift induced by the AOM can be changed to bring the frequency produced by the laser into resonance with the build-up cavity length.
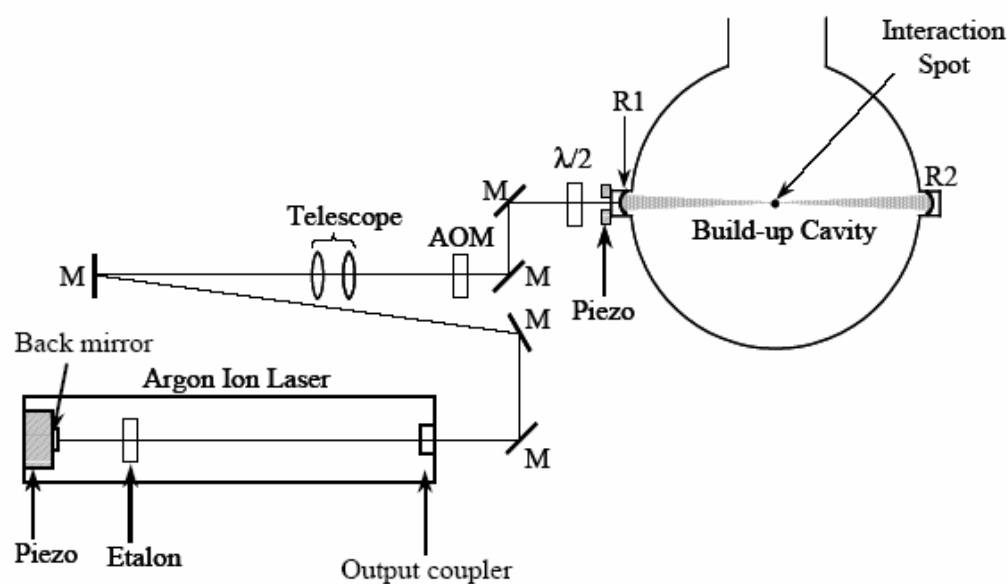
Figure 2.6   Hemispherical analyzer instrument ultraviolet continuous wave laser system.

2.7   Hemispherical Analyzer Methodology and Data Analysis

The raw photoelectron data are contained in segments. Each segment contains the number of counts in each pixel of the detector array (256 pixels per segment) for the given input lens voltages. The segments are tagged with the center experimental electron kinetic energy as derived from the well known[5] atomic transitions observed in the tungsten anion photoelectron spectrum. These segments are added using the PESCON program which

outputs the total number of photoelectron counts as a function of the electron kinetic energy. This energy scale is calibrated using a well known atomic transition observed in the atomic anion photoelectron spectrum, with atomic oxygen anion[6] being the most common. The width of each segment in eKE is also determined by observation of a known atomic transition. This width is used when adding the segments together. Also of importance is a small energy scale compression caused by the hemispherical analyzer. This compression is corrected for by routinely measuring the positions of the atomic transitions in the tungsten anion photoelectron spectrum mentioned above.

Spectral assignments of photoelectron spectra and theoretical calculations performed to aid these assignments are presented in section 2.13.

2.8   Velocity Map Imaging Photoelectron Spectrometer Overview

The photoelectron velocity map imaging apparatus is diagrammed in Figure 2.7. It has been described in some detail in several publications,[7-9] thus a moderate description is given here, with more attention paid to methodology and data analysis. The apparatus consists of a pulsed source region, Wiley-McLaren time-of-flight mass spectrometer,[10] and velocity map imaging photoelectron detection system.[11,12] Because the resolution of the spectrometer decreases with increasing electron kinetic energy, a nanosecond laser system tunable between 210 nm and 2,000 nm is used for photodetachment in order to resolve subtle spectral features. The description of the velocity map imaging photoelectron spectrometer is given in the following sections. Pulsed anion sources used in these experiments are described in section 2.9. Anion beam formation and mass separation are described in section 2.10. Section 2.11 describes the photoelectron velocity map imaging system and data collection methodology. The tunable nanosecond laser system is described in section 2.12, and data analysis procedures are described in section 2.13.
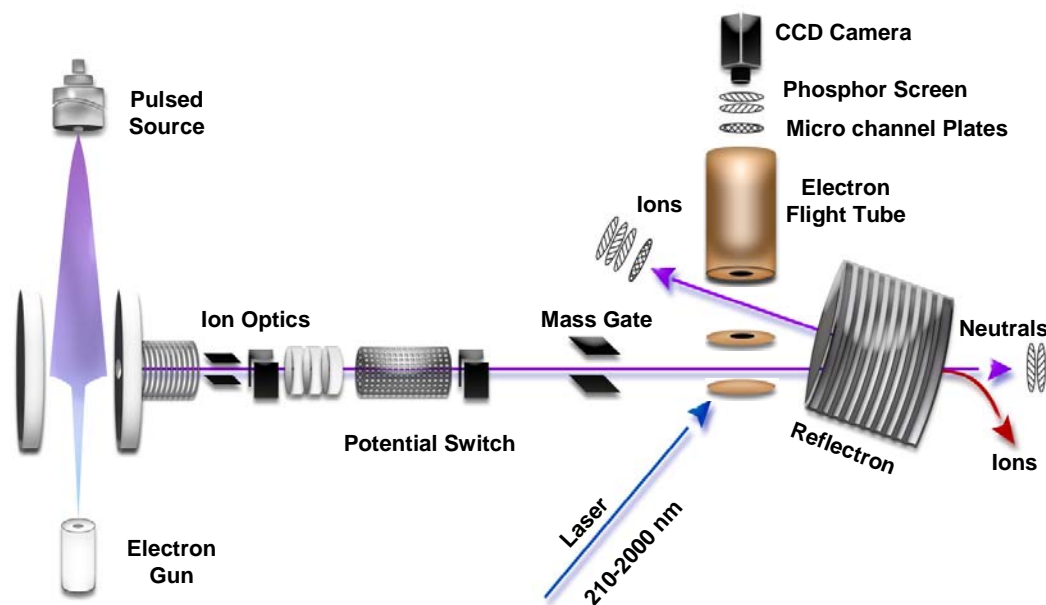
Figure 2.7   Photoelectron velocity map imaging spectrometer.

2.9   Velocity Map Imaging Instrument Ion Sources

Two ion source configurations were used during the course of the photoelectron velocity map imaging experiments presented here. The heart of both sources is a mixed-gas pulsed supersonic expansion. The expansion is formed when a gas mixture with stagnation pressure between 40 psi and 50 psi is expanded through a pulsed valve (General Valve Series 9, 0.8 mm aperture) into a low pressure region (base pressure 1×10^{-7} torr). The valve is driven by a General Valve IOTA ONE pulsed valve driver. The valve trigger, repetition rate, and open time are externally controlled by a high precision delay generator (Stanford Research Systems model DG535). The full experimental timing scheme is presented in section 2.11.

In the ion source configuration used to produce 1,2,3-triazolide, a gas mixture containing 10% O_2 and 20% CH_4 in argon is passed through a liquid sample of 1H-1,2,3-

triazole in a heated (85°C) scintillated glass bubbler. This mixture is brought to the pulsed

valve through heated (75°C) stainless steel tubing with a stagnation pressure of 45 psi. The

gas expansion is met collinearly (see Figure 2.7) by a 1 keV beam of electrons produced by a

home-built electron gun. The electron gun consists of a filament, anode, einzel lens, and

deflectors, and is located 30 cm from the pulsed valve face. Electrons are thermally emitted

by passing a current of 5 to 7 amps through a thoriated iridium filament (Electron

Technology, Inc.). Emitted electrons are extracted from the filament region and moderately

focused by an anode plate which is biased at -80 volts to -120 volts with respect to the

filament. Both the filament and anode plate are floated at 1 kV. The extracted electrons are

focused by an einzel lens, the first and third plates of which are held at ground potential,

while the middle plate is biased between 600 volts and 1100 volts. The electron beam is

steered into the gas expansion by a set of horizontal and vertical deflectors located beyond the

einzel lens, each set of plates typically having a potential difference of $0 - 50$ volts. The

electron beam is further directed to the center of the gas expansion by a 5 mm thick

samarium-cobalt magnetic annulus mounted to the front of the pulsed valve face. A

grounding clip attached to the valve face keeps the annulus and pulsed valve at chamber

ground.

The likely synthesic route to 1,2,3-triazolide is as follows. Slow secondary electrons

produced by interaction of the electron beam with argon dissociatively attach to O_2 forming

oxygen atom and O^-. The O^- then abstracts a hydrogen atom from CH_4 producing neutral

CH_3 and HO^-. The HO^- abstracts the N-H proton from 1H-1,2,3-triazole producing the 1,2,3-

triazolide anion.

The second source used in the experiments described here is a dc metal sputtering

source used to produce atomic metal ions with and without ligands. In this source, a large

potential difference is applied between two metal rods. One rod is a stainless steel anode,

while the other is the metal of interest (copper in these experiments). The stainless steel rod is connected directly to the chamber and the metal of interest is biased at $-1,000$ to $-3,000$ volts. The rods are held in a Macor block approximately 1 cm from the pulsed valve orifice and are separated by 0.5 to 2.0 mm. The Macor block has a 4 mm orifice in the center to allow the passage of gas from the pulsed valve and is attached to the valve face with stainless steel screws. A gas mixture of methanol seeded in argon is produced by passing argon over a liquid sample of neat spectroscopic grade (Aldrich) methanol held in a stainless steel cup. When this gas mixture passes between the rods a discharge is formed which ionizes the argon and the resulting Ar^+ is accelerated towards and impacts the negatively biased rod with sufficient force to sputter the metal. The process creates a plasma of neutral and ionic metal atoms and clusters. Metal-ligand anions are formed by three body reactions of metal anions, ligands, and a neutral collision partner (argon).

2.10   Velocity Map Imaging Instrument Ion Beam Formation and Mass Selection

Once formed, the plasma drifts 15 cm until the negative ions are transversely repelled by a pulsed electric field. The negative pulse is generated by a home-built module which takes a TTL pulse and dc high voltage as input and outputs a 2 ms (internally adjustable) less than 10 ns rise time pulse. The time delay between the pulsed valve opening and this repelling plate firing is set by maximizing the anion signal and is typically 300 μs to 800 μs. Negative ions are accelerated towards a ground aperture plate which defines the beginning of the second acceleration stage of the Wiley-McLaren time-of-flight mass spectrometer. The ground plate has a 3 mm aperture which defines the anion beam diameter and is in direct electrical contact with the vacuum chamber.

Once past this aperture plate, the anions enter the region marked "Ion Optics" in Figure 2.7. The first ion optical element is a 10 annuli acceleration region, with each annulus spaced by 0.43 cm with 2.54 cm diameter apertures. A dc voltage of $+2.3 - +2.5$ kV is

applied to the last plate and divided down to ground by 1 MΩ resisters, which accelerates the ions to this beam potential. All the elements labeled "Ion Optics" in Figure 2.7 are floated at this potential, including a three element einzel lens, horizontal deflectors, and vertical deflectors. The first and last elements of the einzel lens are held at the beam potential, while the middle element is held between +500 and +1100 volts. The voltage across the deflectors is 0 V – 135 V.

Beyond the einzel lens is an aperture plate (2.54 cm diameter aperture), also held at the beam potential, which defines the beginning of a 70 cm long potential switch[13] region. The switch is a cylindrical section which is electrically isolated from the ion optics and the chamber walls. When the anion repelling plate is fired, the potential of the cylindrical region is switched from ground up to the beam potential by a Directed Energy Inc I PVX-4140 pulse switcher. When the anion of interest is in the cylindrical region, the potential is rapidly switched to ground. This allows the chamber and ion optics elements beyond the switch region to be held at chamber ground and not the beam potential, as was previously the case. After the potential switch the ions are steered through a 1.5° bend in the chamber and into the entrance of a three element mass gate. The 1.5° bend removes any neutrals which have formed in the beam, while the mass gate selects the anion (or range of anions) of interest. The mass gate consists of three pairs of parallel horizontal plates between two aperture plates. These aperture plates, along with the first and third pairs of plates are held at chamber ground, while the middle pair of plates is held at a high voltage (typically 1 kV) and pulsed down to ground when the anion of interest is between the plates. See Figure 2.9 for the full experimental timing scheme. A gate valve between the 1.5° bend and the mass gate separates the ion production region from the ion and electron detection region.

The anions then travel through the photoelectron velocity map imaging region (described in section 2.11), reflectron (not used in the experiments described here), and

horizontal deflector before impinging on the front face of a microchannel plate detector. This detector consists of two impedance matched microchannel plates (Hamamatsu Corp. F4612-09 and Burle 32733) in a chevron configuration. The plates have a 2.0 cm diameter active area and the back plate is held at 1,600 volts for detection of anions and 1,800 – 1,950 volts for detection of neutral photoproducts. Anions may be deflected from the beam by applying a voltage of 200 – 1,000 volts on the horizontal deflector mentioned above. A mesh held at chamber ground sits before the front face of the MCPs and provides a field-free region for the anions just before the detector. Electrons emitted from the microchannel plates (typically 10^7 per particle) are collected by an anode plate biased at 200 volts above the back face of the MCPs. The anode signal is amplified by a Stanford Research Systems (model SR 240A) 350 MHz fast pre-amplifier which provides a maximum gain of 625. This signal is monitored on a 200 MHz oscilloscope (Tektronix model 2445B). A time-of-flight mass spectrum is recorded on this oscilloscope by monitoring the anion arrival time in reference to the high pulse of the anion repelling plate. These data are transferred from the oscilloscope to a PC via 3.5" floppy disk.

2.11   Velocity Map Imaging Instrument Photoelectron Detection

The photoelectron imaging spectrometer is based on the velocity map imaging technique developed by Parker and Eppink[11] and the design is a modified version of that employed by Sanov and coworkers.[12]   The electron imaging detector is comprised of a three element lens consisting of negatively biased repelling (V_1), ground (V_0), and positively biased extracting (V_2) 7.62 cm diameter 0.762 mm thick oxygen-free high-conductivity copper disks spaced by 2.54 cm. These electrodes are contained in a μ-metal (Magnetic Shielding Corp.) enclosure with 2.54 cm apertures for entrance and exit of the ion and laser beams, as well as ions directed towards the

off-axis detector by the reflectron (not used in the experiments reported here). In addition, there is a 2.54 cm aperture in the bottom of the enclosure to enable efficient pumping of the imaging region. The ground (V_0) and extracting plates (V_2) have 2.54 cm centered apertures, while the repelling plate has none. The extractor plate (V_2) is in electrical contact with, and defines the beginning of, a 15 cm long 7 cm diameter oxygen-free high-conductivity copper field free flight tube which is mounted on an 8" conflat flange. The inner surface of the electron flight tube is lined with four layers of 0.5 mm thick μ-metal to shield photoelectrons from the earth's magnetic field. At the end of the flight tube is a 4 cm active diameter imaging dual impedance matched chevron configured microchannel plate detector and P47 type phosphor screen coupled by a fiber optic bundle to a chamber window (Burle Electro-Optics, Inc.). This window is monitored by a 1280 x 1074 pixel CCD camera (LaVision 3LS, 6.7 μm x 6.7 μm pixel size) controlled by a desktop PC.

The anion of interest is photodetached approximately halfway between the repelling (V_1) and ground plates (V_0) of the electron imaging assembly. The repelling plate is pulsed high by an externally switched power supply (Directed Energy PVM-4210) ~ 10 μs prior to the arrival of the photodetachment laser pulse, with a pulse duration of ~ 50 μs. Since this repelling plate repels anions as well as electrons, it must be switched on well before the anions are near the plate. This is done to ensure that there is no dependence of the image size on the repelling plate being switched high. The V_2:V_1 voltage ratio (~ 3:1 for our configuration) must be optimized (also referred to as focused) for each laser photodetachment wavelength because the laser beam height changes with changing wavelength (regardless of laser source). Even

small changes in the laser height will significantly affect the optimum V_2:V_1 ratio, because there is a significant electric field gradient in the photodetachment region. A SIMION plot of the laser-ion interaction region is presented in Figure 2.8. The plot shows a high density of field lines in this region, confirming that a slight change in the laser position will significantly change the optimum V_2:V_1 voltage ratio. The ratio is optimized by monitoring the full-width-at-half-maximum of one, or more, well known electronic transitions in the photoelectron spectrum of an atomic anion. For the 1,2,3-triazolide spectra reported here, the $^3P_{3/2} \leftarrow {}^1S_0$ transition in the well known[14] photoelectron spectrum of F^- was used to determine the optimum V_2:V_1 ratio. For photoelectron imaging of copper based anions reported here, the transitions in the well known[15] photoelectron spectrum of atomic copper anion were used to find the optimum ratio. These transitions along with the corresponding electron binding energies are listed in Table 2.1. These atomic transitions are also used to calibrate the electron binding and electron kinetic energy scales (see section 2.13 for a thorough procedure). An atomic photoelectron spectrum is focused and recorded whenever the image size (V_1 and V_2) or laser (height or wavelength) is changed.

+86.9 volts
extraction plate

0.0 volts
ground plate

-20.0 volts
repelling plate
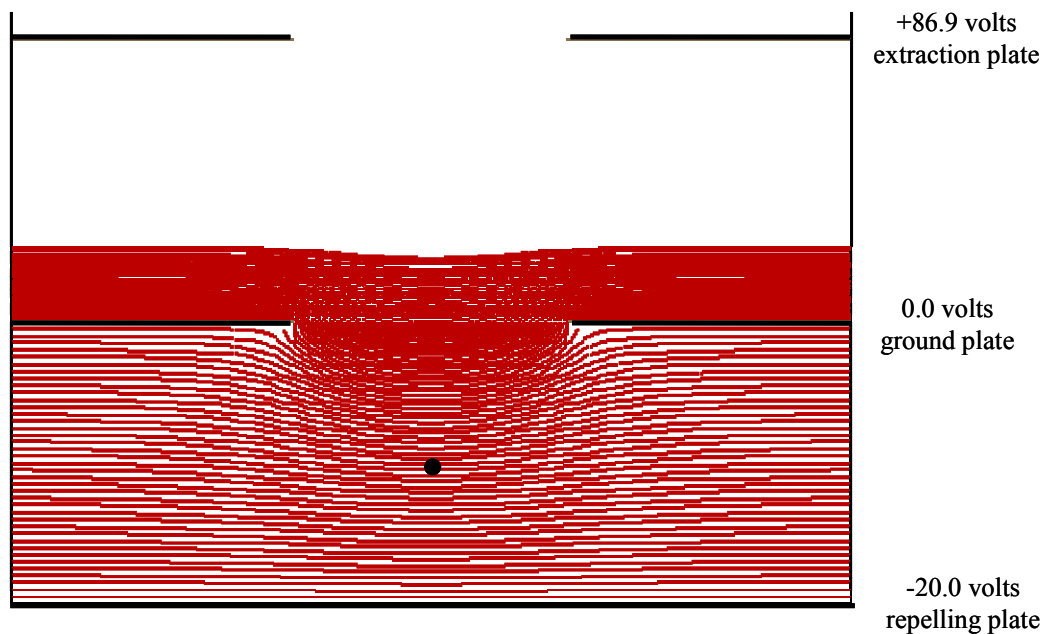
Figure 2.8 Potential field lines spaced at 0.5 volt computed using SIMION for the electron photodetachment region with typical imaging voltages. The black dot is the approximate laser-anion interaction region.

Table 2.1 Atomic copper photodetachment transitions used to focus and calibrate the velocity map imaging photoelectron spectrometer during copper based anion studies.

anion electronic state and tem symbol	neutral electronic configuration and term symbol	electron binding energy and photodetachment threshold
	[Ar] $3d^{10}$ $4s^1$, $^2S_{1/2}$	1.235 eV / 1004 nm
[Ar] $4s^2$ $3d^{10}$, $^1S_0$	[Ar] $3d^9$ $4s^2$, $^2D_{5/2}$	2.624 eV / 472.5 nm
	[Ar] $3d^9$ $4s^2$, $^2D_{3/2}$	2.677 eV / 463.2 nm

To decrease the background from non-photodetached electrons, the front face of the imaging detector is held at the flight tube voltage, while the back plate is pulsed from

1600 volts to 2000 volts above the front face by an externally switched high voltage pulse generator (Directed Energy PVM-4140). The high and low voltages for this pulse generator are externally provided. Switching of such a large voltage causes the voltage on the front face of the microchannel plates to ring, causing subtle potential differences between the MCP front face and the flight tube. These small differences in potential create in effect a transient electron lens which causes the image size to change with the MCP switch high time for a short duration (0 – 1 μs) after the MCPs are brought high. To allow for this ringing to subside, while still significantly reducing the background, the imaging MCPs are pulsed high for 2 μs beginning 1 μs before the arrival of the photodetachment laser pulse. The phosphor screen is held ~ 3,000 volts above the high voltage of the rear micro channel plate to increase the electron detection efficiency of the phosphor and is not pulsed. See Figure 2.9 for the experimental timing scheme.

The CCD camera is operated in a digital event counting mode. In this mode, the CCD is exposed for 50 – 1000 ms, after which the 2D peak position of each event over 25 analog counts is recorded. A typical data set contains 5,000 – 100,000 of these images which represent 125,000 to 5,000,000 laser shots and are summed. The CCD exposure time is set such that individual events do not overlap in a single image; otherwise the event counting macro may count these two events as a single event, effectively reducing the number of events counted per second.

Pulsed Valve [A = T_0 + (100 – 200) μs]

Ion Repelling Plate [B = T_0 + (400 – 900) μs]

Potential Switch (comes on with Ion Repelling Plate)

Mass Gate [C = B + (10 – 50) μs]

Electron Repeller (D ≈ B + 10 μs)

Laser Flash Lamp (E = F – 301.1 μs)

Laser Q-Switch (F ≈ ½ C + ½ Anion Inline Arrival Time)

Imaging MCP (G = F – 1 μs)

T_0
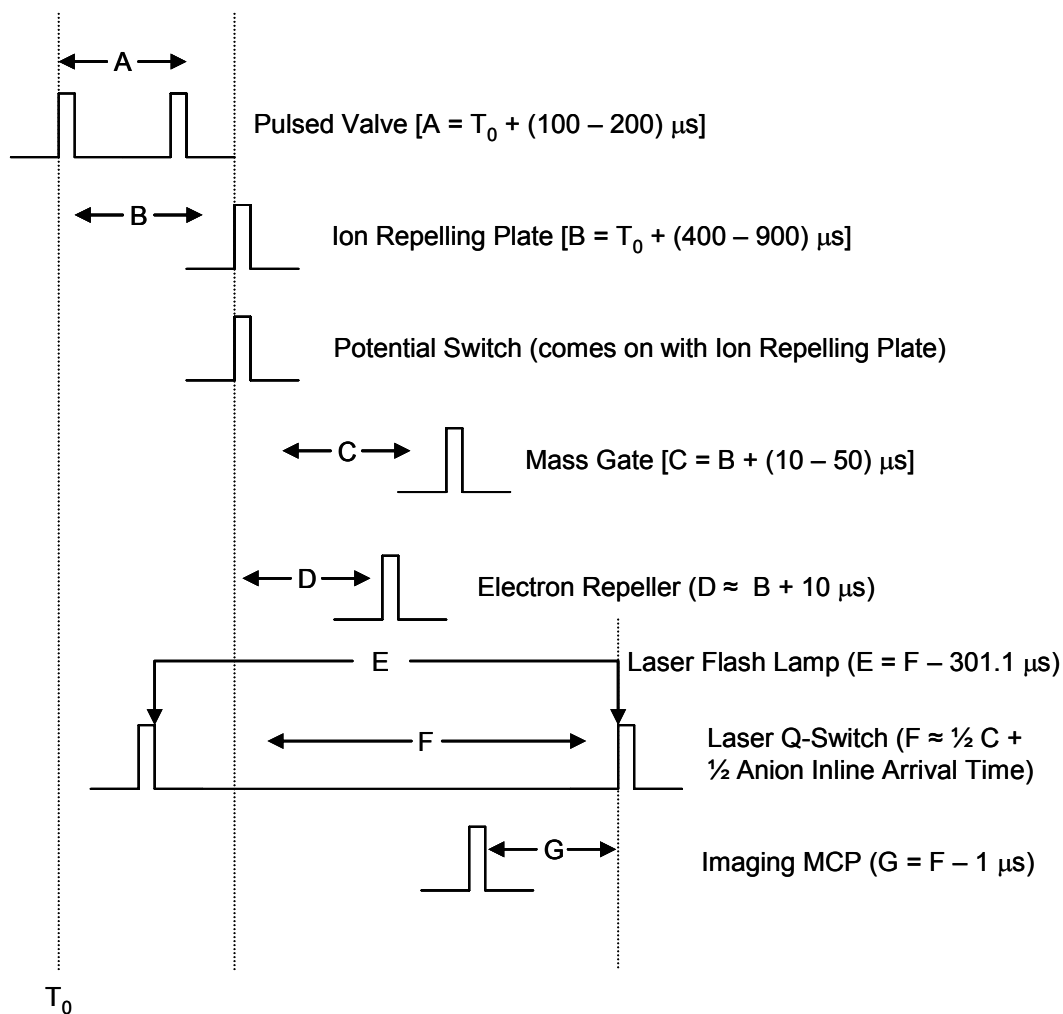
Figure 2.9   Photoelectron velocity map imaging instrument ion, laser, and detection timing scheme.

The resolution of the spectrometer is approximately 2% of the electron kinetic energy with the narrowest feature measured to date the above mentioned F^- transition with a full-width-at-half-maximum of 4 meV, as measured in the 355 nm photoelectron spectrum. It should be mentioned that due to the perpendicular orientation of the velocity map imaging detector relative to the ion propagation direction, the photoelectron images are subject to a Doppler shift due to the ion velocity. Figure 2.10 shows the effect of anion velocity on the ultimate resolution of the spectrometer. The top panel shows raw and BASEX reconstructed (see section 2.13 for a description of the image reconstruction method) images of Cu^- and the bottom panel contains similar images for F^-. Notice that the $\Delta eKE/eKE$ of the copper image is significantly smaller than that of the fluorine image. Also notice that the copper image is much more symmetric than the fluorine image. Because of this effect, one should always choose the heaviest calibration anion available.

(a)   Cu⁻ 600 nm (eKE = 0.831 eV, ΔeKE/eKE = 1.7)

(b)   F⁻ 325 nm (eKE = 0.413 eV, ΔeKE/eKE = 2.5)
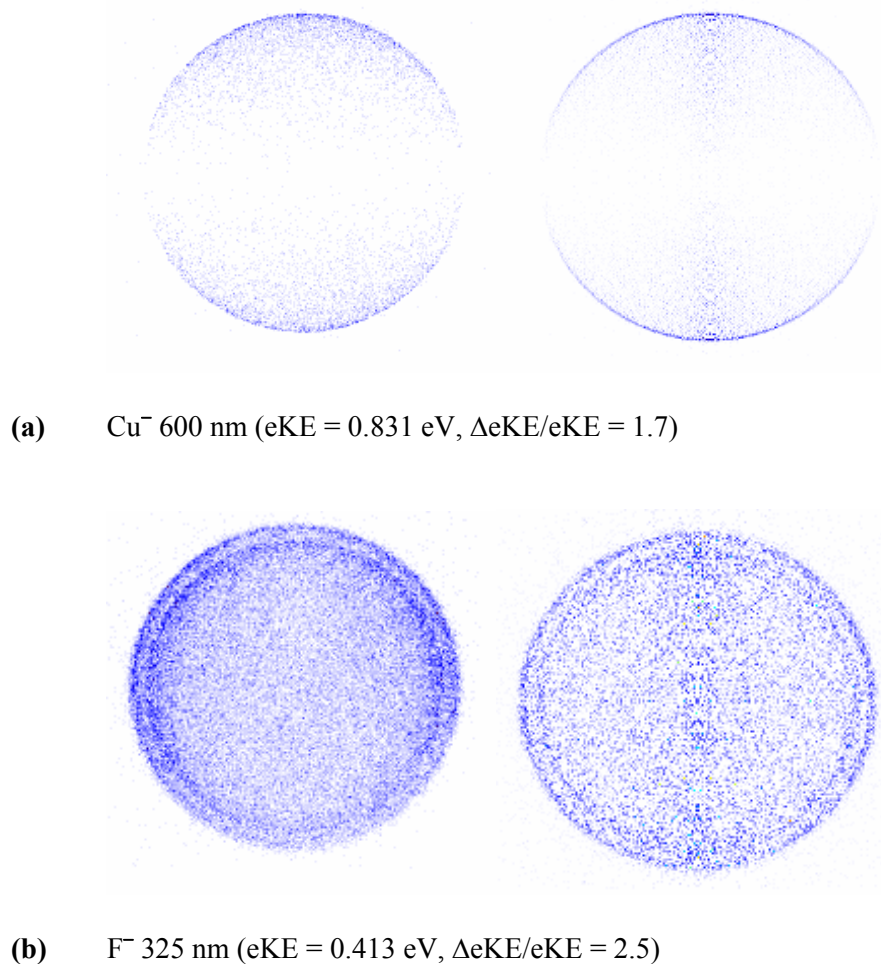
Figure 2.10   (a) Atomic copper and (b) fluoride anion raw (left) and reconstructed (right) photoelectron images showing effect of ion velocity on image quality and resolution.

2.12   Velocity Map Imaging Instrument Tunable Nanosecond Laser System

Fundamental laser radiation at 1064 nm with 0.1 – 100 Hz repetition rate and characteristic pulse duration of 3 ns is produced by a Coherent Infinity laser system which has been described in detail previously,[16] thus only a moderate description is given here. Initial 1064 nm pulses are created in a diode-pumped Nd:YAG prism in a ring resonator. These pulses are amplified by passing twice through each of two flashlamp-pumped Nd:YAG

rods, with the amount of amplification user defined. After amplification the 1064 nm pulses have pulse energies up to 600 mJ. These pulses undergo frequency doubling in an angle-tuned BBO crystal to produce 532 nm pulses with over 50% efficiency. These 532 nm pulses are combined with the residual 1064 nm pulses in another angle-tuned BBO crystal to produce 355 nm pulses, again with over 50% efficiency. At this point the Infinity is producing intense 1064 nm, 532 nm, and 355 nm laser pulses, which can be separated by use of appropriate laser mirrors. The residual 1064 nm pulses have not been used to date and are steered into an internal beam dump. The 355 nm pulses can be used for photodetachment, or to pump an optical parametric oscillator (OPO), the Coherent Infinity option is called "XPO". The 355 nm pulses undergo difference frequency mixing in a BBO crystal to produce signal and idler beams. The idler beam is tunable from 710 nm to 2,000 nm, while the signal beam is tunable between 410 nm and 710 nm. Wavelength tuning is accomplished through changing the angle of the BBO crystal used to produce both beams. A measured tuning efficiency curve for the signal beam is presented in Figure 2.11. Selection of signal or idler beam is done through selection of different sets of optics. Either signal or idler radiation may be doubled in an angle-tuned BBO crystal and compensator assembly, called the "SHG" package by Coherent. The doubled signal efficiency curve is presented in Figure 2.12. At 710 nm the OPO is producing both signal and idler beams; this condition is called the "degeneracy" of the OPO. As the BBO crystal angle is tuned away from degeneracy, it is still producing both signal and idler beams, both of which have large linewidths near degeneracy. The signal beam measured linewidth as a function of wavelength is presented in Figure 2.13.
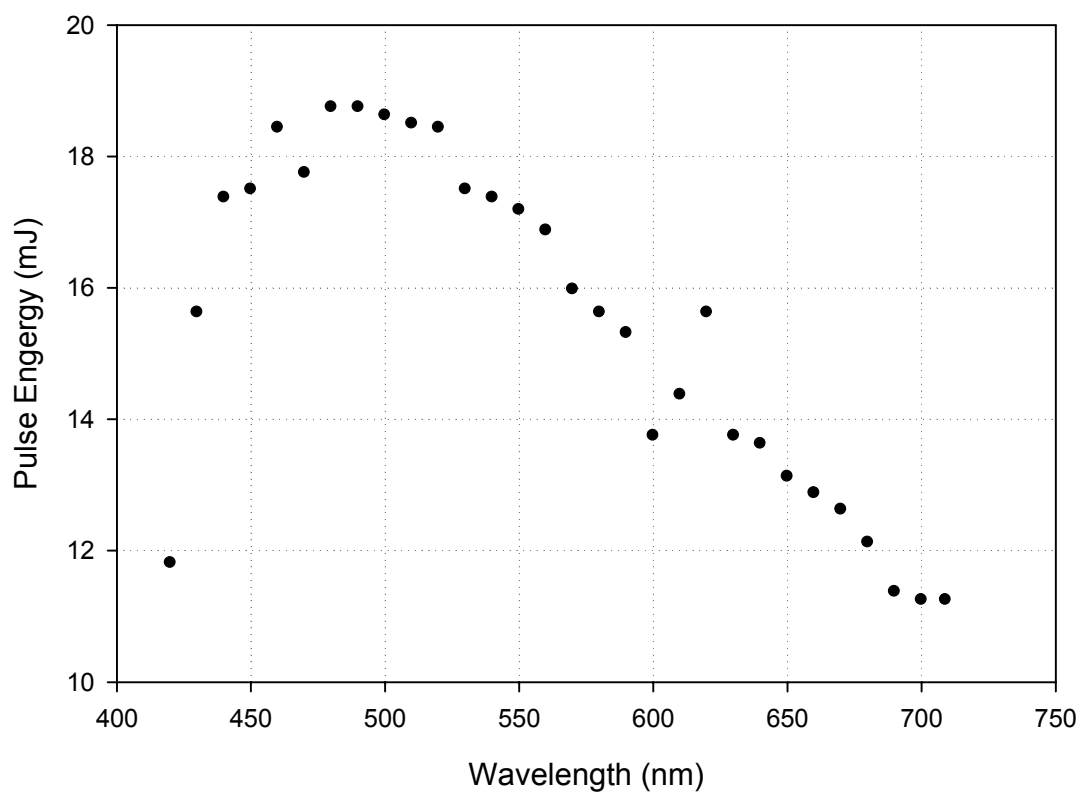
Figure 2.11   Infinity XPO energy per pulse as a function of wavelength measured at 250 mJ IR pump.
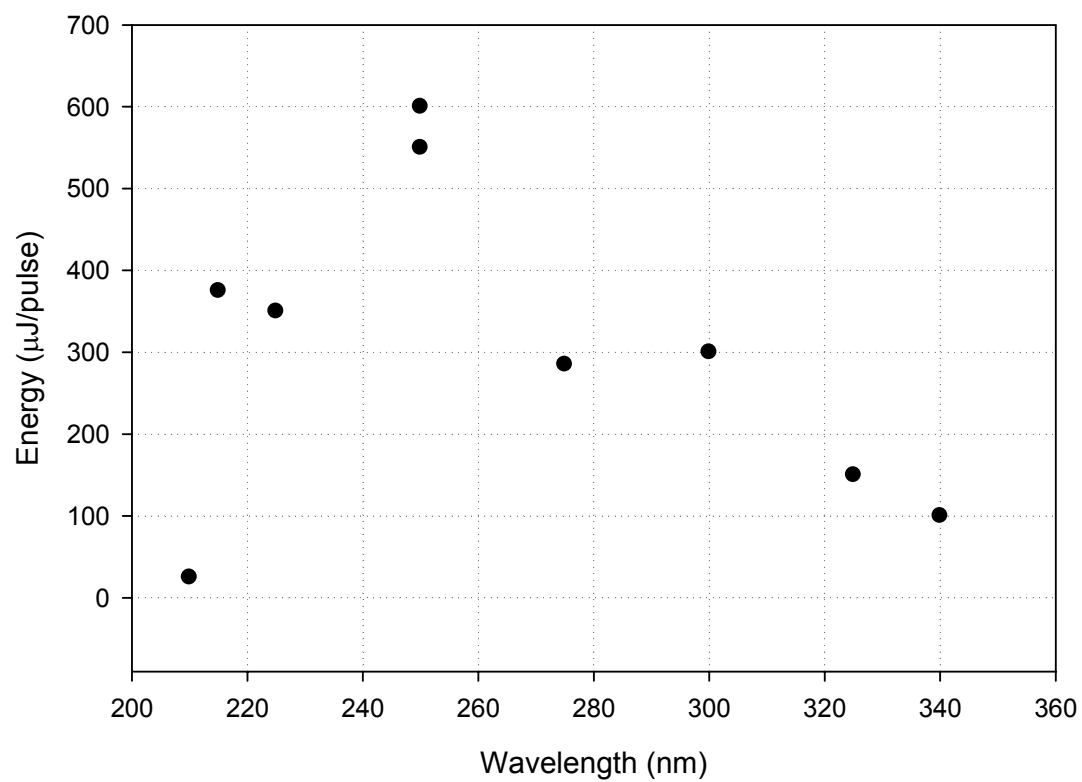
Figure 2.12   Doubled Infinity XPO energy per pulse as a function of wavelength measured at 200 mJ IR.
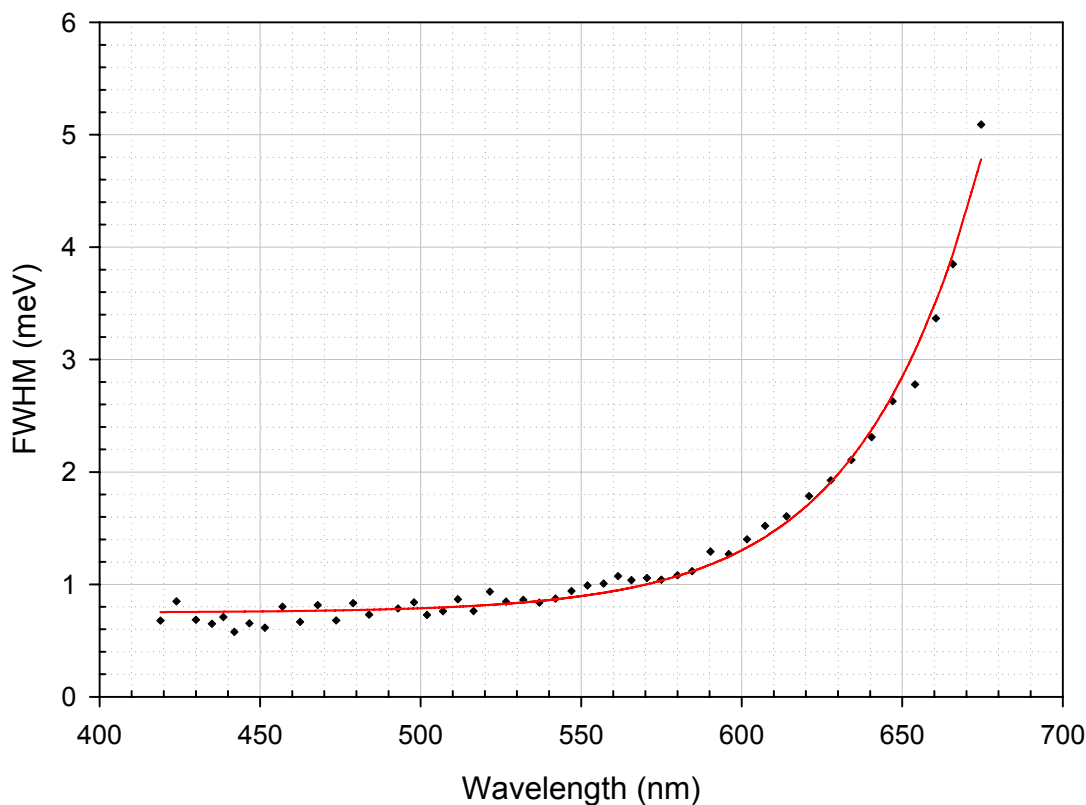
Figure 2.13   Measured Infinity XPO linewidth as a function of wavelength.

Because the linewidth near degeneracy is large enough to significantly compromise the resolution of the photoelectron velocity map imaging spectrometer, another laser source with narrower linewidth must be used. Therefore the 532 nm output of the Infinity is used to pump a Quanta-Ray PDL-1 dye laser, which has linewidth less than 1 meV between 600 nm and 800 nm. Two dyes have been used for the experiments described here. One is Exciton DCM dye which produces 610 – 690 nm pulses, and the other is Exciton LDS-698 which produces 650 – 750 nm pulses. Both dyes were dissolved in spectral grade methanol (Aldrich), and were frequency doubled in broad angle-tuned BBO. Attainable UV-Vis pulse wavelengths along with their production methods, maximum pulse energies, and linewidths are presented in Table 2.2.

Table 2.2   Recommended configurations, maximum pulse energies, and maximum linewidths for production of 210 – 750 nm nanosecond laser pulses.

wavelength (nm)	production method	maximum energy per pulse	FWHM not more than (meV)
210 – 300	OPO + BBO	1.5 mJ	2
266	355 nm + 532 nm	10 mJ	0.001
305 – 345	DCM + BBO	1.5 mJ	2.5
355	Infinity 3rd Harmonic	100 mJ	0.001
325 – 375	LDS 698 + BBO	1.5 mJ	2.5
420 – 625	OPO	20 mJ	2
532	Infinity 2nd Harmonic	200 mJ	0.001
610 – 690	DCM	20 mJ	1.25
650 – 750	LDS 698	20 mJ	1.25

2.13   Velocity Map Imaging Instrument Data Analysis

The center of the summed image for each data set is found by fitting a circle to a distinct feature in the photoelectron image. This is usually done using the "overlay" option in the DaVis program. This subroutine allows one to choose the radius and the center of the image in pixels. In general it is best to choose a radius which is 1 or 2 pixels larger than the radius of the feature to be fit. The center of the image is found by adjusting the center of the circle to fit the experimental image by eye. While other methods exist for finding the image center, fitting a circle to the

image by eye has proven to be the most accurate and reliable method to date. This center is then used to reconstruct the full 3D distribution using the BASEX program developed by Dribinski and co-workers,[17] which outputs a 2D slice through the center of the 3D distribution, a radial integration of this 2D slice, and angular anisotropy parameters (β_1, $\beta2$, and β_3) at each radial pixel position. The photoelectron feature used to find the image center should be chosen with care as different features have slightly different centers. The greater the difference in energy between the feature used to find the image center and the feature of interest, the worse the resolution for the feature of interest. Figure 2.14 shows the difference in resolution caused by using different features in a photoelectron image to find the image center. The bottom panel contains the photoelectron spectrum attained using the feature near 2.85 eV to center the image, while the top panel shows the spectrum attained using the feature at 0.45 eV to find the image center. Note that the resolution in the bottom panel is better for high eBE features compared to the top panel. Also notice that the features at low eBE in the bottom panel have superior resolution when compared to the same features in the top panel. Thus when all features of a spectrum spanning a large electron binding energy range are to be resolved, the center of several different features must be used in order to attain the best resolution possible for the entire image.
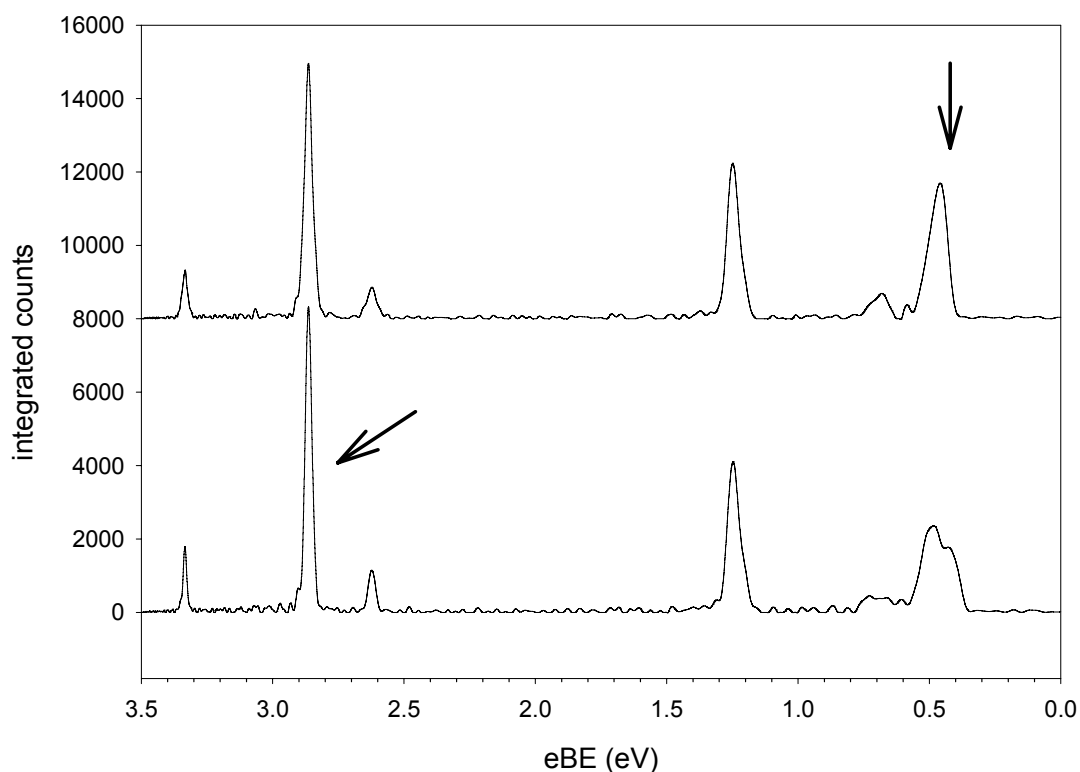
Figure 2.14   CuH⁻ 355 nm photoelectron velocity map imaging spectrum showing difference in resolution using different spectral features to center the image. The arrows indicate the feature used to center the image for each trace.

The BASEX program outputs a text file with pixel in the first column and integrated counts in the second, referred to in BASEX as a speed plot. The next step in the data analysis is to transform the pixel axis into electron kinetic energy (eKE) and electron binding energy (eBE). This is done by finding the constant of proportionality in the equation

$$eKE \propto C \times P^2 \tag{2.1}$$

where C is the proportionality constant and P is the distance in pixel from the image center. The proportionality constant is unique for each image size, laser beam height,

and laser wavelength combination. The constant is found by making a plot of eKE versus P^2 for known atomic transitions measured in an atomic photoelectron image. A linear function is then fit to this plot, the slope of which is the constant of proportionality. The linear function is forced through the origin for cases when only one atomic transition is available at the image size and laser wavelength used. The pixel position(s) for the atomic transition(s) are found by fitting a gaussian to the atomic peak(s) in a plot of counts as a function of pixel from the image center (the "speed plot" mentioned above). Once the proportionality constant is found, the pixel scale can be converted to eKE using equation 2.1. The scale is converted to binding energy by subtracting the eKE from the photon energy.

Since the photodetachment cross-section varies as $eKE^{(\ell + \frac{1}{2})}$ near threshold for detachment from an atomic anion,[18] where ℓ is the angular momentum of the photodetached electron ($\ell = 0$ for the case of detachment from a p orbital near threshold),[19] the experimental intensities for features close to threshold (within ~ 750 meV) are often scaled by this function to approximate the true relative intensities of the features in the spectrum.

2.14 Theoretical Geometry and Frequency Calculations and Photoelectron Spectral Simulation Methods

Often photoelectron spectra are complex enough that theoretical calculations are needed to aid in the spectral assignments. This may be the case because it is not clear which anion is being photodetached (due to structural isomers, anions with the same mass or poor mass resolution) or to understand the nature of the vibrational or electronic features present in

the photoelectron spectrum. Two methods for geometry and frequency calculations and spectral simulation have been used to study the systems presented here. In one, the program ACES II[20] was used to calculate the geometries and frequencies of 1,2,3-triazolide and 1,2,3-triazolyl molecules, with the spectral simulation carried out using the method pioneered by Stanton and coworkers.[21] These calculations and corresponding spectral simulations were not performed by the author, so only the results are presented here.

The method used to study all other anion systems, and that performed by the author, is presented in detail in this section. First, the geometries and frequencies of the anion, resulting neutral, and anion precursor parent neutral are calculated using the Gaussian suite of programs.[22] Careful attention is paid to the starting geometry to insure the correct isomer and symmetry is calculated. Much information is gained by calculating the geometry and frequencies of a particular system. From the results of the anion, radical, and anion precursor parent calculations one can extract the electron affinity of the radical, the gas phase acidity of the parent, the bond dissociation energy of the parent, as well as the relative stabilities of different structural and conformational isomers.

For the purposes of anion photoelectron spectral simulations, however, the geometries and frequencies of the anion and neutral are most important. Specifics of the method and basis set used in the Gaussian calculations are given along with the results for specific anions (i.e., in the chapters in which they are discussed). Once the geometries and frequencies are calculated, the outputs are converted for input into the FCFGAUS03 program by running what is referred to as an "FCF" Gaussian job. This job essentially requests high precision vectors and masses from Gaussian03. A generic Gaussian03 input file for this job is presented below. For use, text in quotes should be replaced by actual files names or methods / basis sets where appropriate.

```
-------------------------------------------------------------------------------------------------------
%chk= "check point file name of original geometry/frequency job"
# "method"/"basis set" freq=(readfc,readiso) iop(7/33=1) geom.=check guess=check
```

title card info on this line

"charge" "multiplicity"

298.15 1.0 1.0
"isotope data listed one per line in the order in which they are listed in the original geometry/frequency job"

An example set of an original geometry/frequency job and corresponding FCF job is given

below.

Original Gaussian03 Job input file:

```
%chk=HNCHCNN-cis2-anion.chk
# opt=verytight freq ub3lyp/6-311++g(d,p)

HNCHCNN cis2 anion

-1 1
N
N          1       B1
C          2       B2   1       A1
C          3       B3   2       A2   1       D1
H          4       B4   3       A3   2       D2
N          4       B5   3       A4   2       D3
H          6       B6   4       A5   3       D4

 B1=1.15924647
 B2=1.27271276
 B3=1.41988792
 B4=1.1021695
 B5=1.31273286
 B6=1.02223365
 A1=171.7841783
 A2=122.28371912
 A3=112.89185454
 A4=127.95431811
 A5=108.59511052
 D1=180.
 D2=180.
 D3=0.
 D4=180.
```

Corresponding FCF job input file:

```
-----------------------------------------------------------------------------------------------------
%chk=HNCHCNN-cis2-anion.chk
# ub3lyp/6-311++g(d,p) freq=(readfc,readiso) iop(7/33=1) geom=check guess=check

HNCHCNN cis2 anion FCF

-1 1

298.15 1.0 1.0
14
14
12
12
1
14
1


-----------------------------------------------------------------------------------------------------
```

Once the FCF Gaussian job has been run, the output files are input into the FCFGaus03

program which reads the normal coordinates and frequencies and calculates the Dushinsky

rotation matrix J and the displacement vector K. J and K are then transformed to the Sharp &

Rosenstock arrays A, B, C, D, and E. The frequencies may be scaled. In addition the atom

ordering and Cartesian axis of one file may be changed to match those of the other (this is

essential). The outputs of the FCFGaus03 program are matrices which may be read into the

PESCAL[23] program for spectral simulation.

As stated above, the PESCAL program can be used to simulate photoelectron spectra.

If using FCFGaus03 output files, the Dushinsky rotation option should be used. For the

simulation, the intensity and eKE position of the photoelectron band origin are adjustable

parameters. Other adjustable parameters include the anion temperature for each normal

mode, the type and full-width-at-half-maximum of a spectral convolution, and the option to

apply the hemispherical analyzer instrument sensitivity function. Additionally, an

experimental photoelectron spectrum in .eke format may be loaded for direct comparison to

the spectral simulation. It should be noted that the program only simulates a vertical

transition and does not treat vibronic coupling. Transitions to/from excited electronic states are able to be simulated, given that their geometries and frequencies may be calculated using Gaussian03.

Once a satisfactory simulation is complete, the transition positions and intensities (the "stick" spectrum) as well as the convolution may be saved as x, y data. Comparison of the main features in the stick spectrum to the calculated anion and neutral frequencies allows assignment of the modes active in the photoelectron spectrum.

References for Chapter II

[1]   K. M. Ervin, J. Ho, and W. C. Lineberger, *Journal of Chemical Physics* **91**, 5974 (1989).

[2]   K. M. Ervin and W. C. Lineberger, in *Advances in Gas Phase Ion Chemistry*, edited by N. G. Adams and L. M. Babcock (JAI Press, Greenwich, 1992), Vol. 1, pp. 121.

[3]   D. G. Leopold, K. K. Murray, A. E. Stevens-Miller, and W. C. Lineberger, *Journal of Chemical Physics* **83**, 4849 (1985).

[4]   T. M. Ramond, PhD, University of Colorado, 2001.

[5]   C. E. Moore, *Atomic Energy Levels*. (US GPO Circular No. 467, Washington, 1952).

[6]   D. M. Neumark, K. R. Lykke, T. Andersen, and W. C. Lineberger, *Physical Review A* **32** (3), 1890 (1985).

[7]   D. H. Andrews, T. Ichino, R. M. D. Calvi, A. J. Gianola, S. Kato, J. R. Rathbone, F. Misaizu, V. M. Bierbaum, and W. C. Lineberger, (In Press) (2006).

[8]   M. E. Nadal, P. D. Kleiber, and W. C. Lineberger, *The Journal of Chemical Physics* **105** (2), 504 (1996).

[9]   A. Sanov, T. Sanford, S. Nandi, and W. C. Lineberger, *The Journal of Chemical Physics* **111** (2), 664 (1999).

[10]   W. C. Wiley and I. H. McLaren, *Journal of Mass Spectrometry* **32** (1), 4 (1997).

[11]   A. T. J. B. Eppink and D. H. Parker, *Review of Scientific Instruments* **68** (9), 3477 (1997).

[12]   E. Surber, R. Mabbs, and A. Sanov, *Journal of Physical Chemistry A* **107** (40), 8215 (2003).

[13]   L. A. Posey, M. J. DeLuca, and M. A. Johnson, *Chemical Physics Letters* **131** (3), 170 (1986).

[14]   C. Blondel, P. Cacciani, C. Delsart, and R. Trainham, *Physical Review A* **40** (7), 3698 (1989).

[15]   R. C. Bilodeau, M. Scheer, and H. K. Haugen, *Journal of Physics B-Atomic Molecular and Optical Physics* **31** (17), 3885 (1998).

[16]   T. J. Sanford, PhD, Colorado, 2004.

[17]   V. Dribinski, A. Ossadtchi, V. A. Mandelshtam, and H. Reisler, *Review of Scientific Instruments* **73** (7), 2634 (2002).

[18]   E. P. Wigner, *Physical Review* **73**, 1002 (1948).

[19]   J. Cooper and R. N. Zare, *Journal of Chemical Physics* **48**, 942 (1968).

[20]   J. F. Stanton, J. Gauss, J. D. Watts, M. Nooijen, N. Oliphant, S. A. Perera, P. G. Szalay, W. J. Lauderdale, S. A. Kucharski, S. R. Gwaltney, S. Beck, A. Balková, D. E. Bernholdt, K. K. Baeck, P. Rozyczko, H. Sekino, C. Hober, and R. J. Bartlett, ACES II (Quantum Theory Project, University of Florida, 2006).

[21]   J. F. Stanton, T. Ichino, A. J. Gianola, and W. C. Lineberger, (2006).

[22]   M. J. Frisch, G. W. Trucks, H. B. Schlegel, G. E. Scuseria, M. A. Robb, J. R. Cheeseman, J. A. Montgomery, Jr. , T. Vreven, K. N. Kudin, J. C. Burant, J. M. Millam, S. S. Iyengar, J. Tomasi, V. Barone, B. Mennucci, M. Cossi, G. Scalmani, N. Rega, G. A. Petersson, H. Nakatsuji, M. Hada, M. Ehara, K. Toyota, R. Fukuda, J. Hasegama, M. Ishida, T. Nakajima, Y. Honda, O. Kitao, H. Nakai, M. Klene, X. Li,

J. E. Knox, H. P. Hratchian, J. B. Cross, C. Adamo, J. Jaramillo, R. Gomperts, R. E. Stratmann, O. Yazyev, A. J. Austin, R. Cammi, C. Pomelli, J. W. Ochterski, P. Y. Ayala, K. Morokuma, G. A. Voth, P. Salvador, J. J. Dannenberg, V. G. Zakrzewski, S. Dapprich, A. D. Daniels, M. C. Strain, O. Farkas, D. K. Malick, A. D. Rabuck, K. Raghavachari, J. B. Foresman, J. V. Ortiz, Q. Cui, A. G. Baboul, S. Clifford, J. Cioslowski, B. B. Stefanov, G. Liu, A. Liashenko, P. Piskorz, I. Komaromi, R. L. Martin, D. J. Fox, T. Keith, M. A. Al-Laham, C. Y. Peng, A. Nanayakkara, M. Challacombe, P. M. W. Gill, B. Johnson, W. Chen, M. W. Wong, C. Gonzalez, and J. A. Pople, Gaussian 03, Revision B.05 (Gaussian, Inc., Pittsburgh, PA, 2003).

[23]   K. M. Ervin, PESCAL, Fortran program (2003).

_____

Photoelectron Imaging Spectroscopy of 1,2,3-Triazolide

_____

3.1   Introduction

The 1,2,3-triazoles have been the subject of many theoretical and experimental investigations over the years. While most of the investigations were concerned with structural and spectroscopic properties, some have concentrated on the biological activity,[1-6] electrochemical properties,[7-11] and usefulness in fuels and explosives[12,13] of 1H-1,2,3-triazole and 2H-1,2,3-triazole. The N-H deprotonated 1,2,3-triazolide anion has been the subject of only a few investigations (see Figure 3.1 for the structures of the above mentioned species).[14-17] Because of the broad importance of the azoles, recent investigations by Gianola and co-workers have measured the N-H bond dissociation energies of pyrrole,[18] imidazole,[19] and pyrazole[25] via photoelectron spectroscopy of the N-H deprotonated anions and gas phase proton transfer kinetic measurements of the parent azoles. These investigations revealed that both the N-H and C-H sites of imidazole and pyrazole are acidic enough to be deprotonated by hydroxide in the gas phase. These investigations also reveal significant vibronic coupling in the photoelectron spectra due to the presence of low-lying electronic states of the neutral radicals formed via photodetachment. The experiments in this chapter are a continuation of this previous work from one and two nitrogen-containing to three nitrogen containing azoles in an attempt to better understand the effect of nitrogen substitution on the geometries, energetics, and thermodynamics of the azoles.
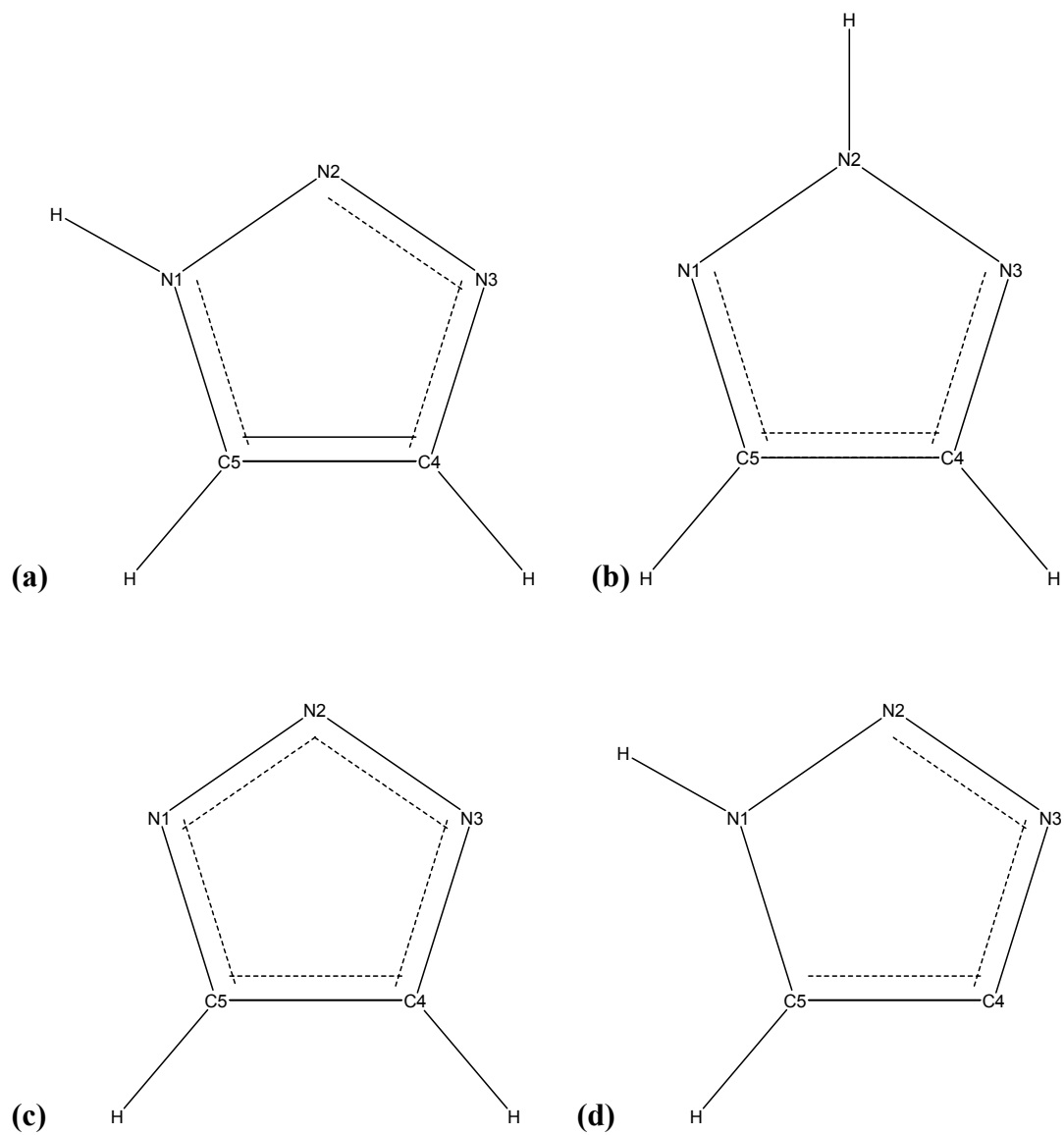
Figure 3.1. Molecular structures of 1H-1,2,3-triazole (a), 2H-1,2,3-triazolde (b), 1,2,3-triazolide (c), and C4-1,2,3-triazolide (d). Stuctures taken from Gaussian03 output.

3.2   Experimental Methods

The 1,2,3-triazolide anion was formed by deprotonation of 1H-1,2,3-triazole as described in chapter 2. Typical anion intensities of 700 – 800 mV were detected from the post-MCP preamp with a voltage of 1600 volts across the MCP inline detector. Photoelectron spectra were recorded using ultraviolet photodetachment wavelengths of 320 nm, 335 nm, and 355 nm. Doubled dye laser output was used to create the 320 nm and 335 nm pulses, while the 355 nm pulses were produced by the Infinity laser system (see chapter 2). The photoelectron imaging optics were set to maximize the 1,2,3-triazolide photoelectron image size. The well known[21] electron affinity of F atom observed in the photoelectron spectrum of F^- was used to both focus the photoelectron images and to calibrate the electron energy scale. Images were taken in the event counting mode with one second CCD exposures and very moderate laser pulse energies of less than 200 μJ for 320 nm and 335 nm pulses, and less than 2 mJ for 355 nm pulses.

3.3   Results

Representative 320 nm, 335 nm, and 355 nm raw and BASEX inverted photoelectron images of 1,2,3-triazolide anion are presented in Figure 3.2. The 320 nm images show several distinct photoelectron features at high electron velocities (outer rings), with less distinct photodetachment occurring at lower electron velocities (inner features). These images also show a large amount of detachment near the very center of the image which is slightly off center. Most of this detachment is caused by ionization of background gas by the laser pulse and is not signal from 1,2,3-triazolide. The 335 nm photoelectron images contain all but the inner most features of the 320

nm images, but they are much more distinct. The greater distinctiveness of these features is mostly due to much less laser photoionization background, but also due to enhanced resolution, as the electron kinetic energies are ~ 175 meV less than in the 320 nm images. The 355 nm images contain only the outermost ring of the 320 nm and 335 nm images. However, this wavelength has the best resolution and near zero laser photoionization background, which allows a very accurate determination of the electron binding energy of the main photoelectron feature, as well as the electron affinity of the 1,2,3-triazolyl radical.

The 335 nm photoelectron spectrum is presented in Figure 3.3. The spectrum shows transitions from the anion ground electronic and vibrational state to several electronic and vibrational states of the 1,2,3-triazolyl neutral radical. A constant background of 0.1 counts has been subtracted due to the 1,2,3-triazolide spectrum sitting atop a background of photoelectrons detached from the concurrently produced C-H deprotonated and ring-opened isomer iminodiazomethide, which has a lower electron binding energy (the photoelectron spectrum of iminodiazomethide is presented in chapter 4). The intense peak labeled "a" in Figure 3.3 is assigned as the electron affinity of the 1,2,3-triazolyl neutral radical with a value of 3.447 (4) eV, reported to a 2σ level of uncertainty. The electron affinity of 1,2,3-triazolyl has also been calculated at the (U)B3LYP/6-311++G(d,p) level of theory[22] as 3.478 eV, in good agreement with the experimental value.
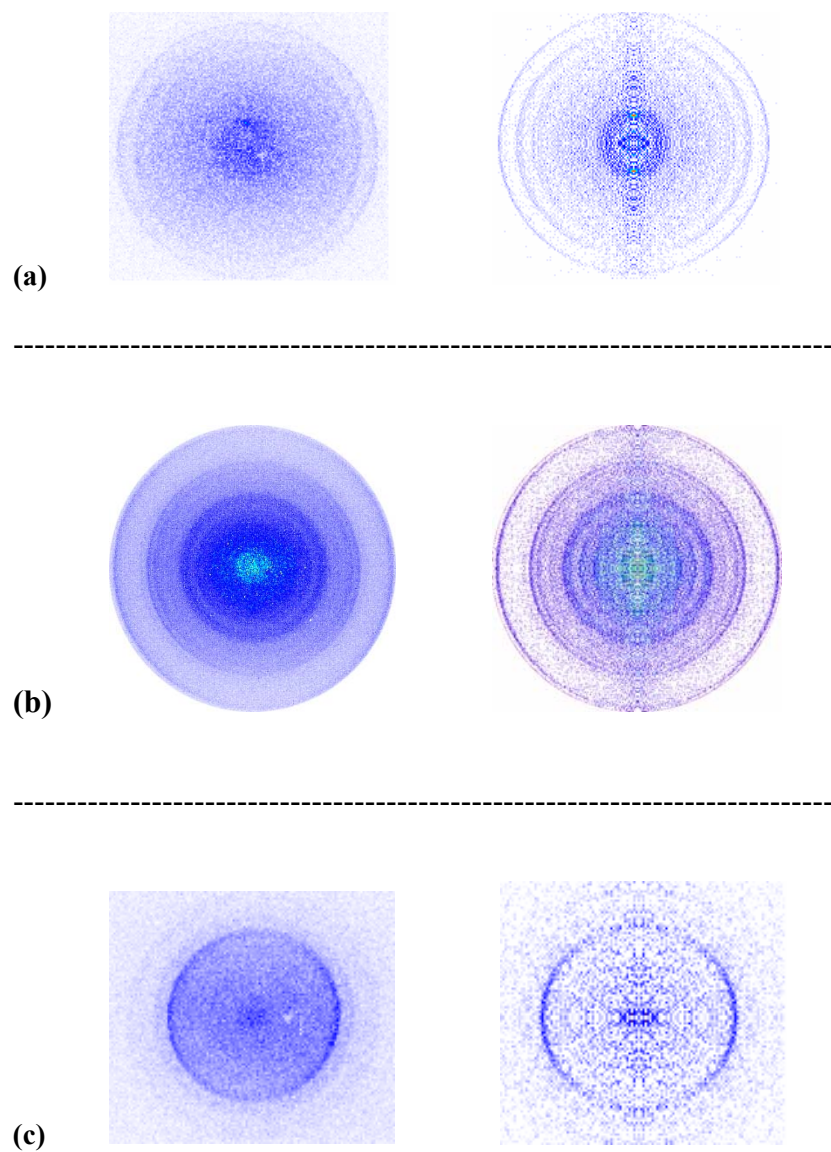
Figure 3.2. 1,2,3-triazolide raw photoelectron images (left panel) and BASEX reconstructed images (right panel) taken at (a) 320 nm, (b) 335 nm, and (c) 355 nm.
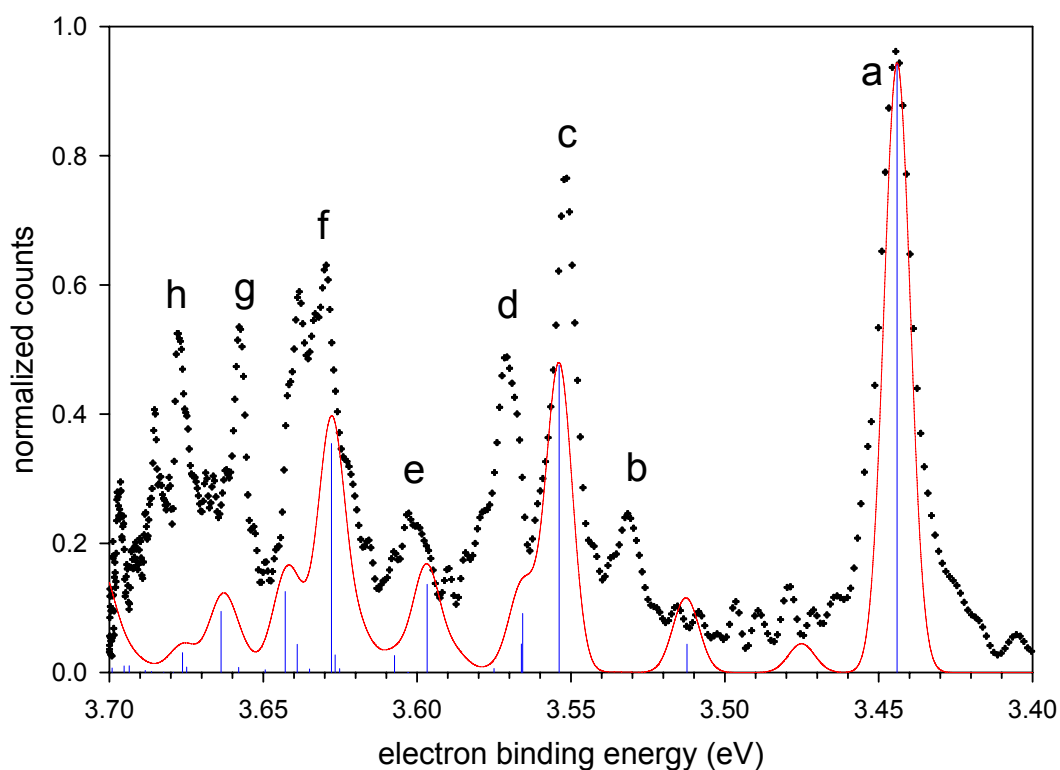
Figure 3.3. 1,2,3-triazolide 335 nm photoelectron imaging spectrum (points) with convoluted (line) transition positions and intensities (sticks).

To aid in the spectral assignments, the photoelectron spectrum of 1,2,3-triazolide was simulated using the method developed by Stanton and co-workers.[23] This simulation was not performed by the author, thus the details are not given here, as they will be presented elsewhere.[24] It should be mentioned, however, that the simulation is not complete, thus only a small amount of the observed structure in the photoelectron spectrum is assigned at this time. A full assignment of the spectrum will be given in a future publication.[24] The experimental peak positions and spectral assignments derived from this simulation are presented in Table 3.1.

Table 3.1. Peak positions and assignments for 1,2,3-triazolide 335 nm photoelectron spectrum.

peak label[a]	peak position (eV)	cm^{-1} from origin	assignment
a	3.447 (4)	0	$^2B_1$ origin
b	3.534 (4)	696 (26)	$^2B_1$, 1 quantum b_2
c	3.552 (2)	846 (34)	$^2B_1$, 1 quantum a_1
d	3.570 (3)	988 (50)	$^2B_1$, 2 quantum b_2
e	3.598 (10)	1214 (108)	
f	3.634 (3)	1497 (28)	
g	3.657 (20)	1684 (62)	
h	3.674 (30)	1825 (74)	

[a] See Figure 3.3.

The 320 nm and 355 nm 1,2,3-triazolide spectra, along with the 335 nm spectrum, are presented in Figure 3.4 for comparison. Figure 3.4 illustrates the dependence of the resolution on the electron kinetic energy. In this figure the electron kinetic energy is increasing from left to right (high eBE to low eBE), while the resolution is degrading in the same direction. This effect is also shown in the resolution of the origin peak ("a" in Figure 3.3). In the 320 nm photoelectron spectrum in Figure 3.4 the origin is a wide peak with several shoulders, in the 335 nm spectrum the peak is narrower with one resolved peak to higher electron binding energy. In the 355 nm spectrum, the origin is quite narrow and several features which were shoulders in the other spectra are there clearly resolved.
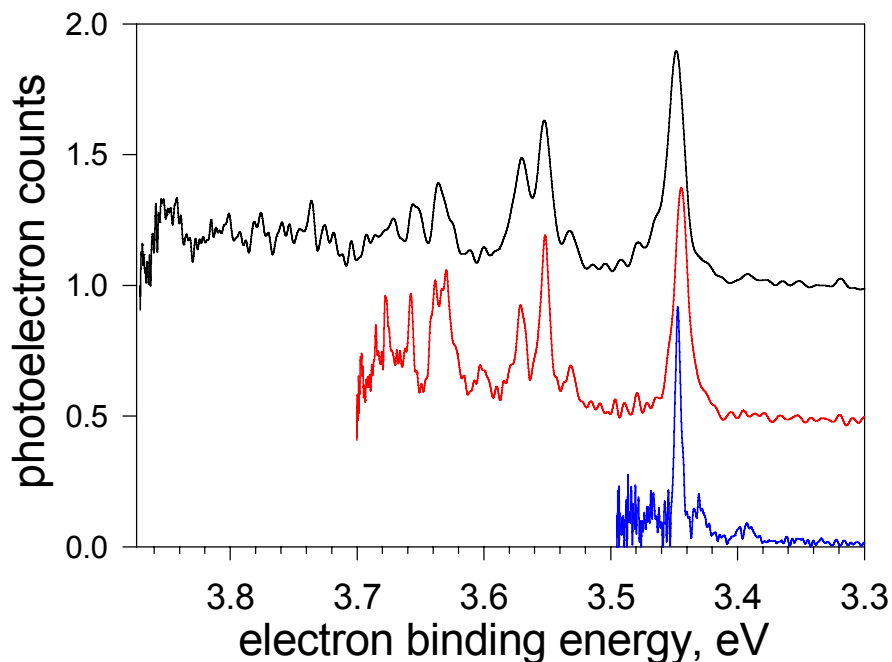
Figure 3.4. 1,2,3-triazolide photoelectron imaging spectra taken at 320 nm (top trace), 335 nm (middle trace), and 355 nm (bottom trace).

All spectra in Figure 3.4 were taken at velocity imaging magnifications which placed the electron affinity feature of the 1,2,3-triazolide spectrum very near the detector edge. In order to determine the relative amount of the iminodiazomethide anion produced, 320 nm images were taken (see chapter 4) at a magnification which included the photoelectron features arising from this isomer. The 1,2,3-triazolide and iminodiazomethide photoelectron features of this spectrum were integrated and a ring-to-linear ratio of approximately 2.5-to-1 was found. This ratio is similar to the ring-to-fragmented ratio of 2-to-1 measured in flowing afterglow-selected ion flow tube experiments.[24]

3.4   Discussion

As mentioned in the introduction, study of the thermodynamic properties of the azoles is one aim of the research conducted on 1,2,3-triazolide in this chapter. It should be mentioned that the thermodynamic properties extracted from the measurements here are all for 2H-1,2,3-triazole. This is because 1,2,3-triazolide protonates to the more stable 2H-1,2,3-triazole neutral in the FA-SIFT experiments used to measure the deprotonation enthalpy, and thus the derived acidity (as well as the thermochemical cycle) corresponds to that for 2H-1,2,3-triazole. The gas phase acidity ($\Delta_{acid}G_{298}$) of 2H-1,2,3-triazole, N-H bond dissociation energy of 2H-1,2,3-triazole, and radical heat of formation for 1,2,3-triazolyl were calculated as follows. The measured[24] gas phase acidity ($\Delta_{acid}G_{298}$) of 2H-1,2,3-triazole was converted to the gas phase enthalpy of deprotonation ($\Delta_{acid}H_{298}$) using the change in entropy between 2H-1,2,3-triazole and 1,2,3-triazolide calculated at the UB3LYP/6-311++G(d,p) level of theory.[22] The N-H bond dissociation energy was calculated by adding the electron affinity of 1,2,3-triazolyl to the enthalpy of deprotonation of 2H-1,2,3-triazolide and subtracting the ionization potential of the hydrogen atom. The enthalpy of formation for the 1,2,3-triazolyl radical was evaluated by adding the enthalpy of formation and the bond dissociation enthalpies of 2H-1,2,3-triazole and subtracting the enthalpy of formation of the hydrogen atom. Thermodynamic properties of the azoles as studied by photoelectron spectroscopy and gas phase acidity measurements are summarized in Table 3.2.

As is clear from Table 3.2, the addition of nitrogen atoms to the ring increases the electron binding energy of the N-H deprotonated anions. As discussed elsewhere,[25] the increase in electron binding energy of the azole anions is due to the stabilization of the anion HOMO which has significant nitrogen p-orbital character. The table also shows that the anion HOMO is also stabilized by having nitrogen atoms adjacent: the measured electron binding energy of pyrazolide is greater than that of imidazolide, just as the measured electron binding energy of 1,2,3,-triazolide is greater than the calculated electron binding energy of 1,2,4-triazolide. Note that the electron affinity of 1,2,3-triazolide calculated at B3LYP/6-311++G(d,p)[22] is 3.477 eV. The $\Delta_{acid}G_{298}$ values for the azoles show a very modest dependence on the arrangement of nitrogen atoms in the ring with a mild decrease with increasing number of nitrogen atoms. Accordingly, the N-H bond dissociation energy increases with the number of nitrogen atoms and is higher for azoles with a high number of adjacent nitrogen atoms.

Table 3.2. Thermodynamic trends in the azoles.

parent molecule RN-H	radical electron affinity RN$^\bullet$ (eV)	$\Delta_{acid}G_{298}$ RN-H (kcal•mol^{-1})	D_0 RN-H (kcal•mol^{-1})	radical $\Delta_f H_0$ RN$^\bullet$ (kcal•mol^{-1})
—NH pyrrole	2.145 (10)[a]	351.9 (4)[a]	93.92 (11)[a]	72.16 (2)[a]
HN—N imidazole	2.613 (6)[b]	342.6 (4)[b]	95.1 (5)[b]	79.7 (6)[b]
—NH—N pyrazole	2.937 (6)[c]	346.4 (3)[c]	101.5 (5)[c]	102.1 (5)[c]
NH N—N 1,2,4-triazole	3.426[d]	337.7[d]	110.3[d]	108.4[d]
N—NH N 2H-1,2,3-triazole	3.447 (4)[f] 3.477[d]	340.7 (20)[e]	114.9 (45)	137.4 (93)

[a] From Reference 18

[b] From Reference 19

[c] From Reference 25

[d] Calculated Using UB3LYP/6-311++G(d,p)[22]

[e] From Reference 26

[f] Experimentally determined in this study

References for Chapter III

[1]   C. W. Tornoe, S. J. Sanderson, J. C. Mottram, G. H. Coombs, and M. Meldal, *Journal of Combinatorial Chemistry* **6** (3), 312 (2004).

[2]   Y. Ding, S. A. Hofstadler, E. E. Swayze, L. Risen, and R. H. Griffey, *Angewandte Chemie, International Edition* **42** (29), 3409 (2003).

[3]   M. M. Balkis, S. D. Leidich, P. K. Mukherjee, and M. A. Ghannoum, *Drugs* **62** (7), 1025 (2002).

[4]   H. M. Guardiola-Diaz, L. A. Foster, D. Mushrush, and A. D. N. Vaz, *Biochemical Pharmacology* **61** (12), 1463 (2001).

[5]   T. Joseph-Horne and D. W. Hollomon, *Fems Microbiology Letters* **149** (2), 141 (1997).

[6]   E. Stenz, G. Menzel, and G. Schuster, *Mikrobiologicheskii Zhurnal (1978-1993)* **43** (2), 239 (1980).

[7]   Z. Zhou, R. Liu, J. Wang, S. Li, M. Liu, and J.-L. Bredas, *Journal of Physical Chemistry A* **110** (7), 2322 (2006).

[8]   H. Kusama, M. Kurashige, and H. Arakawa, *Journal of Photochemistry and Photobiology, A: Chemistry* **169** (2), 169 (2005).

[9]   K. Babic-Samardzija and N. Hackerman, *Journal of Solid State Electrochemistry* **9** (7), 483 (2005).

[10]   G. Rauhut, *Physical Chemistry Chemical Physics* **5** (5), 791 (2003).

[11]   S. A. Kaluzhina and G. V. Shatalov, 1975.

[12]   Z. X. Chen and H. M. Xiao, *Propellants Explosives Pyrotechnics* **24** (5), 319 (1999).

[13]   M. Arai, T. Tsukahara, and M. Tamura, *Proceedings of the International Pyrotechnics Seminar* **26th**, 7 (1999).

[14]   R. Vianello and Z. B. Maksic, *Molecular Physics* **103** (2-3), 209 (2005).

[15]   A. A. El-Azhary, H. U. Suter, and J. Kubelka, *Journal of Physical Chemistry A* **102** (3), 620 (1998).

[16]   C. Toernkvist, J. Bergman, and B. Liedberg, *Journal of Physical Chemistry* **95** (8), 3119 (1991).

[17]   S. B. Bulgarevich, V. S. Bolotnikov, V. N. Sheinker, O. A. Osipov, and A. D. Garnovskii, *Zhurnal Obshchei Khimii* **45** (8), 1821 (1975).

[18]   A. J. Gianola, T. Ichino, R. L. Hoenigman, S. Kato, V. M. Bierbaum, and W. C. Lineberger, *J. Phys. Chem. A.* **108** (46), 10326 (2004).

[19]   A. J. Gianola, T. Ichino, R. L. Hoenigman, S. Kato, V. M. Bierbaum, and W. C. Lineberger, *J. Phys. Chem. A.* **109** (50), 11504 (2005).

[20]   A. J. Gianola, PhD, University of Colorado, 2006.

[21]   C. Blondel, P. Cacciani, C. Delsart, and R. Trainham, *Physical Review A* **40** (7), 3698 (1989).

[22]   M. J. Frisch, G. W. Trucks, H. B. Schlegel, G. E. Scuseria, M. A. Robb, J. R. Cheeseman, J. A. Montgomery, Jr. , T. Vreven, K. N. Kudin, J. C. Burant, J. M. Millam, S. S. Iyengar, J. Tomasi, V. Barone, B. Mennucci, M. Cossi, G. Scalmani, N. Rega, G. A. Petersson, H. Nakatsuji, M. Hada, M. Ehara, K. Toyota, R. Fukuda, J. Hasegama, M. Ishida, T. Nakajima, Y. Honda, O. Kitao, H. Nakai, M. Klene, X. Li, J. E. Knox, H. P. Hratchian, J. B. Cross, C. Adamo, J. Jaramillo, R. Gomperts, R. E. Stratmann, O. Yazyev, A. J. Austin, R. Cammi, C. Pomelli, J. W. Ochterski, P. Y. Ayala, K. Morokuma, G. A. Voth, P. Salvador, J. J. Dannenberg, V. G. Zakrzewski, S. Dapprich, A. D. Daniels, M. C. Strain, O. Farkas, D. K. Malick, A. D. Rabuck, K. Raghavachari, J. B. Foresman, J. V. Ortiz, Q. Cui, A. G. Baboul, S. Clifford, J.

Cioslowski, B. B. Stefanov, G. Liu, A. Liashenko, P. Piskorz, I. Komaromi, R. L. Martin, D. J. Fox, T. Keith, M. A. Al-Laham, C. Y. Peng, A. Nanayakkara, M. Challacombe, P. M. W. Gill, B. Johnson, W. Chen, M. W. Wong, C. Gonzalez, and J. A. Pople, Gaussian 03, Revision B.05 (Gaussian, Inc., Pittsburgh, PA, 2003).

[23] J. F. Stanton, T. Ichino, A. J. Gianola, and W. C. Lineberger, (2006).

[24] D. H. Andrews, T. Ichino, R. M. D. Calvi, A. J. Gianola, S. Kato, G. J. Rathbone, F. Misaizu, V. M. Bierbaum, and W. C. Lineberger, (In Preparation) (2006).

[25] A. J. Gianola, T. Ichino, S. Kato, V. M. Bierbaum, and W. C. Lineberger, *J. Phys. Chem. A.*, (in press) (2006).

[26] J. Catalán, R. M. Claramunt, J. Elguero, J. Laynez, M. Menéndez, F. Anvia, J. H. Quian, M. Taagepera, and R. W. Taft, *J. Am. Chem. Soc.* **110** (13), 4105 (1988).

Hemispherical Analyzer Photoelectron Spectroscopy of Iminodiazomethide

_____

4.1   Introduction

This chapter presents photoelectron spectroscopy results of iminodiazomethide, a C-H deprotonated ring-opened isomer of 1,2,3-triazole. iminodiazomethide is concurrently produced along with 1,2,3-triazolide in the pulsed supersonic expansion source used in the photoelectron imaging studies.   While a few photoelectron imaging spectra of iminodiazomethide were recorded, the majority of the results reported here were obtained using the hemispherical analyzer photoelectron spectrometer. From the results of a spectral simulation (see results, section 4.3, for details), the structure is E-iminodiazomethide and is presented in Figure 4.1 along with the structures of1H-1,2,3-triazole and C5 deprotonated 1H-1,2,3-triazole. This structure is very similar to that of E-vinyldiazomethide, which is a C-H deprotonated ring-opened isomer of pyrazole. Vinyldiazomethide was synthesized by reaction of the allyl anion and nitrous oxide, and its photoelectron spectrum and analysis have been presented elsewhere.[1] Interestingly, vinyldiazomethide was not concurrently produced with pyrazolide in the hemispherical analyzer microwave discharge source.

Fabian and coworkers have modeled the cyclization of iminodiazomethanes as a possible synthetic route to 1H-1,2,3-triazole.[2]   They found that the cyclization of E-iminodiazomethane to form 1H-1,2,3-triazole was exothermic by   15 kcal mol^{-1}, with a reaction barrier of ~ 9 kcal mol^{-1}. Trifonov and coworkers[3] have modeled the ring-opening of 1,2,3-triazolide at the N-N position and found it to be highly endothermic by ~ 65 kcal mol^{-1}. To date, no theoretical or experimental results on the ring-opening of C4 1H-1,2,3-triazolide or the ring closing of iminodiazomethide have been reported. Likewise, there have

been no theoretical or experimental reports in the literature on the structure or energetics of iminodiazomethide anion or iminodiazomethyl radical. The photoelectron spectra as well as the calculated geometries and frequencies presented here, then, are the first investigations of the iminodiazomethide anion and the iminodiazomethyl radical.
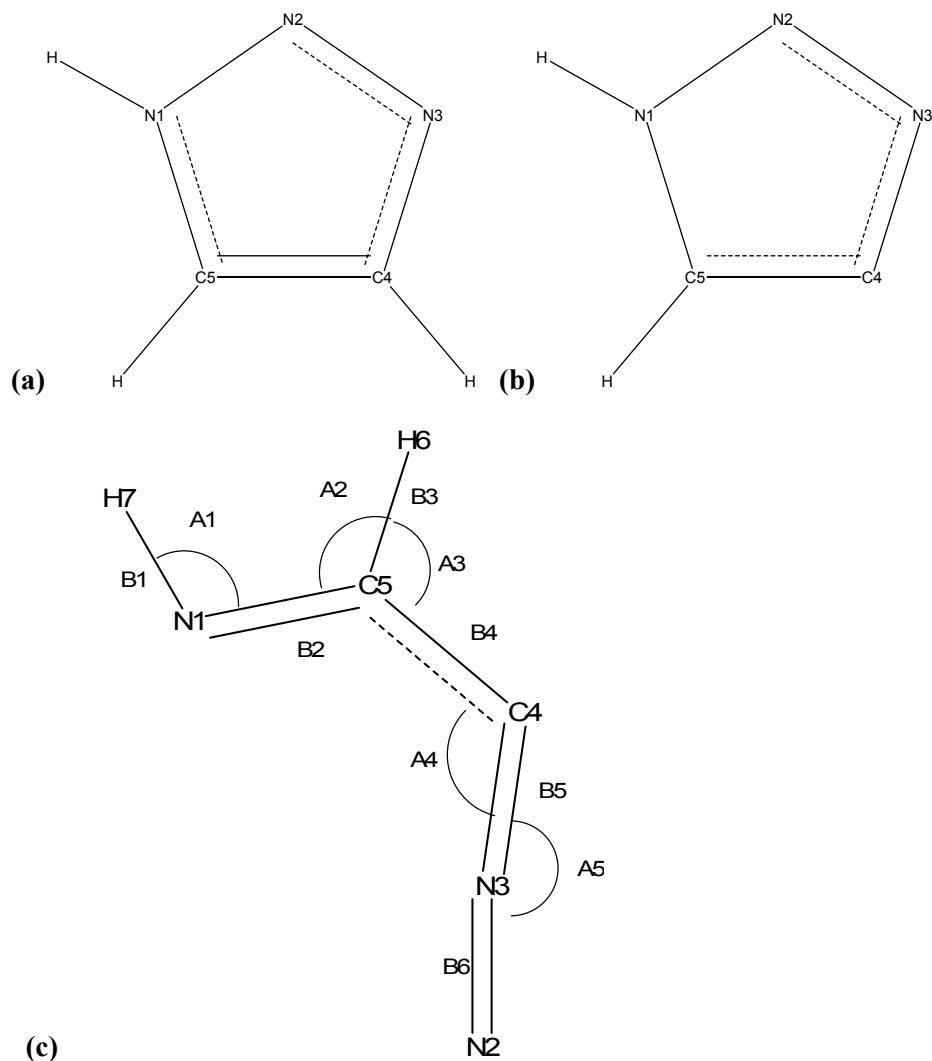
Figure 4.1 Structures of (a) 1H-1,2,3-triazole, (b) C4 deprotonated 1H-1,2,3-triazolide, and (c) E-iminodiazomethide. Geometries calculated at the b3lyp/6-311++g(d,p) level of theory.[4] Structures taken directly from Gaussian03 output files.

4.2   Experimental Methods

Ultraviolet negative ion photoelectron spectra of E-iminodiazomethide have been obtained with the hemispherical analyzer and photoelectron velocity map imaging spectrometers described in chapter 2. For the hemispherical analyzer studies, atomic oxygen anion (O⁻) was formed by microwave discharge of helium

buffer gas (~0.5 Torr) in the presence of a trace amount of oxygen in a flowing afterglow source. The O⁻ reacted with methane to produce hydroxide anion (HO⁻). Then 1H-1,2,3-triazole (Sigma, 97 %) was introduced downstream via a stream of helium flowing over a liquid sample. HO⁻ deprotonation of 1H-1,2,3-triazole at the N-H position produced the 1,2,3-triazolide anion, while deprotonation at the C4 position (along with ring opening) produced E-iminodiazomethide (see Figure 4.1 for the relevant molecular structures). In order to better understand the structure of iminodiazomethide, spectra were taken using both HO⁻ and O⁻ to abstract a proton from 1H-1,2,3-triazole. Because O⁻ is a weaker base[5] than HO⁻, it is more likely to abstract the more acidic N-H proton than one of the less acidic C-H protons. Photoelectron spectra were taken of the m/z = 68 ion produced with HO⁻ (1,2,3-triazolide and iminodiazomethide) and O⁻ (1,2,3-triazolide only), and were recorded at laser electric field polarizations of 0°, 90°, and 54.7° (magic angle) with respect to the photoelectron collection direction.

For the photoelectron velocity map imaging studies, iminodiazomethide was produced by passing a mixture of 10% molecular oxygen and 20% methane in argon through a scintillated glass bubbler containing liquid 1H-1,2,3-triazole heated to 85°C. This mixture was expanded through a pulsed valve with a stagnation pressure of 45 psi. The expansion was met collinearly by a 1 keV beam of electrons, with 1,2,3-triazolide and iminodiazomethide produced via the reactions above. The 320 nm photoelectron images were recorded with imaging voltages which allowed the simultaneous detection of photoelectrons detached from both 1,2,3-triazolide and

iminodiazomethide. The electron energy scale was calibrated using the well-known[6] electron affinity of F atom observed in the photoelectron spectrum of F⁻.

4.3   Results

Photoelectron spectra were measured at 351.1 nm for the anion at m/z 68 formed both in the presence of HO⁻ and in the presence of O⁻. Both spectra contain a feature at high electron binding energy which is assigned to detachment from 1,2,3-triazolide anion. In addition, the mass 68 anion formed in the presence of HO⁻ also contains a lower electron binding energy feature which is assigned to the C4 deprotonated 1,2,3-triazolide ring-opened isomer E-iminodiazomethide.   The $\Delta_{acid}H_{298}$ for deprotonation of 1H-1,2,3-triazolide was calculated at the (U)B3LYP/6-311++G(d,p) level of theory[4] as 390.6 kcal mol⁻¹ for deprotonation at the C4 position and 372.2 kcal mol⁻¹ at the C5 position. Since the deprotonation enthalpy at the C4 position is greater than both H_2O (390.3 kcal mol⁻¹)[7] and HO (382.6 kcal mol⁻¹)[5], deprotonation at the C4 position of 1H-1,2,3,-triazole most likely does not occur in the isolated system, nor does it effectively compete with deprotonation at the much more acidic C1 and C5 positions. In addition, no photodetachment was observed from C4 or C5 triazolide anion, and only ring opened C4 anion photodetachment was observed. This strongly suggests that when deprotonation occurs at the carbon positions, it either leads to fragmentation (C5) or to ring-opening (C4). Calculations with the same basis set and method show that the E-iminodiazomethide anion is more stable than the C4 deprotonated 1H-1,2,3-triazolide anion by ~ 16 kcal mol⁻¹, and a transition state of Cs symmetry for ring opening to form E-iminodiazomethide was

found $\sim$ 19 kcal mol^{-1} above C4 deprotonated 1H-1,2,3-triazolide. A probable pathway for production of E-iminodiazomethide from 1H-1,2,3-triazolide is presented in the discussion, section 4.4.

The 351.1 nm hemispherical analyzer photoelectron spectrum of iminodiazomethide formed in the presence of HO$^-$ is presented in Figure 4.2. The intense peak at 2.484 (5) eV electron binding energy is assigned as the electron affinity of the iminodiazomethyl neutral radical. The peaks to lower electron binding energies are transitions from excited vibrational states of the anion, while the peaks to higher electron binding energy are transitions to excited vibrational states of the neutral radical. To aid the spectral assignments, the geometry and frequencies of several geometric isomers of the iminodiazomethane anion and neutral were calculated at the (U)B3LYP/6-311++G(d,p) level of theory.[4] The 351.1 nm photoelectron spectrum was simulated for all isomers in order to confirm which iminodiazomethide isomer is the signal carrier for the photoelectron spectrum. It was found that the E form of iminodiazomethide gave the most accurate spectral simulation, thus the signal carrier is identified as E-iminodiazomethide. The adiabatic electron affinity extracted from these calculations is 2.339 eV, in good agreement with the experimental value. The general structure of E-iminodiazomethane is presented in Figure 4.1, with the optimized anion and neutral radical geometries presented in Table 4.1.
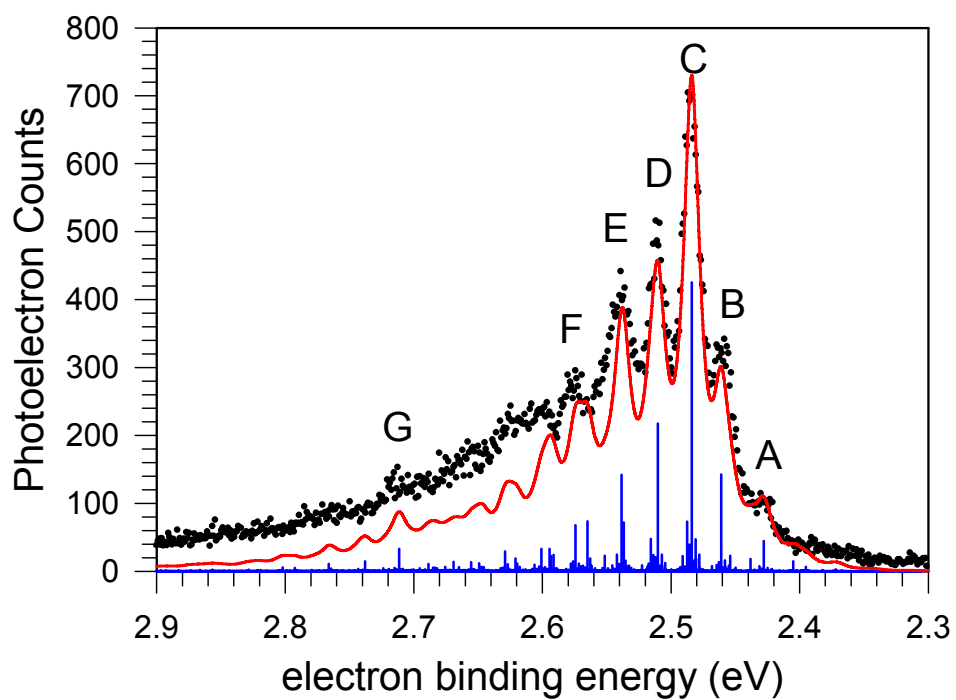
Figure 4.2 351.1 nm photoelectron spectrum of iminodiazomethide anion. The points are the experimental data. Transition energies and intensities from a Frank-Condon calculation (sticks) which are convoluted by the instrument resolution function (line) are also presented.

Table 4.1   E-iminodiazomethane anion and neutral radical calculated[a] structures. See Figure 4.1 for bond length and angle definitions.

Anion		Neutral Radical	
bond lengths (Å)	**bond angles (deg.)**	**bond lengths (Å)**	**bond angles (deg.)**
$B_1 = 1.02$	$A_1 = 108.6$	$B_1 = 1.02$	$A_1 = 110.5$
$B_2 = 1.31$	$A_2 = 119.1$	$B_2 = 1.29$	$A_2 = 123.0$
$B_3 = 1.10$	$A_3 = 112.9$	$B_3 = 1.09$	$A_3 = 114.7$
$B_4 = 1.42$	$A_4 = 122.2$	$B_4 = 1.44$	$A_4 = 119.8$
$B_5 = 1.27$	$A_5 = 171.8$	$B_5 = 1.29$	$A_5 = 170.0$
$B_6 = 1.16$		$B_6 = 1.14$	

[a] Calculated at (U)B3LYP/6-311++G(d,p)[4]

The optimized geometries and normal mode frequencies of the anion and neutral were used to perform an initial Franck-Condon simulation using the PESCAL program.[8,9] The position and intensity of the electron affinity peak in this simulation were set to match the experimental values. While this simulation (not shown) is in qualitative agreement with the measured spectrum, the transition positions were in significant error (~ 10%). Rather than use this simulation to directly make the spectral assignments, the simulation was used to identify the normal modes active in

the observed spectrum. In a second simulation the frequencies of the main spectral features were set to the values observed in the experimental spectrum (found by measuring the spectral distance from the origin). These new line positions and intensities were convoluted by a Lorenzian function with a 15 meV full-width-at-half-maximum. This second simulation is in excellent agreement with the experimental spectrum, allowing for confident spectral assignments. The peak positions and assignments are presented in Table 4.2, while the simulated spectrum is presented along with the experimental spectrum in Figure 4.2.

Table 4.2   Peak positions and assignments for E-iminodiazomethide photoelectron spectrum.

peak label[a]	peak position (eV)	cm^{-1} from origin	assignment	excited motion
A	2.428	-452 (12)	3_1^0	C-N-N bend
B	2.461	-184 (7)	1_1^0	C-C-N bend
C	2.484	0	0_0^0	–
D	2.510	213 (5)	2_0^1	C-C-N bend
E	2.538	441 (5)	4_0^1	C-N-N bend
F	2.574	730 (12)	6_0^1 and $2_0^1 4_0^1$	$\nu6$ = C-C-N bend
G	2.712	1837 (14)	13_0^1	N-N stretch

[a] See Figure 4.2.

The polarization measurements reveal an anisotropy parameter of ~ −0.36 for all features in the spectrum. This suggests that the photodetached electrons originate from the same molecular orbital in the anion, further confirming the assignments (which simulated photodetachment producing a single electronic state in the neutral radical).

The 320 nm photoelectron velocity map raw and BASEX reconstructed images are presented in Figure 4.3. The corresponding photoelectron spectrum is presented in Figure 4.4, with the inner (low eKE, high eBE) features assigned to photodetachment from 1,2,3-triazolide and the outer (high eKE, low eBE) features assigned to photodetachment from E-iminodiazomethide. The 1,2,3-triazolide and E-iminodiazomethide photoelectron features of this spectrum were integrated and a ring-to-linear ratio of approximately 2.5-to-1 was found. This ratio is similar to the ring-to-fragmented ratio of 2-to-1 measured in a flowing afterglow-selected ion flow tube experiment.[10]
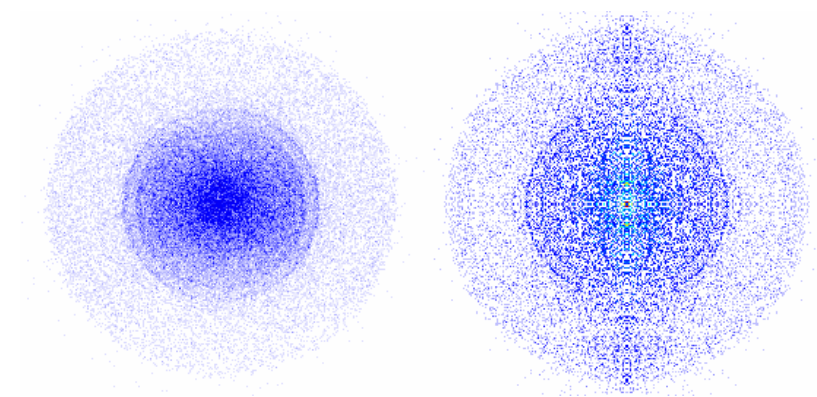
Figure 4.3   320 nm photoelectron velocity map imaging raw (left) and BASEX reconstructed (right) images containing features arising from 1,2,3-triazolide (inner) and E-iminodiazomethide (outer) photodetachment.
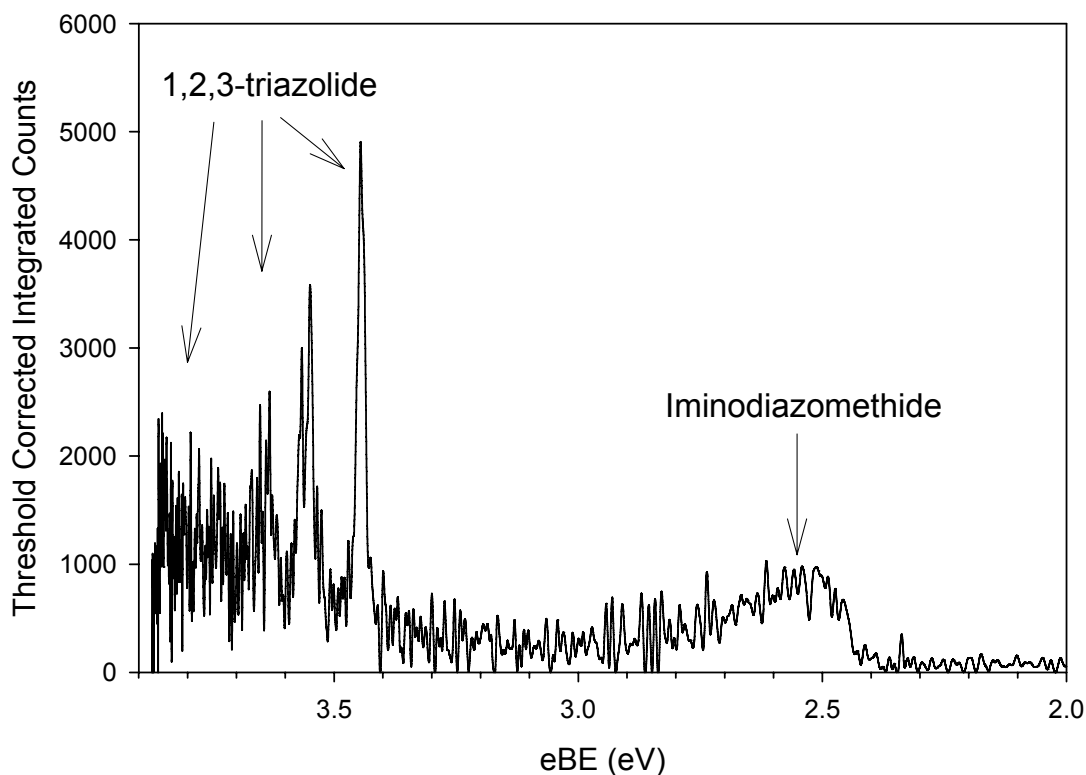
Figure 4.4   320 nm velocity map imaging photoelectron spectrum containing features arising from photodetachment of 1,2,3-triazolide (high eBE) and iminodiazomethide (low eBE).

4.4   Discussion

The electron binding energy of E-iminodiazomethide, 2.461 (8) eV, is considerably less than the electron binding energy of 1,2,3-triazolide, 3.447 (4) eV. This is most likely due to the aromaticity of the 1,2,3-triazolide ring which significantly stabilizes the anion, and is absent in the E-iminodiazomethide structure. The observed photoelectron spectrum and the calculated geometry of E-iminodiazomethide are very similar to that of E-vinyldiazomethide,[1] while the

electron binding energy is approximately 630 meV higher, due to the electron stabilization caused by the presence of an additional nitrogen atom.

As mentioned in section 4.3, the ring opening of C4 deprotonated 1H-1,2,3-triazole to form E-iminodiazomethide does not occur in the isolated system. However, deprotonation at the C4 position to form an ion-dipole complex of C4-1H-1,2,3-triazolide and water was calculated[4] at the UB3LYP/6-311++G(d,p) level of theory to be exothermic by $\sim$ 24 kcal mol^{-1}. Since deprotonation to form the separated products was calculated to be slightly endothermic, the exothermicity of the deprotonated ion-dipole complex is due entirely to the ion-dipole complexation energy. It is reasonable to assume that the barrier to ring-opening is not significantly higher in the ion-dipole complex than in the isolated anion, thus the complex has enough energy to overcome this barrier. Likewise, the transition state for dissociation of the ring-opened anion water complex must lie below the energy of the isolated reactants (1H-1,2,3-triazolide and hydroxide). This reaction scheme is consistent with the experimental observation that E-iminodiazomethide is produced while C4 deprotonated 1H-1,2,3-triazolide is not. The energetics of the ring-opening are presented in Figure 4.5.

This is opposite of the experimental observations in pyrazole[11] and imidizole[12] where the C4 deprotonated ions were observed without ring-opening. Deprotonation at the C4 site of these azoles was calculated to be exothermic by several kcal mol^{-1}. The transition state for dissociation of the lower azole C4 deprotonated ion-dipole complex to remove water is significantly loose compared to the transition state for

ring-opening of the C4 deprotonated anion, thus dissociation of the ion-dipole

complex is much more likely than ring-opening of the anion.
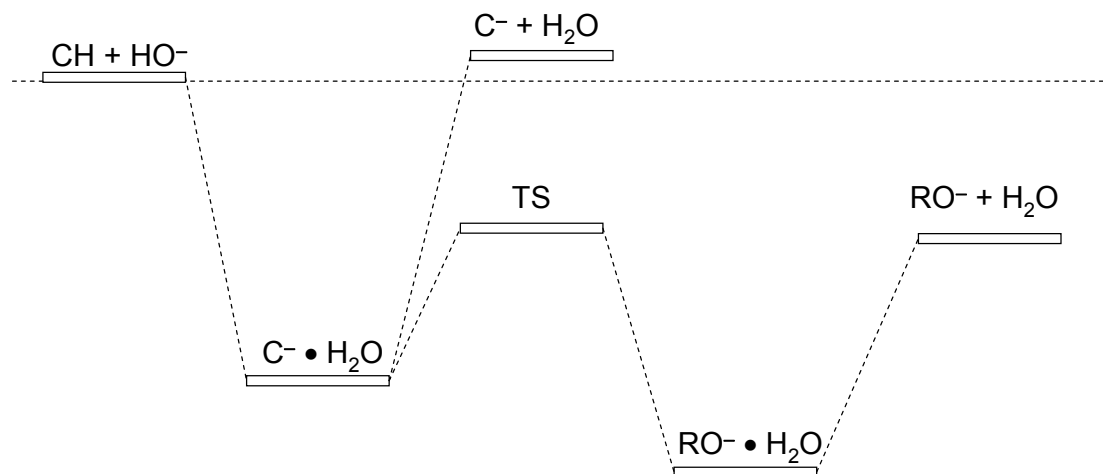
Figure 4.5   Reaction energetics for production of E-iminodiazomethane from 1H-1,2,3-triazole. CH represents 1H-1,2,3-triazole, C⁻ represents C4 deprotonated 1H-1,2,3-triazole, TS is the ring-opening transition state, and RO⁻ represents E-iminodiazomethide.

References for Chapter IV

[1]   A. J. Gianola, PhD, University of Colorado, 2006.

[2]   W. M. F. Fabian, V. A. Bakulev, and C. O. Kappe, *Journal of Organic Chemistry* **63** (17), 5801 (1998).

[3]   R. E. Trifonov, I. Alkorta, V. A. Ostrovskii, and J. Elguero, *Heterocycles* **52** (1), 291 (2000).

[4]   M. J. Frisch, G. W. Trucks, H. B. Schlegel, G. E. Scuseria, M. A. Robb, J. R. Cheeseman, J. A. Montgomery, Jr. , T. Vreven, K. N. Kudin, J. C. Burant, J. M. Millam, S. S. Iyengar, J. Tomasi, V. Barone, B. Mennucci, M. Cossi, G. Scalmani, N. Rega, G. A. Petersson, H. Nakatsuji, M. Hada, M. Ehara, K. Toyota, R. Fukuda, J. Hasegama, M. Ishida, T. Nakajima, Y. Honda, O. Kitao, H. Nakai, M. Klene, X. Li, J. E. Knox, H. P. Hratchian, J. B. Cross, C. Adamo, J. Jaramillo, R. Gomperts, R. E. Stratmann, O. Yazyev, A. J. Austin, R. Cammi, C. Pomelli, J. W. Ochterski, P. Y. Ayala, K. Morokuma, G. A. Voth, P. Salvador, J. J. Dannenberg, V. G. Zakrzewski, S. Dapprich, A. D. Daniels, M. C. Strain, O. Farkas, D. K. Malick, A. D. Rabuck, K. Raghavachari, J. B. Foresman, J. V. Ortiz, Q. Cui, A. G. Baboul, S. Clifford, J. Cioslowski, B. B. Stefanov, G. Liu, A. Liashenko, P. Piskorz, I. Komaromi, R. L. Martin, D. J. Fox, T. Keith, M. A. Al-Laham, C. Y. Peng, A. Nanayakkara, M. Challacombe, P. M. W. Gill, B. Johnson, W. Chen, M. W. Wong, C. Gonzalez, and J. A. Pople, Gaussian 03, Revision B.05 (Gaussian, Inc., Pittsburgh, PA, 2003).

[5]   E. P. Hunter and S. G. Lias, in *NIST Chemistry WebBook, NIST Standard Reference Database Number 69*, edited by P. J. Linstrom and W. G. Mallard (National Institute of Standards and Technology, Gaithersburg MD, 20899, 2005).

6   C. Blondel, P. Cacciani, C. Delsart, and R. Trainham, *Physical Review A* **40** (7), 3698

        (1989).

7   J. R. Smith, J. B. Kim, and W. C. Lineberger, *Physical Review A* **55**, 2036 (1997).

8   K. M. Ervin, PESCAL, Fortran program (2003).

9   K. M. Ervin, T. M. Ramond, G. E. Davico, R. L. Schwartz, S. M. Casey, and W. C.

        Lineberger, *Journal of Physical Chemistry A* **105** (48), 10822 (2001).

10   D. H. Andrews, T. Ichino, R. M. D. Calvi, A. J. Gianola, S. Kato, G. J. Rathbone, F.

        Misaizu, V. M. Bierbaum, and W. C. Lineberger, (In Press) (2006).

11   A. J. Gianola, T. Ichino, S. Kato, V. M. Bierbaum, and W. C. Lineberger, *J. Phys.

        Chem. A.*, (in press) (2006).

12   A. J. Gianola, T. Ichino, R. L. Hoenigman, S. Kato, V. M. Bierbaum, and W. C.

        Lineberger, *J. Phys. Chem. A.* **109** (50), 11504 (2005).

_____

Hemispherical Analyzer Photoelectron Spectroscopy of AgO⁻, AuO⁻, and AuS⁻

_____

5.1   Introduction

Silver and gold metal oxides have been the subject of both experimental and theoretical investigations because of their usefulness in catalysis,[1-8] as electrodes in power cells,[9] and as thin film substrate materials for surface-enhanced Raman spectroscopy (SERS).[10] Several experimental[11-18] and theoretical[19-23] investigations have reported bond lengths, vibrational frequencies, spin-orbit splittings, and term energies for the neutral ground state and several electronic excited states of AgO. Likewise there have been few experimental[24-27] and theoretical[28,29] investigations of AuO properties. To date the only investigations of gold or silver oxide anions are those reported here.[30,31] In addition, very little experimental[26,32,33] and theoretical[34-36] attention has been paid to the AuS molecule.

Most recently O'Brien[14] has measured the harmonic frequencies, bond lengths, and electronic term energies for the ground $^2\Pi_i$ and excited $^2\Sigma^+$ states of AgO. The bond dissociation energy of AgO has been measured by Smoes and coworkers.[26] O'Brien[27] has also recently reported the bond lengths, vibrational frequencies, and spin-orbit splittings for the $^2\Pi_i$ ground states of AuO. A moderate resolution photoelectron spectrum of AuS⁻ has been reported by Nakajima,[32] with only the electron affinity and ground state spin-orbit splitting reported.

This chapter presents the results of hemispherical energy analyzer phototelectron studies of AgO⁻, AuO⁻, and AuS⁻. The experimental conditions are briefly explained in section 5.2, the photoelectron spectroscopy and spectral simulations are presented in section

5.3, comparison of transition metal oxide photoelectron results are presented in section 5.4, and some brief conclusions are made in section 5.5

5.2 Experimental Methods

Photoelectron spectra were taken using the hemispherical analyzer photoelectron spectrometer described in Chapter 2. Briefly, AgO^- was produced by sputtering a silver rod (Goodrich) in 500 mtorr of He/Ar and reacting the resulting plasma with oxygen. AuO^- was produced in a similar manor using a gold rod (Goodrich). AuS^- was produced by reacting a gold plasma with CS_2 (Aldrich, 97%). After production the ions were mass selected by a Wein velocity filter resulting in typical anion beams of a few picoamps of current. Photoelectron spectra were recorded using 363.8 nm radiation to photodetach the anions. Spectra were taken with the angle between the laser electric field vector and the photoelectron collection axis at 54.7° (magic angle), 0°, and 90°.

5.3.1 AgO$^-$ Results

A survey of the photoelectron spectrum of AgO^- shows photodetachment in the region between 1.5 eV and 2.8 eV electron binding energy. The features in this range are plotted in Figures 5.1(a) and 5.1(b). The single peak in Figure 5.1(a) at 2.70 eV binding energy is the transition to the $\nu = 0$ level in the A $^2\Sigma^+$ state of AgO. Peaks C, E, and G in Figure 5.1(b) are transitions from the anion ground state to the $\nu = 0$, 1, and 2 levels, in the X $^2\Pi_{3/2}$ state of AgO, respectively. Peaks D, F, and H are transitions from the anion ground state to the $\nu = 0$, 1, and 2 levels, in the X $^2\Pi_{1/2}$ state of AgO, respectively. Peaks A and B are vibrational hotband transitions from the anion $\nu = 1$ state to the ground vibrational level in the X $^2\Pi_{3/2}$ and X $^2\Pi_{1/2}$ states of AgO, respectively. The position of peak C defines the electron affinity of AgO as 1.655(4) eV. Many of the experimental investigations[11,17,18,24]

report a $^2\Pi$ state lying about 24,400 cm^{-1} above the ground state, which was not accessible by the photon energy used here.

The peak assignments were confirmed by simulating the vibrational progression in Figure 5.1(b). A Franck-Condon simulation of the data in Figure 5.1(b) using the program PESCAL[37,38] was carried out as follows. The anion and neutral electronic ground states were modeled as Morse oscillators. The neutral parameters (r_e, ω_e, $\omega_e x_e$) were fixed to known literature values.[12,16] The lack of a vibrational progression for transitions to the A state shows that the anion bond length and the neutral A state bond lengths are essentially identical. Thus the anion equilibrium bond length was fixed at the 1.935 Å neutral A $^2\Sigma^+$ state literature value,[14] and only the anion harmonic vibrational frequency ω_e was allowed to vary, effectively determining the hot band position. Franck-Condon factors were determined by numerical integration of the Laguerre wave function solutions[39] to the Morse potentials. The instrumental lineshape was modeled as a Gaussian with 15 meV full width at half maximum. Other parameters input into the simulation were the 0-0 transition position and height and the anion temperature (~300 K). The simulated spectrum is plotted in Figure 5.1(b) as a solid line. Molecular constants and electronic state splittings derived from the transition assignments and the Franck-Condon simulation are summarized in Table 5.1, along with recent literature values for comparison. The electronic ground state of AgO$^-$ is found to have a vibrational frequency of 497 (15) cm^{-1} and an equilibrium bond length of 1.935 (2) Å. The neutral A state term energy and the X state spin-orbit splitting and vibrational frequency reported here are in good agreement with the known literature values.[14]

The adiabatic dissociation energy of AgO$^-$ to Ag + O$^-$ can be obtained from a thermodynamic cycle:

$$D_0\,(\text{AgO}^-) = D_0\,(\text{AgO}) - \text{EA}\,(\text{O}^-) + \text{EA}\,(\text{AgO}) \qquad\qquad (5.1)$$

The dissociation energy of AgO has been determined to be 2.29(15) eV from a mass spectrometric Knudsen cell measurement,[26] while the electron affinity of O^-[1.461 122(3) eV] is well known.[40] Using the EA (AgO) measured in this work, the $D_0(AgO^-)$ obtained is 2.48(15) eV [57.2(3.5) kcal mol^{-1}]. The accuracy of this dissociation energy is limited by the mass spectrometric Knudsen cell measurement. A quantity measured with greater accuracy is the difference in bond strengths:

$$D_0 (AgO^-) - D_0 (AgO) = 0.193(2) \text{ eV } [4.45(5) \text{ kcal mol}^{-1}] \tag{5.2}$$

This difference in dissociation energies clearly shows that AgO^- is more strongly bound than AgO.
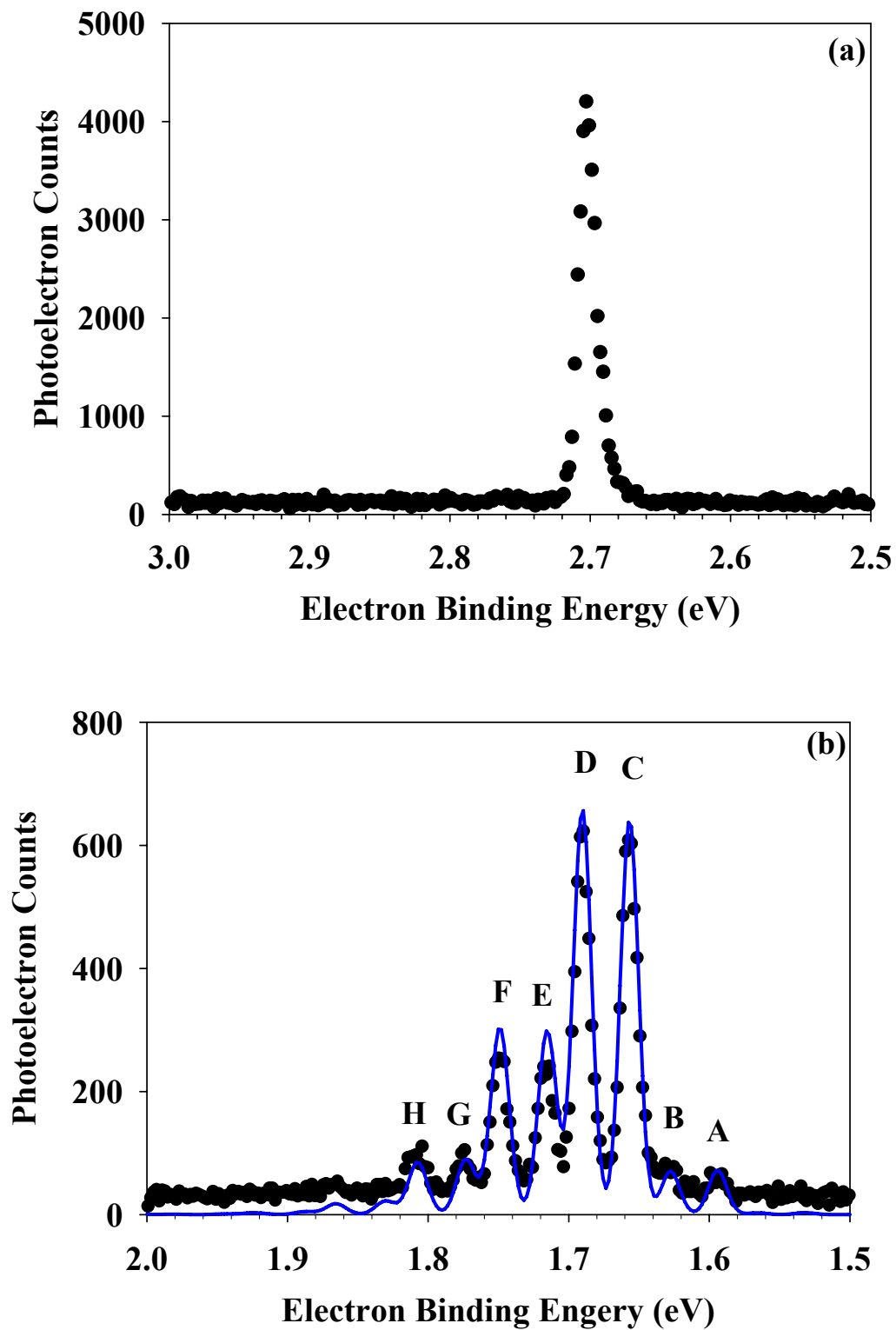
Figure 5.1   364 nm photoelectron spectra of AgO⁻ showing transitions to the (a) $^2\Sigma^+$ excited state and (b) $^2\Pi_i$ spin-orbit split ground states of AgO. The points are the data and the solid line is a Franck-Condon simulation.

Table 5.1   Spectroscopic constants for AgO^- and AgO.

State	T_e (eV)		ω_e (cm^{-1})		r_e (Å)
	This work	Literature[a]	This work	Literature[a]	
AgO^- ($X\,^1\Sigma^+$)	$-1.655\,(4)^{c}$	–	$497\,(20)^{c}$	–	$1.935\,(2)^{b,c}$
AgO ($X\,^2\Pi_{3/2}$)	0	–	$481\,(15)$	485^{c}	$2.005^{a,c}$
AgO ($X\,^2\Pi_{1/2}$)	$0.033\,(5)$	0.033^{c}	$481\,(15)$	485^{c}	$2.005^{a,c}$
AgO ($A\,^2\Sigma^+$)	$1.045\,(8)$	1.045^{c}	–	–	$1.935^{a,c}$

[a] From reference 14

[b] This work

[c] Best value

5.3.2   AuO⁻ Results

Unlike the AgO^- photoelectron spectrum, only transitions from the anion ground electronic state to the $^2\Pi_i$ states of AuO are observed in the 363.8 nm photoelectron spectrum of AuO^-. The 363.8 nm photoelectron spectrum is presented in Figure 5.2. The spectrum contains a strong transition to the neutral $\nu = 0$ vibrational level of the $X\,^2\Pi_{3/2}$ electronic state (peak A), which is assigned as the electron affinity with a value of 2.374(7) eV. A very weak transition to the $\nu = 1$ vibrational level of this state is also observed (peak B). In contrast, the transition to the $\nu = 1$ level in the $^2\Pi_{1/2}$ state (peak D) has a much higher intensity, though it remains less intense than the transition to the $\nu = 0$ (peak C). The vibrational frequency of the $^2\Pi_{3/2}$ state is 620 (15) cm^{-1}, while the vibrational frequency for the $^2\Pi_{1/2}$ state is 570 (15) cm^{-1}. The spin-orbit splitting of the ground state is the splitting of peaks A and C and is

found to be 0.179 (10) eV. The anisotropy parameters for peaks A and C were found to be –

0.25 and 0.50, respectively. The large difference in anisotropy parameters suggests that these

two peaks arise from different electronic states, strengthening the electronic origin

assignments.

To further confirm the spectral assignments, and to determine the difference in bond

length between the anion and neutral AuO, Franck-Condon simulations were performed as

described above. In these simulations the neutral $^2\Pi_{3/2}$ state bond length was set at the

current literature value (1.912 Å)[27] and hot band transitions were not considered. The

simulated spectrum is presented in Figure 5.2 as the solid line. The change in bond length

between the anion $X\,^1\Sigma^+$ electronic state and the neutral $X\,^2\Pi_{3/2}$ state is found to be 0.010 (2)

Å and 0.020 (2) Å for detachment to the $^2\Pi_{1/2}$ state. The spectroscopic constants derived

from the spectral simulations are presented in Table 5.2. From equation 1 above, the

calculated difference in bond dissociation energies (D_0) between AuO⁻ and AuO is:

$$D_0(\text{AuO}^-) - D_0(\text{AuO}) = \text{EA (AuO)} - \text{EA(Au)} = 0.065\ (7)\ \text{eV} \qquad\qquad (5.3)$$

Table 5.2   Spectroscopic constants for AuO⁻ and AuO.

State	T_e (eV)	ω_e (cm^{-1})	Δr_e (Å)
AuO⁻ ($X\,^1\Sigma^+$)	−2.374 (7)	not observed	0
AuO ($X\,^2\Pi_{3/2}$)	0	620 (15)	0.010 (2)
AuO ($X\,^2\Pi_{1/2}$)	0.179 (10)	570 (15)	0.020 (2)
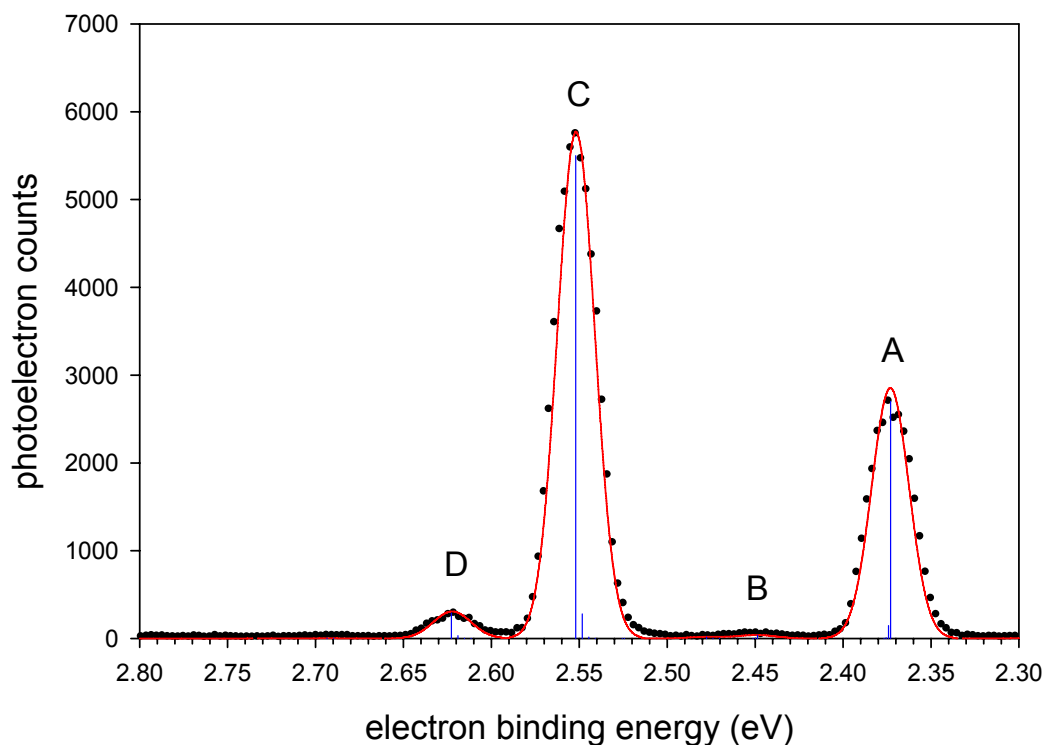
Figure 5.2   363.8 nm photoelectron spectrum of AuO⁻ showing transitions to the $^2\Pi_i$ ground states of AuO.

5.3.3   AuS⁻ Results

Much like the AuO⁻ photoelectron spectrum, the AuS⁻ 363.8 nm photoelectron spectrum contains transitions from the anion ground electronic $\nu = 0$ state to the neutral $^2\Pi_i$ spin-orbit split states, with no higher lying electronic states accessible. The spectrum is presented in Figure 5.3. The AuS⁻ spectrum contains a transition to the $\nu = 1$ vibrational level of both the $^2\Pi_{3/2}$ state (peak C) and the $^2\Pi_{1/2}$ state (peak E), though the magnitude of peak E is much less than that of peak C. In addition, the AuS⁻ photoelectron spectrum contains a hot band transition (peak A) which is built off of the origin peak. The measured angular anisotropy parameters of 0.15 for peak B and 0.30 for peak D confirm that these transitions involve different electronic states. Thus peak B is assigned as the electron affinity of AuS with a value of 2.469 (6) eV, while the spin-orbit splitting of the $^2\Pi_i$ states is found to

be 0.159 (7) eV from the splitting of peaks B and D. Spacings between peaks B and C (as well as peaks D and E) define the neutral vibrational frequency of the $^2\Pi_i$ states as 400 (15) cm^{-1}. Similarly, the spacing between peaks A and B defines the anion ground $^1\Sigma^+$ state vibrational frequency as 380 (15) cm^{-1}.

The extremely small magnitude of the vibrational progression of the transition to the $^2\Pi_{1/2}$ state of AuS strongly suggests that the equilibrium bond length change between this state and the anion ground state is very small. In contrast, the moderate vibrational progression of the $^2\Pi_{3/2}$ state suggests a modest bond length change between that state and the anion ground state. Unfortunately there are no reports of an experimentally obtained equilibrium bond length for AuS or AuS$^-$, thus only the relative bond lengths can be obtained. To do this, and to confirm the spectral assignments above, the AuS$^-$ photoelectron spectrum was simulated. The simulation for transitions to both the $^2\Pi_i$ states is presented in Figure 5.3 as the solid line. The difference in bond length between the anion and the $^2\Pi_{3/2}$ state was found to be 0.030 (2) Å, while the bond length change between the anion and the $^2\Pi_{1/2}$ state was found to be 0.011 (2) Å. The difference in bond dissociation energies between the anion and neutral is found as above to be

$$D_0(\text{AuS}^-) - D_0(\text{AuS}) = \text{EA (AuS)} - \text{EA (Au)} = 0.160(6) \text{ eV} \qquad (5.4)$$

The derived spectroscopic constants for AuS$^-$ and AuS are summarized in Table 5.3.

Table 5.3　　　Spectroscopic constants for AuS$^-$ and AuS.

State	T_e (eV)	ω_e (cm^{-1})	Δr_e (Å)
AuS$^-$ ($X\,^1\Sigma^+$)	−2.469 (6)	380 (15)	0
AuS ($X\,^2\Pi_{3/2}$)	0	400 (15)	0.030 (2)
AuS ($X\,^2\Pi_{1/2}$)	0.159 (7)	400 (20)	0.011 (2)
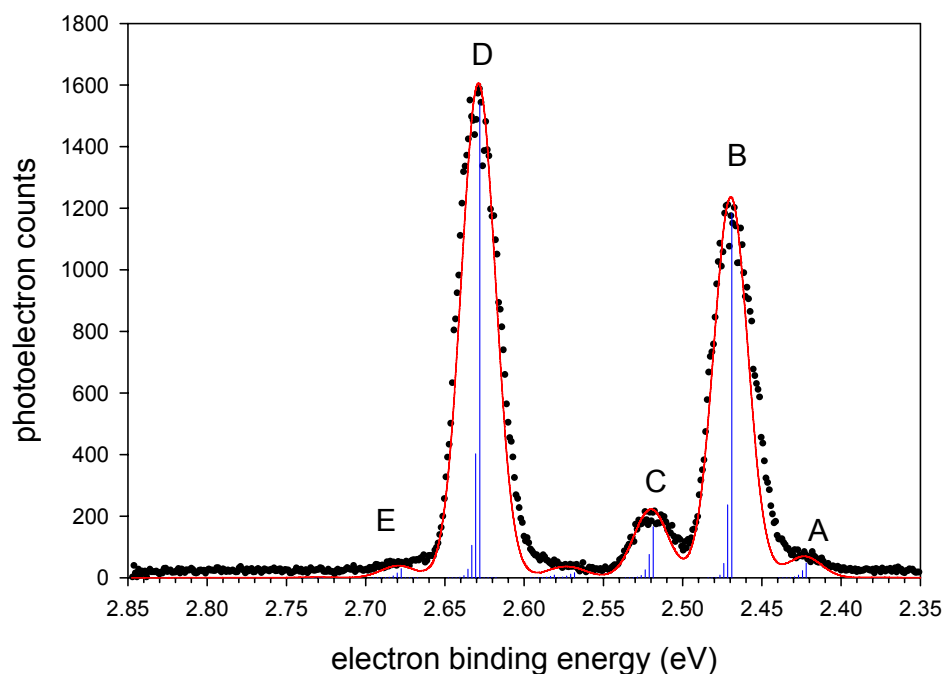
Figure 5.3   AuS⁻ 363.8 nm photoelectron spectrum showing transitions to the spin-orbit split $^2\Pi_i$ states of AuS.

5.4   Discussion

The negative ion photoelectron spectra of copper,[41] silver, and gold oxides are amazingly simple, especially when compared to the photoelectron spectra of the nickel, platinum, and palladium oxides.[42] The relative simplicity is due in most part to the small number of accessible low lying atomic electronic states of the coinage metal (group 11) oxides (two or three) as compared to the group 10 oxides (minimum four). The difference of course is the $s^1 d^{10}$ valence electronic configuration of the group 11 metals as compared to the $s^2 d^8$ valence electronic configuration of the group 10 metals. The coinage metal oxide neutrals (AgO, AuO, CuO) are well described[23] by an ionic $M^+(s^1 d^{10})$ $O^-(2s^2 2p^5)$

configuration. This configuration leads to $p\sigma^2 p\pi^3$ $^2\Pi_i$ ground states and $p\sigma^1 p\pi^4$ $^2\Sigma^+$ low lying excited states (not observed in the AuO⁻ photoelectron spectrum). Assuming a one photon process for photodetachment, the anions then have $p\sigma^2 p\pi^4$ $^1\Sigma^+$ ground states.

Insight into the bonding character of the π and σ molecular orbitals of the group 11 metal oxide (sulfide) anions may be gained by examining the bond length change between the anion and neutral derived from the Franck-Condon spectral simulations. These bond length changes along with the electron affinities, and electronic term energies are presented in Table 5.4. The equilibrium bond length change between the anion the neutral for removal of the an electron from the anion π orbital to produce the neutral $^2\Pi_i$ states is moderate for CuO and AgO, and less for AuO and AuS. This suggests that these electrons are mildly bonding in CuO⁻ and AgO⁻, and weakly bonding in AuS⁻ and AuO⁻. Furthermore, removal of a σ electron to produce the $^2\Sigma^+$ state produces a mild bond length change for CuO, and no bond length change for AgO (this state was not spectroscopically accessible in the AuO⁻ and AuS⁻ photoelectron experiments). Therefore, the σ electrons are slightly bonding in CuO⁻ and non-bonding in AgO⁻.

Examination of the other spectroscopic constants in Table 5.4 reveals very little difference in the electron affinities, spin-orbit splittings, and $^1\Sigma^+$ state term energies of CuO and AgO. There is significant difference between CuO/AgO and AuO/AuS, however. This difference is attributed to the significant relativistic effects of Au.[43-45] The larger electron affinity of AuO/AuS (and Au) is caused by the contraction of the Au 6s orbital. The spin-orbit splitting of the $^2\Pi_i$ states, while nearly identical for CuO and AgO, is much larger for AuO and AuS, due to these relativistic effects.

Table 5.4   Comparison of spectroscopic constants for CuO, AgO, and AuO.

oxide	electron affinity (eV)	$^2\Pi_{3/2} - {}^2\Pi_{1/2}$ splitting (eV)	$^2\Sigma^+$ state T_e (eV)	anion-neutral Δr_e (Å)	
				$^2\Pi_i$	$^2\Sigma^+$
CuO	1.777	0.035	0.977	0.054	0.034
AgO	1.655	0.033	1.045	0.070	0
AuO	2.374	0.179	not observed [a]	0.020	–
AuS	2.469	0.159	not observed [a]	0.030	–

[a] The term energy for this electronic state was too high to be accessed with the photon energy used in this study

References for Chapter V

[1]   J. D. Grunwaldt and A. Baiker, *Journal of Physical Chemistry B* **103**, 1002 (1999).

[2]   J. D. Grunwaldt, M. Maciejewski, O. S. Becker, P. Fabrizioli, and A. Baiker, *Journal of Catalysis* **186** (2), 458 (1999).

[3]   M. Haruta, *Catalysis Today* **36** (1), 153 (1997).

[4]   M. Haruta, N. Yamada, T. Kobayashi, and S. Iijima, *Journal of Catalysis* **115** (2), 301 (1989).

[5]   Z. P. Liu, P. Hu, and A. Alavi, *Journal of the American Chemical Society* **124** (49), 14770 (2002).

[6] N. Lopez and J. K. Norskov, *Journal of the American Chemical Society* **124** (38), 11262 (2002).

[7] M. Valden, X. Lai, and D. W. Goodman, *Science* **281** (5383), 1647 (1998).

[8] C. Yang and Z. Y. Meng, *Applied Catalysis* **71** (1), 45 (1991).

[9] D. F. Smith, G. R. Graybill, R. K. Grubbs, and J. A. Gucinski, *Journal of Power Sources* **65** (1-2), 47 (1997).

[10] D. Buchel, C. Mihalcea, T. Fukaya, N. Atoda, J. Tominaga, T. Kikukawa, and H. Fuji, *Applied Physics Letters* **79** (5), 620 (2001).

[11] V. Bojovic, A. Antic-Jovanovic, M. M. Stoiljkovic, M. Miletic, and D. S. Pesic, *Spectroscopy Letters* **32** (5), 875 (1999).

[12] L. C. O'Brien, S. J. Wall, and G. L. Henry, *Journal of Molecular Spectroscopy* **191** (1), 218 (1998).

[13] T. Steimle, M. Tanimoto, K. Namiki, and S. Saito, *Journal of Chemical Physics* **108** (18), 7616 (1998).

[14] L. C. O'Brien, S. J. Wall, and M. K. Sieber, *Journal of Molecular Spectroscopy* **183** (1), 57 (1997).

[15] B. R. Vujisic, J. J. Savovic, V. Bojovic, and D. S. Pesic, *Spectroscopy Letters* **26** (8), 1529 (1993).

[16] M. J. Griffiths and R. F. Barrow, *Journal of Physics B* **10** (5), 925 (1977).

[17] U. Uhler, *Arkiv For Fysik* **7** (12), 125 (1953).

[18] F. W. Loomis and T. F. Watson, *Physical Review* **48**, 280 (1935).

[19] G. Igel, U. Wedig, M. Dolg, P. Fuentealba, H. Preuss, H. Stoll, and R. Frey, *Journal of Chemical Physics* **81** (6), 2737 (1984).

[20] C. W. Bauschlicher, C. J. Nelin, and P. S. Bagus, *Journal of Chemical Physics* **82** (7), 3265 (1985).

[21] P. J. Hay and R. L. Martin, *Journal of Chemical Physics* **83** (10), 5174 (1985).

22   J. Andzelm, E. Radzio, and D. R. Salahub, *Journal of Chemical Physics* **83** (9), 4573 (1985).

23   C. W. Bauschlicher, H. Partridge, and S. R. Langhoff, *Chemical Physics* **148** (1), 57 (1990).

24   M. J. Griffiths and R. F. Barrow, *Journal of the Chemical Society-Faraday Transactions II* **73**, 943 (1977).

25   A. Hecq, M. Vandy, and M. Hecq, *Journal of Chemical Physics* **72** (4), 2876 (1980).

26   S. Smoes, F. Mandy, A. Vander Auwera-Mahieu, and J. Drowart, *Bulletin des Societes Chimiques Belges* **81** (1-2), 45 (1972).

27   L. C. O'Brien, S. C. Hardimon, and J. J. O'Brien, *Journal of Physical Chemistry A* **108** (51), 11302 (2004).

28   P. Schwerdtfeger, M. Dolg, W. H. E. Schwarz, G. A. Bowmaker, and P. D. W. Boyd, *Journal of Chemical Physics* **91** (3), 1762 (1989).

29   J. M. Seminario, A. G. Zacarias, and J. M. Tour, *Journal of the American Chemical Society* **121**, 411 (1999).

30   D. H. Andrews, A. J. Gianola, and W. C. Lineberger, *Journal of Chemical Physics* **117** (8), 4074 (2002).

31   T. Ichino, A. J. Gianola, D. H. Andrews, and W. C. Lineberger, *Journal of Physical Chemistry A* **108** (51), 11307 (2004).

32   A. Nakajima, T. Taguwa, K. Nakao, K. Hoshino, S. Iwata, and K. Kaya, *Surface Review and Letters* **3** (1), 417 (1996).

33   K. A. Gingerich, *Journal of the Chemical Society [Section] D: Chemical Communications* (10), 580 (1970).

34   Z. J. Wu, *Journal of Physical Chemistry A* **109** (26), 5951 (2005).

35   G. Bravo-Perez and I. L. Garzon, *Theochem* **619**, 79 (2002).

[36]   P. J. Renders and T. M. Seward, *Geochimica et Cosmochimica Acta* **53** (2), 245 (1989).

[37]   K. M. Ervin, T. M. Ramond, G. E. Davico, R. L. Schwartz, S. M. Casey, and W. C. Lineberger, *Journal of Physical Chemistry A* **105** (48), 10822 (2001).

[38]   K. M. Ervin, Fortran PESCAL (Reno, NV, 2001).

[39]   K. Cashion, *Journal of Molecular Spectroscopy* **10**, 182 (1963).

[40]   D. M. Neumark, K. R. Lykke, T. Andersen, and W. C. Lineberger, *Physical Review A* **32** (3), 1890 (1985).

[41]   M. L. Polak, M. K. Gilles, J. Ho, and W. C. Lineberger, *Journal of Physical Chemistry* **95** (9), 3460 (1991).

[42]   T. M. Ramond, G. E. Davico, F. Hellberg, F. Svedberg, P. Salen, P. Soderqvist, and W. C. Lineberger, *Journal of Molecular Spectroscopy* **216** (1), 1 (2002).

[43]   P. Pyykko, *Chemical Reviews* **88** (3), 563 (1988).

[44]   K. S. Pitzer, *Accounts of Chemical Research* **12** (8), 272 (1979).

[45]   P. Pyykko and J. P. Desclaux, *Accounts of Chemical Research* **12** (8), 276 (1979).

_____

Photoelectron Velocity Map Imaging of CuH⁻ and CuH₂⁻

_____

6.1 Introduction

Interest in the copper hydride anions CuH⁻ and CuH₂⁻ arose during the studies of the copper-methanol and copper-methoxy anion complexes reported in Chapter 7. In an effort to locate copper anion in the spectrum, photoelectron images of CuH⁻ and CuH₂⁻ were taken. It was assumed that photoelectron spectra had previously been taken of these very basic molecules, but following a rigorous literature search, it was found that they had not. CuH_2 and CuH₂⁻ have been studied in a series of publications by the Andrews group.[1-3] In these experiments, laser ablated copper atoms were co-deposited either with pure H_2 or H_2 and a rare gas (Ar or Ne) onto a cold window forming a rare gas or H_2 matrix. Infrared spectra were then taken and the spectral lines assigned with the aid of DFT calculations of the fundamental vibrational frequencies. These studies identified the ground electronic state of CuH₂⁻ to be linear ($^1\Sigma^+$) with a CuH bond length of 1.456 Å and CuH_2 to be bent ($^2B_2$) with bond length of 1.527 Å and bond angle of 122.6°. The calculations also predict that ground state CuH_2 is higher in energy than Cu and H_2, and was only observed by trapping in cold matrices.

In the case of CuH, some experimental investigators have reported the production,[4,5] dissociation energy,[5-8] and thermodynamic properties.[9,10] However, most experimental investigators have reported the ultraviolet-visible,[11-13] infrared,[2,3,14-16] and microwave[17] spectra of neutral copper hydride and copper deuteride. Likewise, copper hydride has been extensively studied theoretically as a benchmark for the treatment of transition metals,[18-39] as well as to test the treatment of relativistic effects.[40-50] Both Hliwa[24] and Marian[28] have

reported results which are in good agreement with current experimental data on the spectroscopic constants of the low lying $^1\Sigma^+$ states of CuH. They also predict spectroscopic constants for a low lying $^3\Sigma^+$ state which was first identified experimentally in the photoelectron spectra reported here.

The electronic binding energies of the CuH low lying electronic states are similar to the electron binding energies observed in the copper anion 355 nm photoelectron spectrum presented in Figure 6.1. Also presented in Figure 6.1 is an energy level diagram showing the transition energies and term symbols for transitions from the copper anion ground state to the three lowest lying electronic states of neutral copper atom.

The remainder of this Chapter is partitioned as follows. Experimental methods are presented in Section 6.2. Results on CuH^- and CuD^- are presented in Section 6.3, while those on CuH_2^- and CuD_2^- are presented in Section 6.4. Non-trivial spectral assignments are presented in Section 6.5.
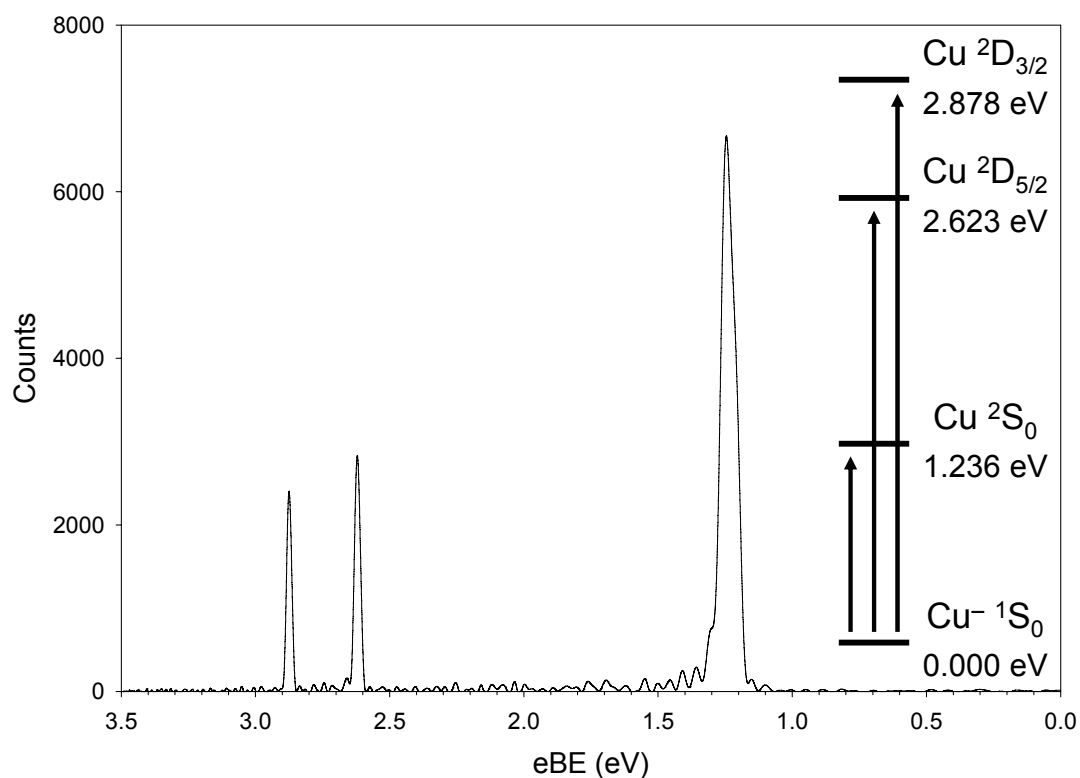
Figure 6.1 Atomic copper anion 355 nm photoelectron spectrum showing transitions from the anion ground state to the three lowest lying electronic states of atomic copper neutral. Transition energies and electronic term symbols are included for reference.

6.2 Experimental Methods

The photoelectron images were obtained using the photoelectron imaging spectrometer with dc discharge copper sputtering source as described in Chapter 2. Copper hydride anions were produced in the dc sputter discharge source by passing argon over a liquid sample of neat methanol before the pulsed valve. Copper deuteride anions were produced by passing argon over a liquid sample of neat d4-methanol. Anion signals of several hundred mV were measured from the inline MCP ion detector for both CuH(D)$^-$ and CuH$_2$(D$_2$)$^-$ with 1600 volts across the detector. The time-of-flight mass spectrum measured

with introduction of d4-methanol in the discharge is presented in Figure 6.2 and labeled with anions of interest. Spectra of the copper-methanol and copper-methoxy anion complexes and analysis are presented in Chapter 7. Because Cu has two naturally occurring isotopes, $\sim 70\%$ ^{63}Cu and $\sim 30\%$ ^{65}Cu, most spectra of the copper-hydrides contain photoelectron features from Cu$^-$. Only the spectra of ^{65}CuD$_2^-$ and ^{65}CuH$_2^-$ are uncontaminated. However, these features can be used to calibrate the spectra, which was the case for all but the above mentioned species.
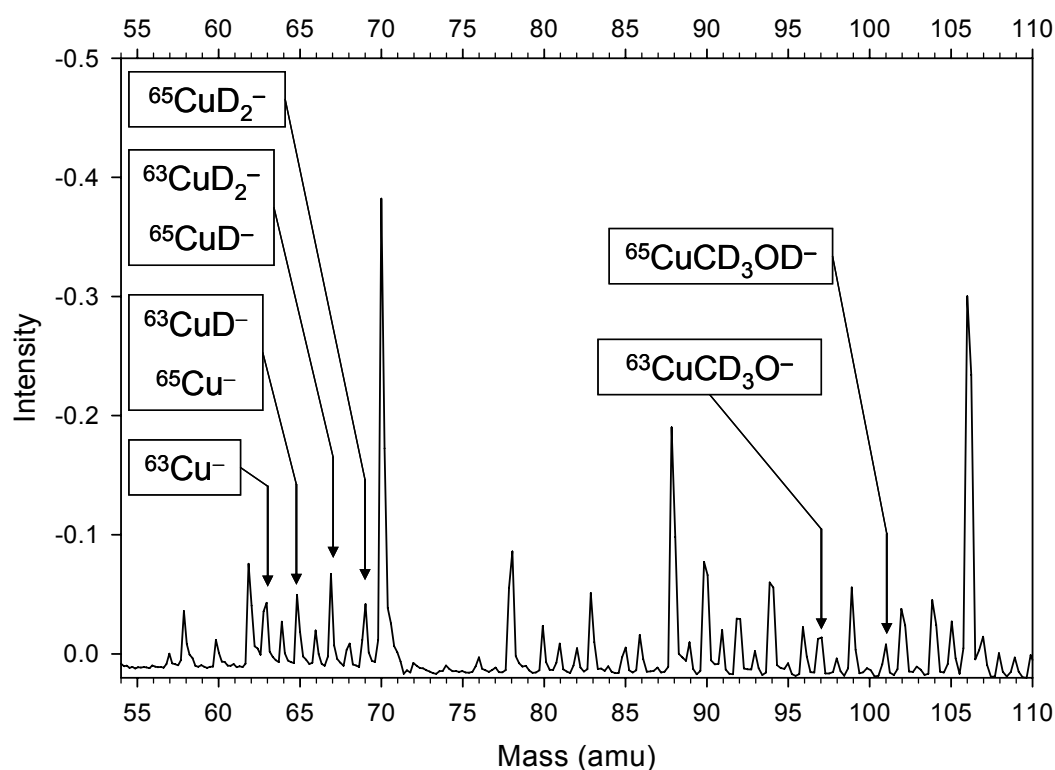
Figure 6.2 Time-of-flight mass spectrum obtained with the dc sputter ion source and d4-methanol with relevant species labeled. Photoelectron imaging spectra of the copper-methanol and copper-methoxy complexes are presented in Chapter 7.

The tripled light (355 nm) from the Infinity laser system was used to take survey scans of CuH(D)$^-$ and CuH$_2$(D$_2$)$^-$ photoelectron spectra by setting the electron imaging optics such that 3.5 eV photoelectrons filled the detector area. The laser power used at 355 nm was

1 – 2 mJ per pulse at a repetition rate of 50 Hz. In order to better resolve the low electron binding energy portions of the photoelectron imaging spectra of CuH(D)$^-$, images were taken using 600 nm laser pulses at 50 Hz produced by the Infinity OPO laser system. Typical pulse energies used were around 1 mJ. In these experiments the electron imaging optics were set such that 2.066 eV (600 nm) photoelectrons filled the detector. The photoelectron images presented here were averaged over 50,000 – 100,000 laser shots. For images taken at 355 nm, observation of transitions to the three lowest lying electronic states[51] of copper neutral were used to calibrate the electron energy scale and to find the optimum electron imaging optics voltage ratio at each magnification. Images taken at 600 nm were calibrated and focused using the transition to the ground state of copper neutral.

The 600 nm spectra of CuH$^-$ and CuD$^-$ contain short vibrational progressions, the fitting of which was used to confirm the spectral assignments. A Franck-Condon simulation of the data using the program PESCAL[52,53] was carried out as follows. The anion and neutral electronic ground states were modeled as Morse oscillators. The neutral parameters (r_e, ω_e, $\omega_e x_e$) were fixed to known literature values.[54] Franck-Condon factors were determined by numerical integration of the Laguerre wave function solutions[55] to the Morse potentials. The instrumental lineshape was modeled as a Gaussian with 45 meV full width at half maximum. Other parameters input into the simulation were the 0-0 transition position and height and the anion temperature (0 K). The only parameter which was allowed to vary was the equilibrium bond length; however the simulation is only sensitive to the change in bond length between the anion and neutral. Thus the change in equilibrium bond lengths between the anion and neutral for the ground states of CuD$^-$ and CuH$^-$ were determined.

6.3   CuH⁻ and CuD⁻ Photoelectron Imaging Results

The 355 nm raw photoelectron image, BASEX reconstructed image, and photoelectron spectrum of ^{63}CuH⁻ are presented in Figure 6.3. The images clearly show five sharp features, two at high electron velocities (outer rings) and three at low electron velocities (inner rings). The two high electron velocity features have angular anisotropies which are aligned with the electric field of the laser (vertical in the images), while the angular distribution of the inner features is more isotropic. Since ^{63}CuH⁻ is 1 amu from both ^{63}Cu⁻ and ^{65}Cu⁻, and the photodetachment cross section is so large for copper anion, the spectrum contains photoelectron features from Cu⁻ photodetachment. However, the photoelectron spectrum of Cu⁻ is well known,[56] thus peaks b and c are assigned as the $^2S_0 \leftarrow {}^1S_0$ and $^2D_{5/2} \leftarrow {}^1S_0$ copper transitions, respectively. Peak d has the correct binding energy for the copper $^2D_{3/2} \leftarrow {}^1S_0$ transition, but the intensity is much too large in comparison to the intensity of peak c (the intensity should be slightly less) for this feature to be assigned purely as the copper $^2D_{3/2} \leftarrow {}^1S_0$ transition. The top trace in Figure 6.3 is the spectrum which results from the subtraction of the measured 355 nm ^{63}Cu⁻ from the bottom spectrum. This spectrum contains photoelectron features only from ^{63}CuH⁻ photodetachment.

The features labeled "a" are assigned as transitions to the ground $X\ ^1\Sigma^+$ state of CuH and are discussed in the presentation of the more resolved 600 nm photoelectron spectrum of CuH⁻ below. Peak e has an electron binding energy of 3.334 (4) eV and is assigned as transitions to the well known[57] excited 2nd $^1\Sigma^+$ state of CuH (refered to as the $A\ ^1\Sigma^+$ in the literature). Peak d has an electron binding energy of 2.862 (7) eV and is assigned as transitions to the predicted,[24,58] but as yet unobserved, 1st $^3\Sigma^+$ state of CuH (given here the state label of $a\ ^3\Sigma^+$). No vibrational progression is observed for transitions to this electronic state, thus the equilibrium bond length of the $a\ ^3\Sigma^+$ state is essentially equal to the equilibrium

bond length of the anion, which is reported below as 1.560 (1) Å. Spectroscopic constants from the literature and this study for CuH⁻ are reported in Table 6.1.

To confirm that peaks d and e are purely electronic transitions, and that the images and spectra reported above do arise from ^{63}CuH⁻ photodetachment, the photoelectron images of ^{63}CuD⁻ were taken at 355 nm under the same experimental conditions as the CuH⁻ images. Figure 6.4 contains the raw photoelectron image, BASEX reconstruction, and photoelectron spectrum of CuD⁻. The images and photoelectron spectrum are very similar to CuH⁻, with the expected exception of the larger contribution from ^{65}Cu⁻ photodetachment, which has the same mass. The peak assignments are the same as for CuH⁻, with slightly different values for the binding and term energies. The differences, however, are well within the experimental uncertainties, thus the results are presented in Table 6.2 without discussion of the assignments. The negligible difference does, however, confirm that the only vibrational structure in the spectrum is found in the lowest binding energy features. These features are examined in greater detail in the 600 nm spectra reported below.
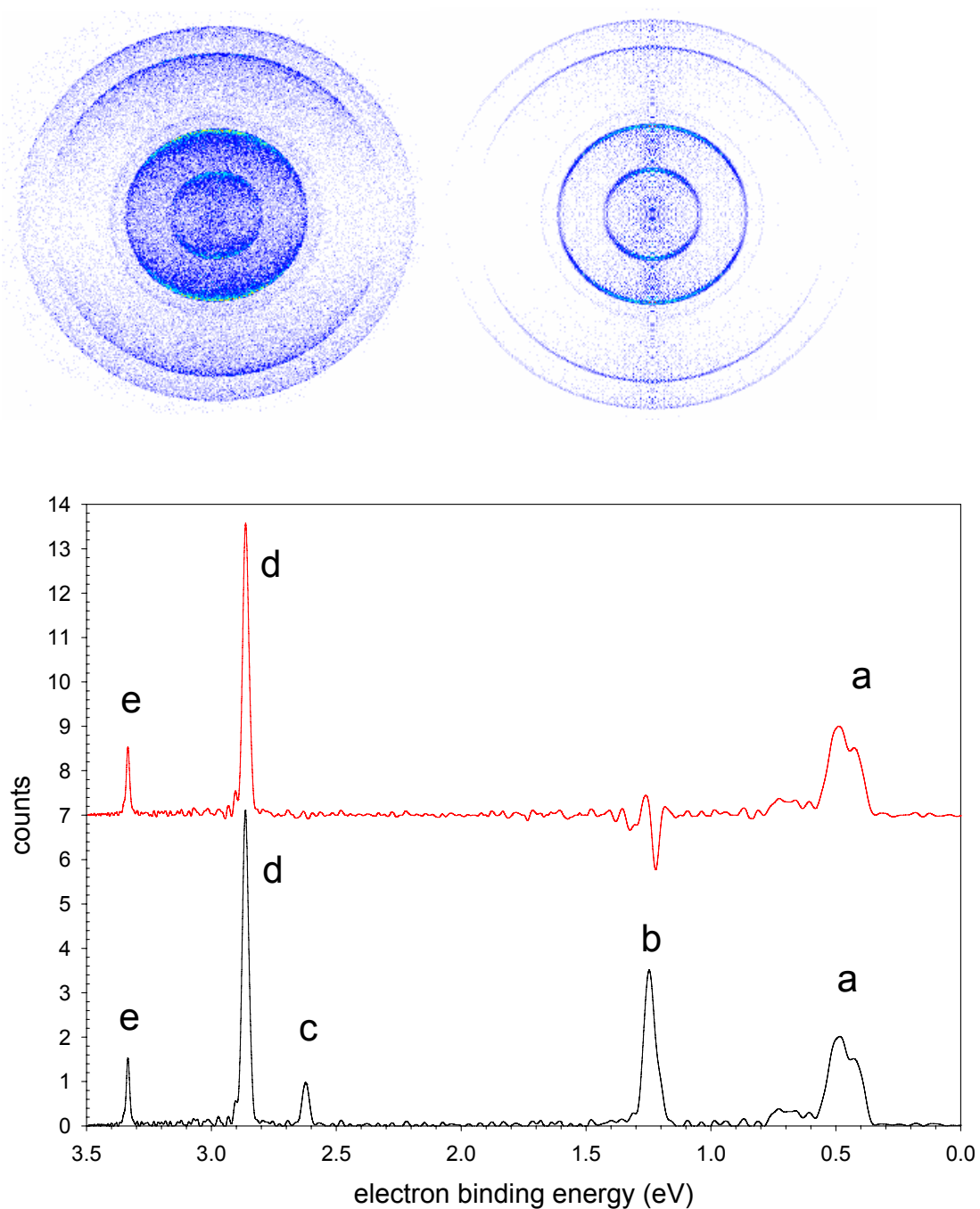
Figure 6.3 ^{63}CuH$^-$ 355 nm full scale raw photoelectron image (top left), BASEX reconstructed photoelectron image (top right), and photoelectron spectrum (bottom). The bottom trace contains features from both ^{63}CuH$^-$ and Cu$^-$ photodetachment, while the Cu$^-$ photodetachment features have been removed in the top trace.
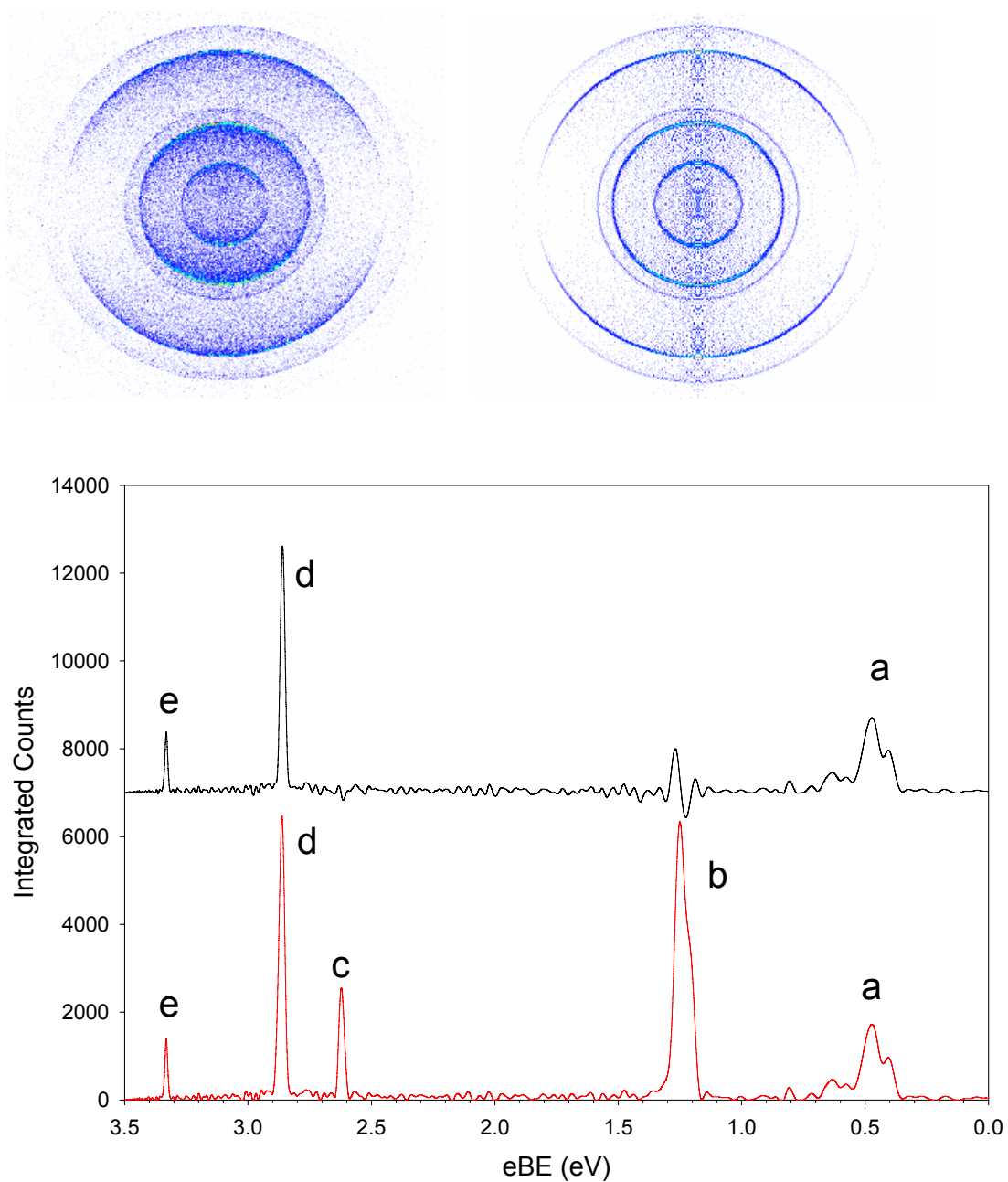
Figure 6.4 $^{63}CuD^-$ 355 nm full scale raw photoelectron image (top left), BASEX reconstructed photoelectron image (top right), and photoelectron spectrum (bottom).   The bottom trace contains features from both $^{63}CuD^-$ and $^{65}Cu^-$ photodetachment, while the $^{65}Cu^-$ photodetachment features have been removed in the top trace.

The 600 nm raw photoelectron image, BASEX reconstructed image, and photoelectron spectrum of CuH^- are presented in Figure 6.5. The low binding energy features in the 355 nm spectra are much more resolved at this photodetachment energy (2.066 eV). As in the 355 nm spectrum, the $^2S_0 \leftarrow {}^1S_0$ copper atom photoelectron transition is observed (peak c), but a vibrational progression in the ground $X\ ^1\Sigma^+$ state of copper hydride is now clearly resolved. Peak a is assigned as the $v = 0$ to $v = 0$ transition, while peak b is assigned as the $v = 0$ to $v = 1$ transition. No hot band transitions are observed in this spectrum, due to the large anion vibrational frequency, which has negligible thermal population at the anion temperature.

Figure 6.5 ^{63}CuH$^-$ 600 nm raw photoelectron image (top left), BASEX reconstructed photoelectron image (top right), and photoelectron spectrum (bottom). The inner feature in the images and the high binding energy feature in the spectrum is detachment from ^{63}Cu$^-$.

As mentioned in the experimental section, the CuH⁻ 600 nm photoelectron spectrum was fit using the known spectroscopic constants for the CuH X $^1\Sigma^+$ electronic ground state listed in Table 6.1. The only adjustable parameters were the change in equilibrium bond length between the anion and neutral, and $0 - 0$ transition position and intensity. These parameters were adjusted manually, and the resulting fit is presented in Figure 6.6 over the data points. The optimized change in bond length from this fit is 0.007 (1) Å. The bond length for the CuH⁻ anion is found to be 1.560 (1) Å, the assignment of which is presented in the discussion section. Since the transition to the a $^3\Sigma^+$ state has no measurable vibrational progression, the bond length of this state is assigned as the bond length of the anion, 1.560 (2) Å, which is in good agreement with the calculated literature[58] value of 1.540 Å. The spectroscopic constants for all the electronic states mentioned in this section are presented in Table 6.1.
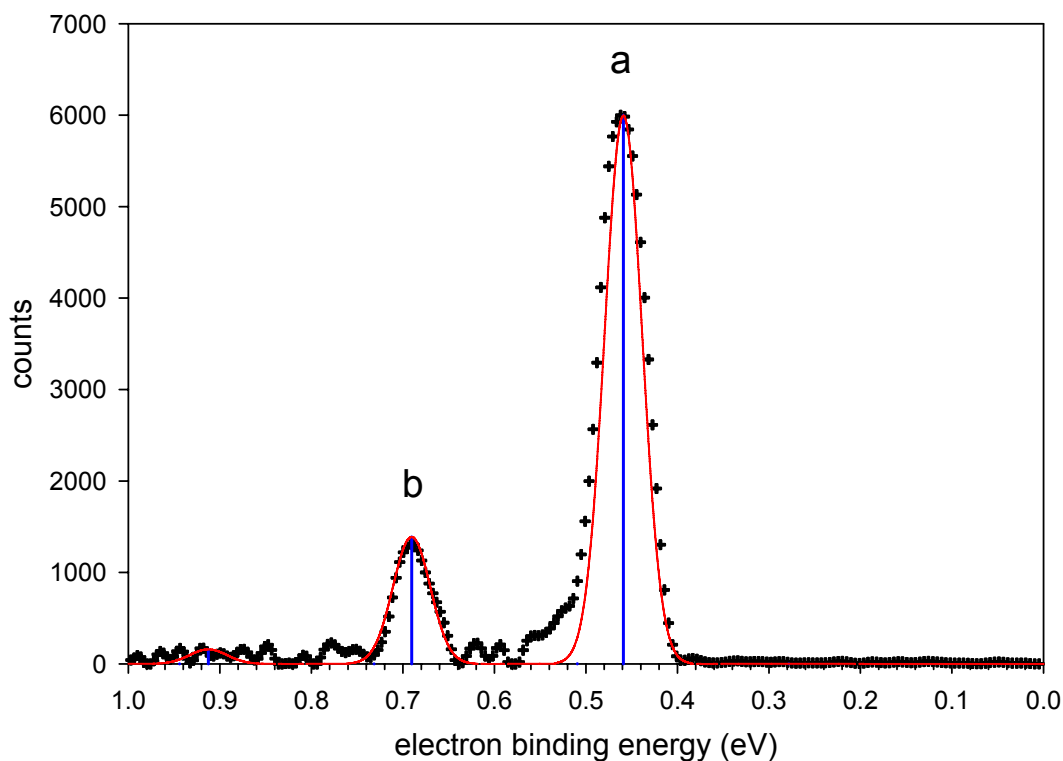
Figure 6.6 ^{63}CuH⁻ 600 nm photoelectron spectrum (points) with calculated Franck-Condon transition positions (sticks) and 45 meV Gaussian convolution (line). The $X\ ^1\Sigma^+$ state ω_e, $\omega_e\chi_e$, and r_e used in the fit are presented in Table 6.1.

Table 6.1   Spectroscopic constants for CuH and CuH⁻.

State	T_e (eV)		ω_e (cm^{-1})	$\omega_e\chi_e$ (cm^{-1})	r_e (Å)	
	this work	lit			this work	lit.
CuH⁻ $X\ ^2\Sigma^+$	−0.430 (5)	–	–	–	1.560 (1)	–
CuH $X\ ^1\Sigma^+$	0	˜0	1941^a	37.51^a	–	1.463^a
CuH $a\ ^3\Sigma^+$	2.436 (5)	2.292^b	1762§	–	1.560 (1)^c	1.540^b
CuH $A\ ^1\Sigma^+$	2.879 (10)	2.905^d	1698^a	44.0^a	–	1.572^a

^{a}from reference 54

^{b}calculated in reference 28

^{c}estimated from lack of vibrational progression, see text

^{d}from reference 57

The ^{63}CuD$^-$ 600 nm photoelectron raw image, BASEX reconstruction, and photoelectron spectrum are presented in Figure 6.7. The spectrum is very similar to the 600 nm ^{63}CuH$^-$ spectrum in that it contains a prominent copper $^2S_0 \leftarrow {}^1S_0$ transition (peak c), but this feature is more intense because the mass of ^{63}CuD$^-$ and ^{65}Cu$^-$ are equal, and thus the amount of copper anion photodetached is much greater than in the copper hydride spectrum. The short vibrational progression was fit, as above, extremely well using the known spectral constants of the ground $X\,{}^1\Sigma^+$ electronic state of CuD listed in Table 6.2. The fit, plotted over the experimental data, is presented in Figure 6.8. The bond length of CuD$^-$ was found to be the same as that of CuH$^-$, 1.560 (1) Å. Similarly, the lack of a vibrational progression in transitions to the $a\,{}^3\Sigma^+$ state of CuD sets the bond length of this state as that of the anion. The known spectral constants for the electronic states of CuD and CuD$^-$ mentioned in this section are presented in Table 6.2.
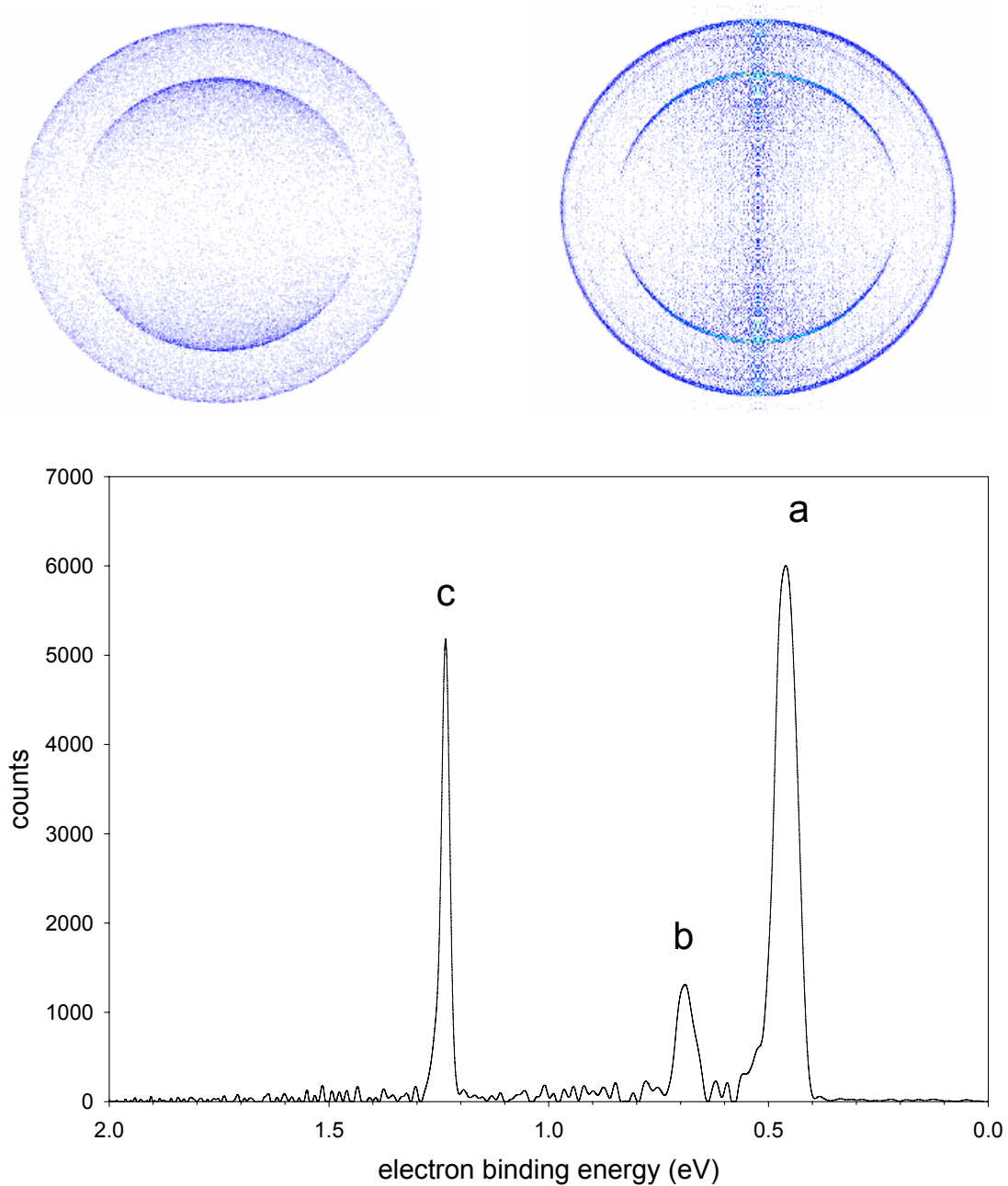
Figure 6.7 $^{63}CuD^-$ 600 nm raw photoelectron image (top left), BASEX reconstructed photoelectron image (top right), and photoelectron spectrum (bottom). The inner feature in the images and the high binding energy feature in the spectrum is detachment from $^{65}Cu^-$.
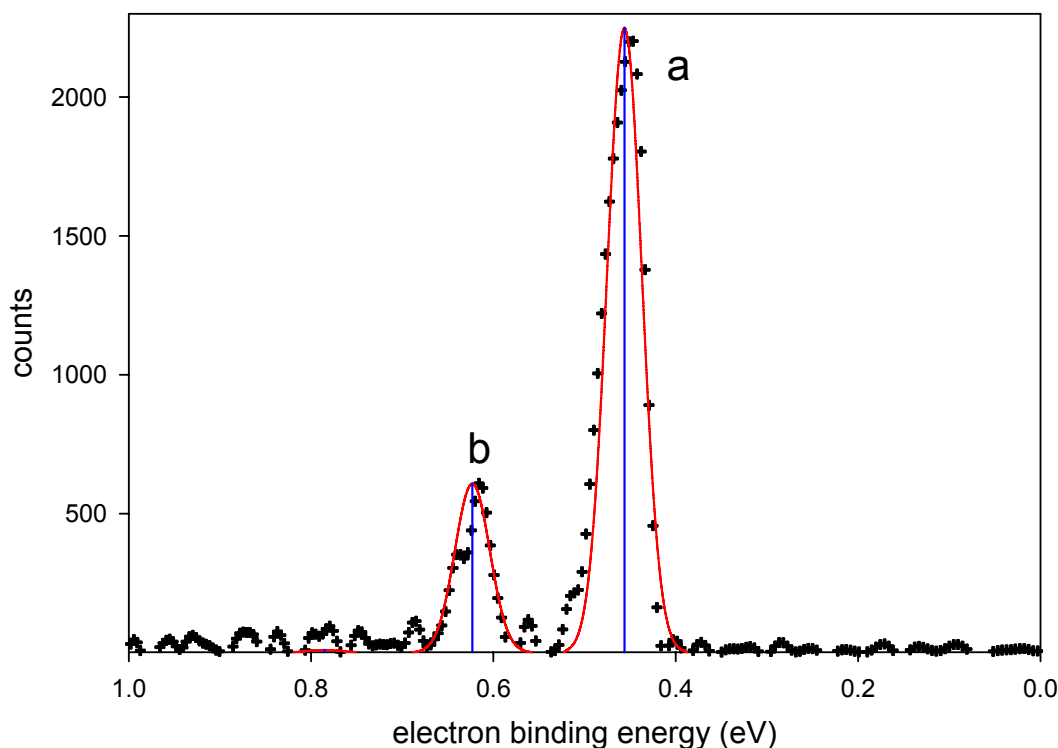
Figure 6.8 ^{63}CuD$^-$ 600 nm photoelectron spectrum with calculated Franck-Condon transition positions (sticks) and 45 meV Gaussian convolution (line). The $X\,^1\Sigma^+$ state ω_e, $\omega_e\chi_e$, and r_e used in the fit are presented in Table 6.2.

Table 6.2   Spectroscopic constants for CuD and CuD$^-$.

| State | T_e (eV) | | ω_e (cm^{-1}) | $\omega_e\chi_e$ (cm^{-1}) | r_e (Å) | |
	this work	lit			this work	lit.
CuD$^-$ $X\,^2\Sigma$	−0.427 (5)	–	–	–	1.560 (1)	–
CuD $X\,^1\Sigma^+$	0	0	1384^a	18.97^a	–	1.463^a
CuD $a\,^3\Sigma^+$	2.437 (5)	2.417^b	1174^b		1.560 (2)^c	–
CuD $A\,^1\Sigma^+$	2.877 (10)	2.892^d	1210^d	1210^d	–	1.566^d

^{a} From reference 54

^{b} Calculated in reference 28

^{c} Estimated from lack of vibrational progression, see text

^{d} From reference 57

6.4   CuH$_2^-$ and CuD$_2^-$ Photoelectron Imaging Results

The 355 nm full scale CuH$_2^-$ raw photoelectron image, BASEX reconstruction, and photoelectron spectrum are presented in Figure 6.9. The images contain two noticeable features at low electron velocity (center of the image) and no other photoelectron features. The photoelectron spectrum confirms this finding, as the only features in the spectrum are at high electron binding energies (low electron velocities). This is markedly different from the copper hydride anion photoelectron spectra above which contain features at low electron binding energies. The photoelectron spectrum also clearly shows low intensity photoelectron features between peak a and the photon energy (3.493 eV). In order to better utilize the photoelectron detector, the electron optics were adjusted such that the CuH$_2^-$ photodetachment features nearly filled the detector.

Figure 6.9 $^{65}CuH_2^-$ 355 nm full scale raw photoelectron image (top left), BASEX reconstructed photoelectron image (top right), and photoelectron spectrum (bottom).

The magnified CuH_2^- 355 nm raw photoelectron image, BASEX reconstruction, and photoelectron spectrum are presented in Figure 6.10. The images show low intensity photoelectron features, as well as the two significant photoelectron features mentioned above.

The photoelectron spectrum confirms the low intensity photoelectron features which start at the most intense feature (peak a) and continue to the photon energy (3.493 eV). Peak a has an electron binding energy of 2.852 (2) eV and peak b has an electron binding energy of 3.086 (2) eV. The splitting between the peaks is 0.234 (2) eV or 1879 (57) cm^{-1}. The angular anisotropy parameters of peaks a and b have been measured as $\beta = 1.8$ (1) for peak a and $\beta = 1.9$ (1) for peak b.
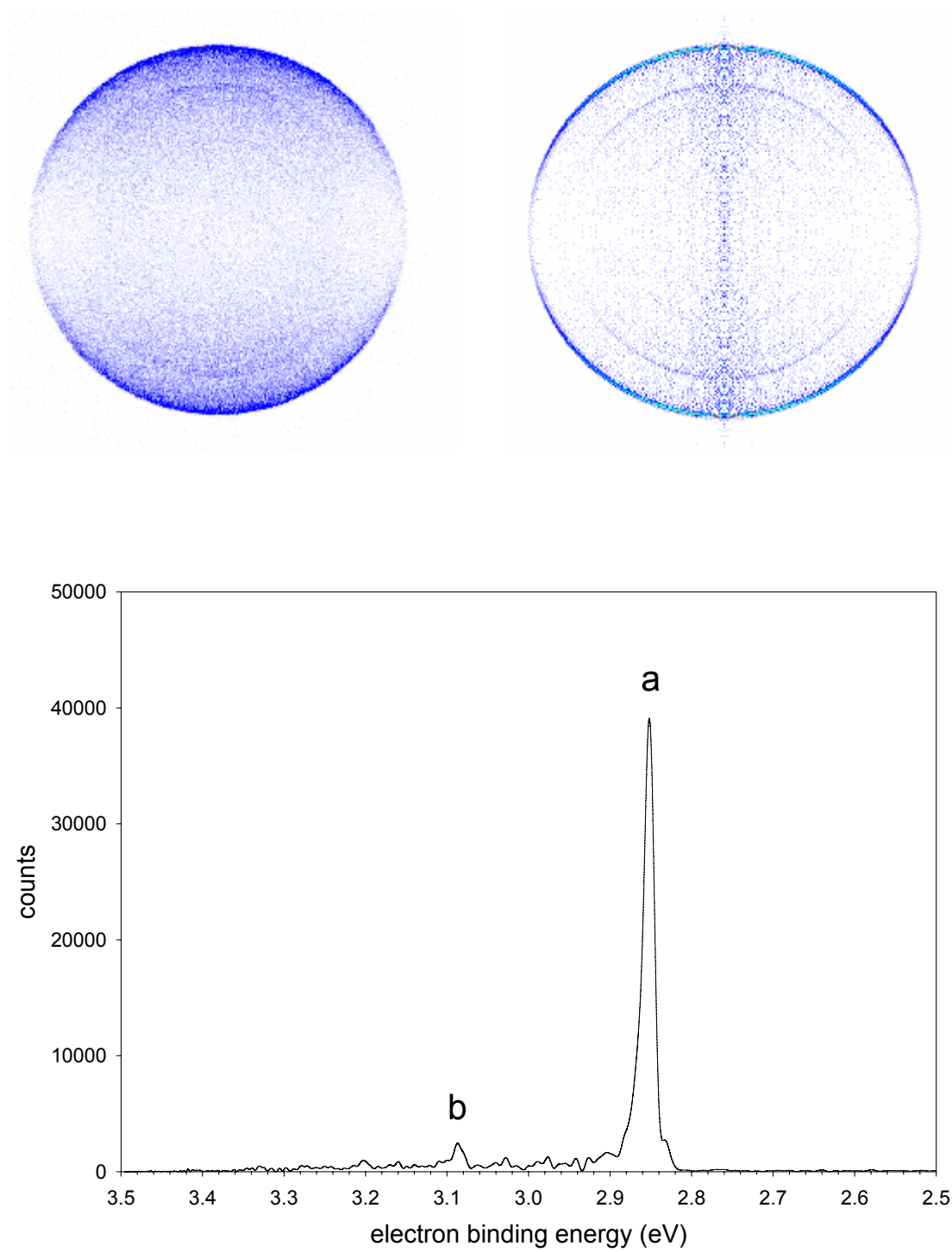
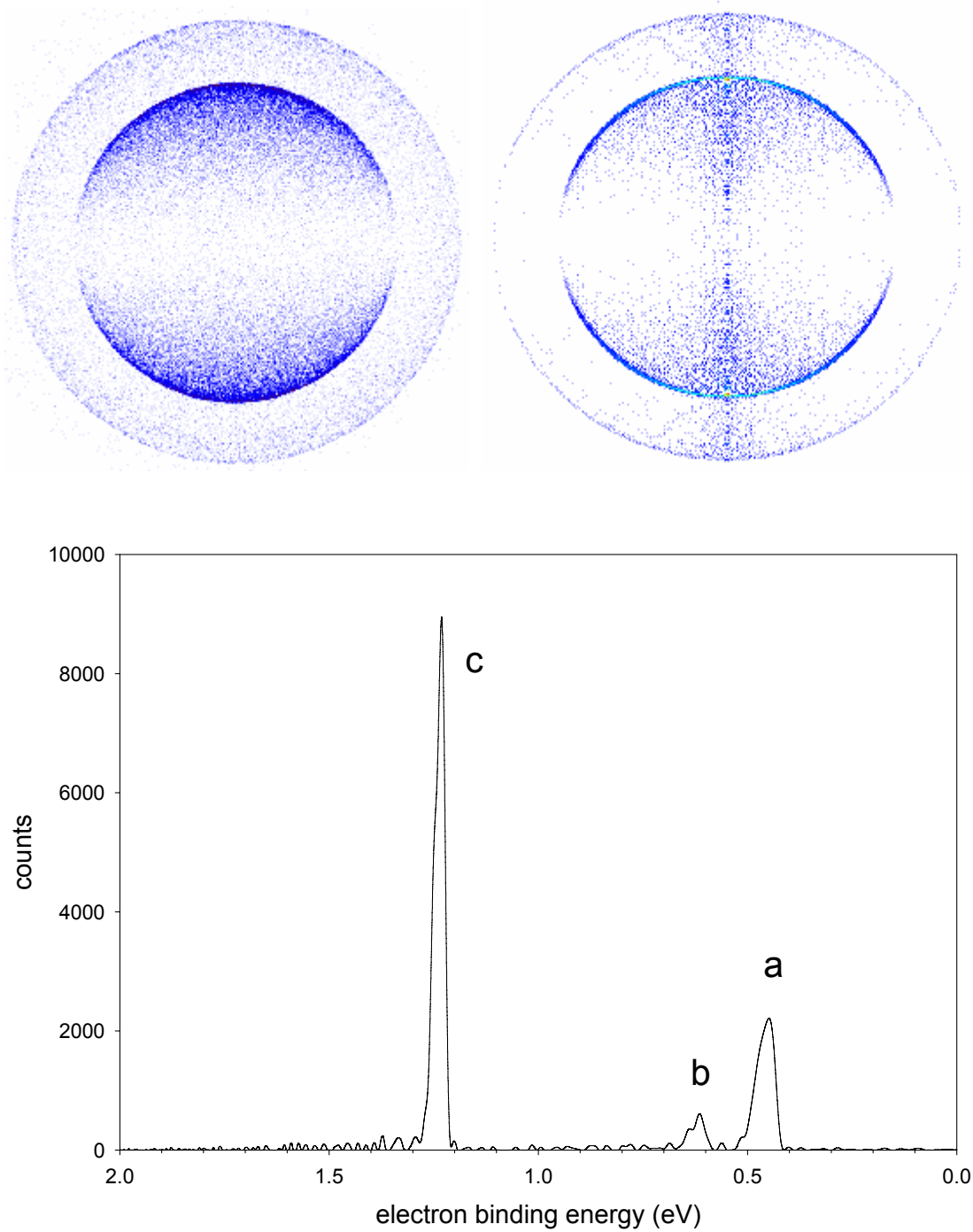**Figure 6.10** $^{65}CuH_2^-$ 355 nm 0 – 1 eV eKE raw photoelectron image (top left), BASEX reconstructed photoelectron image (top right), and photoelectron spectrum (bottom).

Figure 6.11 shows the same portion of the CuH_2^- photoelectron spectrum as above with the intensity scale reduced by a factor of 10. In addition the measured intensities have been scaled by $(eKE)^{\ell+1/2}$ where $\ell = 1$ is the angular momentum of an outgoing p-wave. This scaling assumes that the electron is detached from an orbital of predominantly d character near threshold, a reasonable assumption given the high electron binding energy of the features and the low electron kinetic energy (less than 1 eV). This procedure reveals a spectrum with a large amount of structure. There appear to be groups of multiplet peaks, with the spacing between the groups ranging from 440 cm^{-1} to 190 cm^{-1}.

Figure 6.11 $^{65}CuH_2^-$ 355 nm 0 − 1 eV photoelectron spectrum with the photoelectron intensity scaled to show the low intensity structure.

The 355 nm CuD_2^- raw photoelectron image, BASEX reconstructed image, and photoelectron spectrum are presented in Figure 6.12. As expected, the images show the same basic structure of the CuH_2^- images, with photoelectrons observed at low electron velocities (inner rings) and not at high electron velocities (no outer rings). As in CuH_2^-, low intensity photoelectron structure extends from the lowest binding energy peak (a) to the highest binding energy measurable at this photon energy (3.493 eV). Unlike the CuH_2^- photoelectron spectrum, however, the spacing of peaks a and b is significantly smaller in the CuD_2^- spectrum. As was done with CuH_2^-, the electron optics were adjusted such that the largest photoelectron kinetic energy measured was 1 eV.
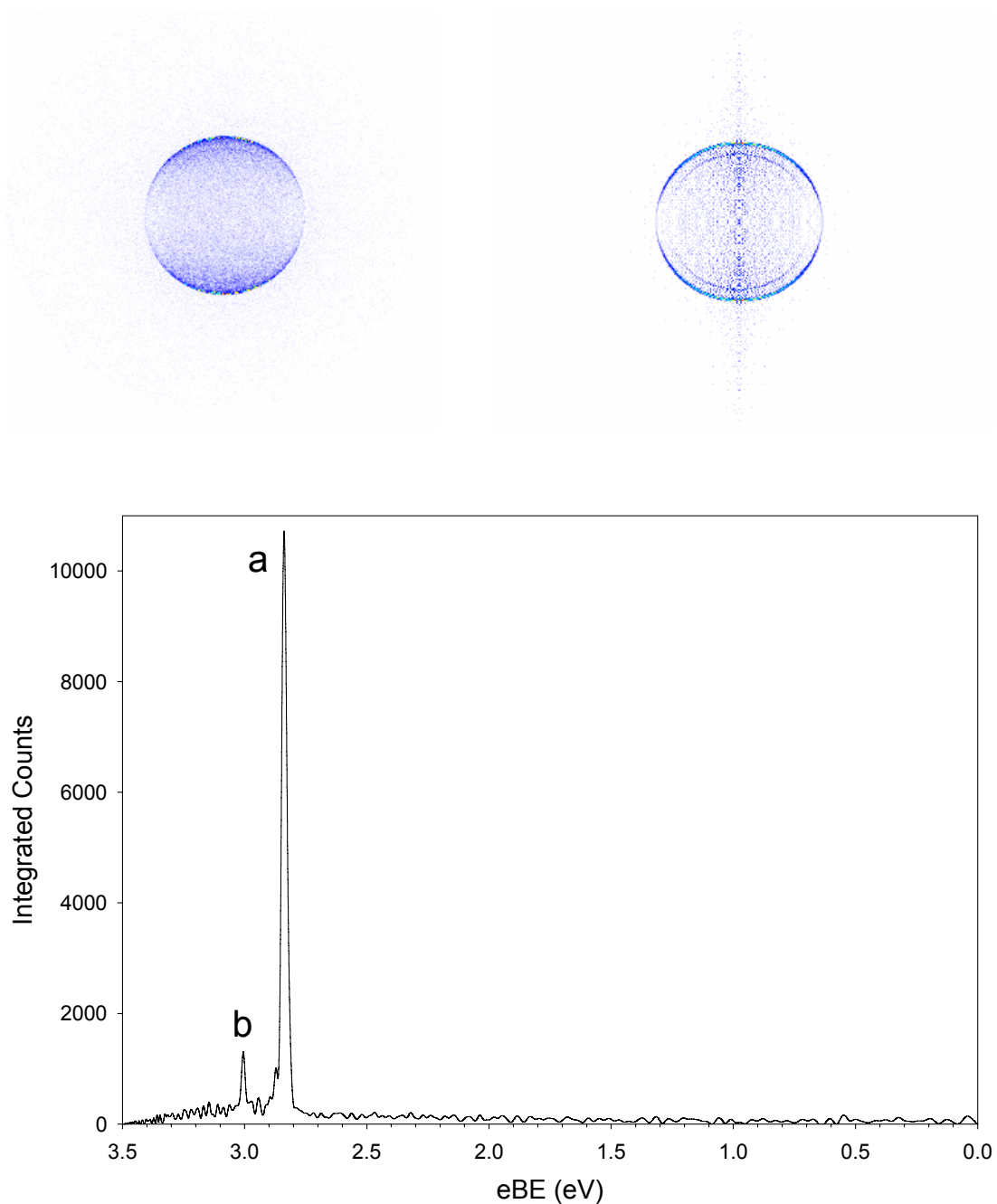
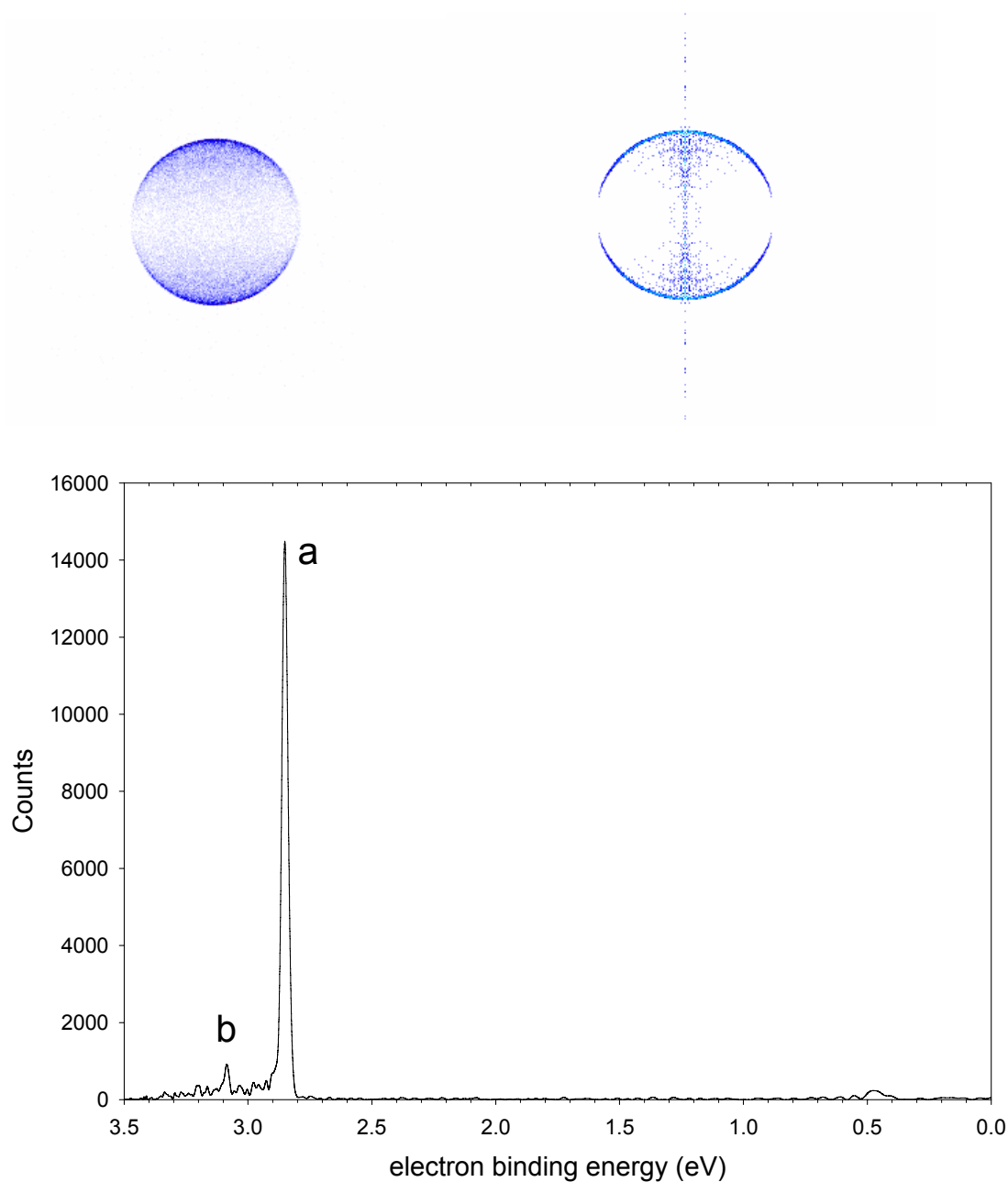**Figure 6.12** $^{65}CuD_2^-$ 355 nm full scale raw photoelectron image (top left), BASEX reconstructed photoelectron image (top right), and photoelectron spectrum (bottom).

The CuD_2^- 355 nm 0 – 1 eV electron kinetic energy raw photoelectron image, BASEX reconstruction, and photoelectron spectrum are presented in Figure 6.13.   The images show that the main features (peaks a and b) have very similar angular anisotropies.

The measured angular anisotropies are $\beta = 1.8$ (1) for peak a and $\beta = 1.8$ (1) for peak b, suggesting that these features are detachment to the same electronic state of the neutral. The electron binding energies of peaks a and b are 2.841 (5) eV and 3.008 (5) eV, respectively. The energy splitting of peaks a and b is 1348 (57) cm^{-1}, considerably less than the 1879 (57) cm^{-1} of the corresponding features in the CuH_2^- 355 nm photoelectron spectrum. The significant lowering of this energy upon deuteration strongly suggests that these are vibrational, not electronic, features. The electron binding energy, peak spacing, and angular anisotropy parameters observed in the photoelectron spectra of CuH_2^- and CuD_2^- are presented in Table 6.3.

Table 6.3   Electron binding energies, angular anisotropy parameters, and peak spacings in the CuH_2^- and CuD_2^- photoelectron spectra.

peak	CuH$_2$			CuD$_2$		
	eBE (eV)	β	b – a (cm^{-1})	eBE (eV)	β	b – a (cm^{-1})
a	2.851 (5)	1.8 (1)	1879 (57)	2.841 (5)	1.8 (1)	1348 (57)
b	3.086 (5)	1.9 (1)		3.008 (5)	1.8 (1)	
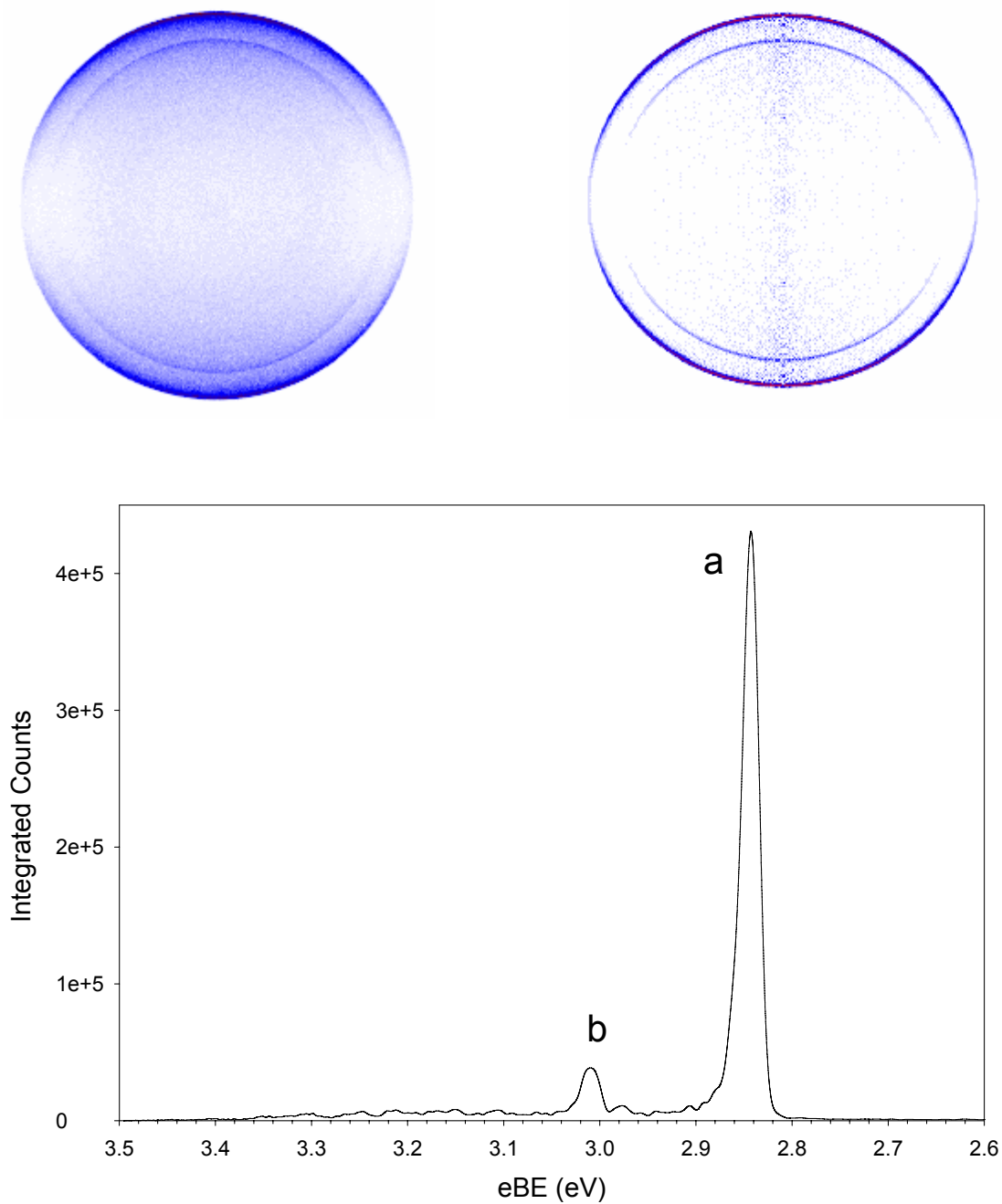
Figure 6.13 $^{65}CuD_2^-$ 355 nm expanded photoelectron raw image (top left), BASEX reconstructed image (top right), and photoelectron spectrum (bottom).

Figure 6.14 shows the same portion of the CuD_2^- photoelectron spectrum as above with the intensity scale reduced by a factor of 10. In addition the measured intensities have been scaled by (eKE) $^{\ell+1/2}$ where $\ell = 1$ is the angular momentum of an outgoing p-wave. This

scaling assumes that the electron is detached from an orbital of predominantly d character near threshold, a reasonable assumption given the high electron binding energy of the features and the low electron kinetic energy (less than 1 eV). This procedure reveals a spectrum with a large amount of structure. There appear to be groups of multiplet peaks, with the spacing between the groups ranging from 350 cm^{-1} to 550 cm^{-1}.
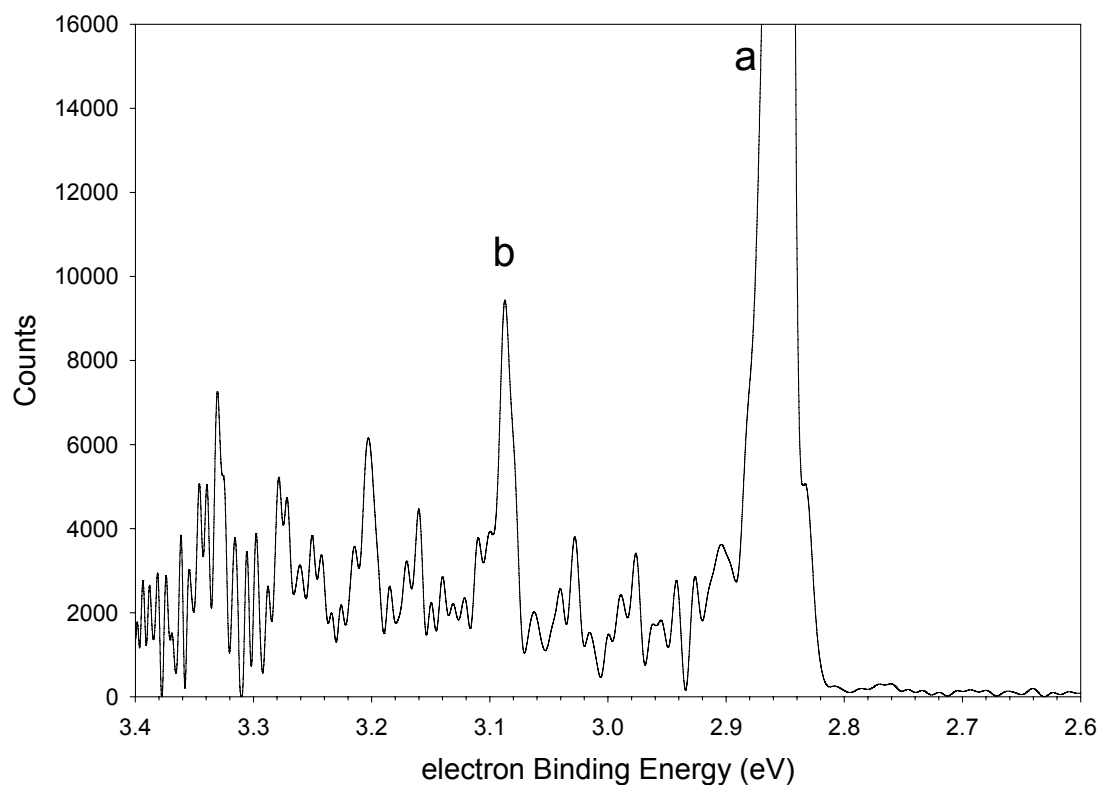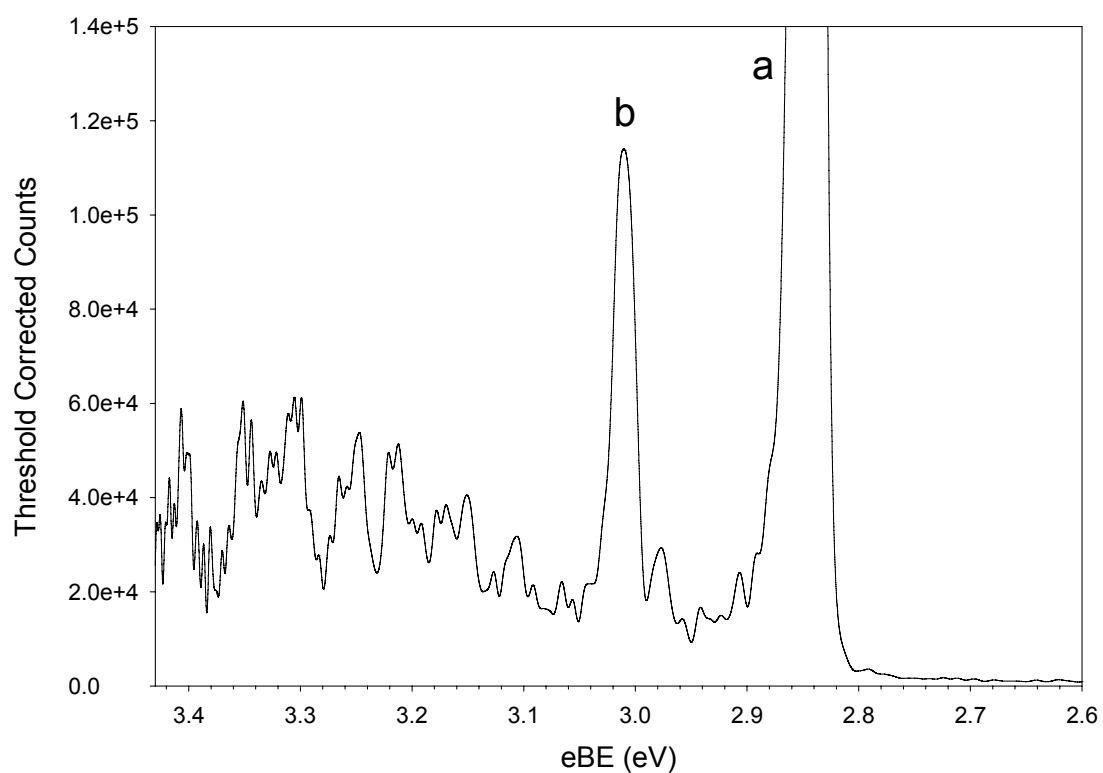

Figure 6.14 ^{65}CuD$_2^-$ 355 nm 0 – 1 eV scale photoelectron spectrum. The counts have been threshold corrected as explained in the text and the photoelectron intensity has been increased by a factor of 10.

6.5   Discussion

As mentioned in the CuH$^-$ and CuD$^-$ results section, the equilibrium bond length of the copper hydride anion is assigned to be longer than the equilibrium bond length of the

neutral molecule. There are both theoretical and experimental reasons why this should be true. Theoretically, the ground state molecular orbital configuration for copper hydride arises from a combination of Cu $3d^{10}4s^1$ and H $1s^1$. These atomic orbitals combine to give a bonding (Cu$3d^{10}4s^1$ H$1s^1$) σ orbital and an anti-bonding (Cu$3d^{10}4s^1$ H$1s^1$) σ^* orbital. The neutral ground state has a σ^2 configuration, while the ground state of the anion has a $\sigma^2\sigma^{*1}$ configuration. The addition of the extra electron in the anion into an anti-bonding orbital should cause an increase in the equilibrium bond length.

The experimental evidence gives additional weight to this argument. Only transitions from the anion to the ground vibrational level in the 2nd $^1\Sigma^+$ (literature A) state of CuH and CuD are observed. In the case of the CuH⁻ photoelectron spectrum, the photodetachment energy (3.493 eV) is just below the binding energy of the first vibrationally excited state in the 2nd $^1\Sigma^+$ manifold (3.545 eV). However, the binding energy of the first vibrationally excited state of the 2nd $^1\Sigma^+$ state of CuD is within our photodetachment energy at 3.481 eV binding energy. There is no significant photoelectron intensity at this binding energy in the 355 nm spectra, thus the equilibrium bond length of the anion and the 2nd $1\Sigma^+$ state must be essentially equal. The bond length of this state is well known as 1.566 Å, thus the equilibrium bond length of the copper hydride anion is set higher than the bond length of the neutral.

The assignments of the CuH$_2$⁻ and CuD$_2$⁻ spectra are more difficult. Foremost, it is not clear if the photoelectron features arise from the ground electronic state, or from an excited electronic state. Wang[3] has calculated the difference in energy between CuH$_2$⁻ and CuH$_2$ to be 2.34 eV at the BPW91/6-311++G(d,p)/SDD level of theory, though it is not stated if this difference includes zero-point energy. It is certainly possible that the calculation is in error by 500 meV, or that the exclusion of zero-point energy would cause a shift of this magnitude. The angular anisotropy parameters should give an idea if the observed

photoelectron originate from a sigma or delta orbital of the anion. The observed angular anisotropy parameters are near 1.8 for the main features in the spectrum, which suggests that the outgoing photoelectron has mostly p-wave character. However, a p-wave may be produced upon removal of an electron from a sigma type orbital, or from a delta type orbital where the outgoing electron is near threshold. The electron kinetic energies of the observed features are less than 700 meV, making them all "near threshold", so the anisotropy parameters also provide little guidance.

Assuming the features are transitions to the electronic ground state, peak a would be the electron affinity while peak b would be assigned as having one quantum of the symmetric stretch excited in the photoelectron transition (Wang calculates the symmetric stretch of CuH_2 neutral as 1770 cm^{-1}). Wang calculates the anion to be linear and symmetric ($^1\Sigma_g^+$) with a Cu – H distance of 1.560 Å. Wang calculates the neutral to be bent and symmetric ($^2B_2$) with a H – Cu – H bond angle of 122.6° and Cu – H bond lengths of 1.527 Å. If these calculations are correct, then both the bend and the symmetric stretch vibrations should be excited in the photoelectron spectrum. However, since there is such a large geometry change in the bending coordinate (from linear to highly bent), these transitions would have poor vibrational overlap in the Franck-Condon approximation in the observed region of the spectrum. The use of a higher energy photon for photodetachment may reveal that the low intensity peaks are merely the onset of an extended vibrational progression. The bend frequency calculated by Wang is 637 cm^{-1} for CuH_2, which is larger than the observed low intensity peak spacings. The observed peaks may be combination bands of the bend, symmetric stretch, or even quanta of the symmetric stretch. Unfortunately, the spectrum is too congested and the calculated frequencies too uncertain to accurately assign each peak in the observed spectrum in this way. Of course the same arguments could be true for an excited electronic state of CuH_2, though there have been no geometries or frequencies

calculated for excited states of CuH_2 to date. The most likely conclusion, however, is that the observed features are transitions to the ground state of CuH_2 and CuD_2. As stated above, this would identify peak a as the electron affinity of CuH_2 and CuD_2 and peak b as excitation of one quanta of the symmetric stretch mode.

Table 6.4   Electron affinities and symmetric stretch frequencies for CuH_2 and CuD_2.

	CuH_2		CuD_2	
	this work	**literature**[a]	**this work**	**literature**[a]
electron affinity (eV)	2.851 (5)	2.34	2.841 (5)	2.34
symmetric stretch frequency (cm^{-1})	1879 (57)	1770	1348 (57)	−

[a] From reference 3

References for Chapter VI

[1]   L. Andrews and X. Wang, *Journal of the American Chemical Society* **125** (38), 11751 (2003).

[2]   X. Wang and L. Andrews, *Angewandte Chemie, International Edition* **42** (42), 5201 (2003).

[3]   X. Wang, L. Andrews, L. Manceron, and C. Marsden, *Journal of Physical Chemistry A* **107** (41), 8492 (2003).

[4]   M. Ebben, G. Meijer, and J. J. Ter Meulen, *Applied Physics B: Photophysics and Laser Chemistry* **B50** (1), 35 (1990).

[5]   R. Georgiadis, E. R. Fisher, and P. B. Armentrout, *Journal of the American Chemical Society* **111** (12), 4251 (1989).

[6]   V. N. Belyaev, N. L. Lebedeva, K. S. Krasnov, and L. V. Gurvich, *Izvestiya Vysshikh Uchebnykh Zavedenii, Khimiya i Khimicheskaya Tekhnologiya* **21** (11), 1698 (1978).

[7]   A. Kant and K. A. Moon, *High Temperature Science* **11** (1), 55 (1979).

[8]   V. M. Rao, M. L. P. Rao, and P. T. Rao, *Journal of Quantitative Spectroscopy & Radiative Transfer* **25** (6), 547 (1981).

[9]   R. Burtovyy, E. Utzig, and M. Tkacz, *Thermochimica Acta* **363** (1-2), 157 (2000).

[10]   R. Burtovyy, D. Wlosewicz, A. Czopnik, and M. Tkacz, *Thermochimica Acta* **400** (1-2), 121 (2003).

[11]   A. M. Antic-Jovanovic and D. S. Pesic, *Glasnik Hemijskog Drustva Beograd* **34** (2-4), 163 (1969).

[12]   C. M. Brown and M. L. Ginter, *Journal of Molecular Spectroscopy* **80** (1), 145 (1980).

[13]   U. Ringstroem, *Canadian Journal of Physics* **46** (20), 2291 (1968).

[14]   P. F. Bernath, *AIP Conference Proceedings* **146** (Adv. Laser Sci. - 1), 443 (1986).

[15]   T. D. Varberg and K. M. Evenson, *Journal of Molecular Spectroscopy* **164** (2), 531 (1994).

[16]   R. B. Wright, J. K. Bates, and D. M. Gruen, *Inorganic Chemistry* **17** (8), 2275 (1978).

[17]   M. C. McCarthy and R. W. Field, *Journal of Chemical Physics* **100** (9), 6347 (1994).

[18]   V. Barone and C. Adamo, *International Journal of Quantum Chemistry* **61** (3), 443 (1997).

[19]   V. Barone and C. Adamo, *Journal of Physical Chemistry* **100** (6), 2094 (1996).

[20]   P. Belohorec, S. M. Rothstein, and J. Vrbik, *Journal of Chemical Physics* **98** (8), 6401 (1993).

[21]   J. C. A. Boeyens and R. H. Lemmer, *Journal of the Chemical Society, Faraday Transactions 2: Molecular and Chemical Physics* **73** (3), 321 (1977).

[22]   G. Das, *Journal of Chemical Physics* **74** (10), 5766 (1981).

[23] P. Fantucci, S. Polezzo, G. Morosi, and V. Valenti, *Theoretica Chimica Acta* **67** (3), 245 (1985).

[24] M. Hliwa, J. C. Barthelat, M. Pelissier, and F. Spiegelmann, *Chemical Physics Letters* **132** (2), 205 (1986).

[25] S. Hoyau and G. Ohanessian, *Chemical Physics Letters* **280** (3,4), 266 (1997).

[26] J. Hrusak, S. Ten-No, and S. Iwata, *Journal of Chemical Physics* **106** (17), 7185 (1997).

[27] V. V. Karasiev, *Theochem* **493**, 21 (1999).

[28] C. M. Marian, *Journal of Chemical Physics* **94** (8), 5574 (1991).

[29] M. Merchan, J. P. Daudey, R. Gonzalez-Luque, and I. Nebot-Gil, *Chemical Physics* **148** (1), 69 (1990).

[30] N. Minh Tho, M. A. McGinn, and N. J. Fitzpatrick, *Journal of the Chemical Society, Faraday Transactions 2: Molecular and Chemical Physics* **82** (9), 1427 (1986).

[31] C. Opitz and H. H. Dunken, *Zeitschrift fuer Physikalische Chemie (Leipzig)* **249** (3-4), 154 (1972).

[32] M. Pelissier, J. P. Daudey, J. P. Malrieu, and G. H. Jeung, *NATO ASI Series, Series C: Mathematical and Physical Sciences* **176** (Quantum Chem.: Challenge Transition Met. Coord. Chem.), 37 (1986).

[33] R. Pou-Amerigo, M. Merchan, I. Nebot-Gil, P. A. Malmqvist, and B. O. Roos, *Journal of Chemical Physics* **101** (6), 4893 (1994).

[34] K. Raghavachari, K. K. Sunil, and K. D. Jordan, *Journal of Chemical Physics* **83** (9), 4633 (1985).

[35] S. M. Rothstein, *International Journal of Quantum Chemistry* **60** (4), 803 (1996).

[36] G. Simons and E. R. Talaty, *Journal of Chemical Physics* **66** (6), 2457 (1977).

[37]   H. Smithson, C. A. Marianetti, D. Morgan, A. Van der Ven, A. Predith, and G. Ceder, *Physical Review B: Condensed Matter and Materials Physics* **66** (14), 144107/1 (2002).

[38]   C. Zhang and A. Alavi, *Journal of the American Chemical Society* **127** (27), 9808 (2005).

[39]   T. Ziegler, V. Tschinke, and A. Becke, *Journal of the American Chemical Society* **109** (5), 1351 (1987).

[40]   C. L. Collins, K. G. Dyall, and H. F. Schaefer, III, *Journal of Chemical Physics* **102** (5), 2024 (1995).

[41]   V. Kello and A. J. Sadlej, *Theochem* **547**, 35 (2001).

[42]   V. Kello and A. J. Sadlej, *Theoretica Chimica Acta* **92** (4), 253 (1995).

[43]   V. Kelloe and A. J. Sadlej, *Journal of Chemical Physics* **95** (11), 8248 (1991).

[44]   V. Kelloe and A. J. Sadlej, *Theoretica Chimica Acta* **94** (2), 93 (1996).

[45]   V. Kelloe, A. J. Sadlej, and B. A. Hess, *Journal of Chemical Physics* **105** (5), 1995 (1996).

[46]   J. Micanko and S. Biskupic, *ACH - Models in Chemistry* **137** (5-6), 753 (2000).

[47]   J. Onoe, *Advances in Quantum Chemistry* **37**, 311 (2001).

[48]   J. Onoe, H. Nakamatsu, T. Mukoyama, R. Sekine, H. Adachi, and K. Takeuchi, *Journal of the Physical Society of Japan* **65** (8), 2459 (1996).

[49]   T. Suzumura, T. Nakajima, and K. Hirao, *International Journal of Quantum Chemistry* **75** (4/5), 757 (1999).

[50]   C. van Wullen, *Journal of Chemical Physics* **109** (2), 392 (1998).

[51]   J. Sugar and A. Musgrove, *Journal of Physical and Chemical Reference Data* **19**, 527 (1990).

[52]   K. M. Ervin, Fortran PESCAL (Reno, NV, 2001).

[53]   K. M. Ervin, T. M. Ramond, G. E. Davico, R. L. Schwartz, S. M. Casey, and W. C. Lineberger, *Journal of Physical Chemistry A* **105** (48), 10822 (2001).

[54]   K. Huber and G. Herzberg, *Molecular Spectra and Molecular Structure, Constants of Diatomic Molecules*. (Van Nostrand-Reinhold, New York, 1979).

[55]   K. Cashion, *Journal of Molecular Spectroscopy* **10**, 182 (1963).

[56]   J. Ho, K. M. Ervin, and W. C. Lineberger, *Journal of Chemical Physics* **93** (10), 6987 (1990).

[57]   U. Ringstrom, *Arkiv For Fysik* **32**, 211 (1966).

[58]   C. M. Marian, *The Journal of Chemical Physics* **94** (8), 5574 (1991).

_____

Photoelectron Velocity Map Imaging of CuCD$_3$O⁻ and CuCD$_3$OD⁻

_____

7.1   Introduction

This chapter presents results of photoelectron imaging experiments conducted on the Cu⁻CD$_3$OD anion.   The experiment was designed to help define the initial state of a photodetachment-photoionization (PDPI) experiment conducted on the same complex. In the PDPI experiments, mass-selected [65]Cu⁻CD$_3$OD was photodetached by a femtosecond laser pulse near 400 nm, allowed to evolve on the gound neutral electronic state surface, then probed at different time delays via resonance enhanced multi photon ionization coupled with mass spectral detection of the product cations. Photoelectron spectroscopy coupled with high level spectral simulations is employed here to elucidate the geometry and thermodynamics of the neutral state formed immediately after electron photodetachment of Cu⁻CD$_3$OD.

Previously Cu⁻H$_2$O was studied using the same techniques described above. In those studies[1-4] it was found that a modest potential well exists in the radial Cu − O coordinate of the neutral complex at the geometry of the anion on the electronic ground state surface. The geometry of the anion was found to have the water hydrogen atoms between the copper atom (which carries much of the excess negative charge) and the oxygen atom, while the hydrogen atoms are located further from the copper atom than the oxygen atom in the neutral complex. Because of this very large difference in geometry between the lowest energy geometries of the anion and neutral complexes, transitions from the anion to the lowest energy geometry of the neutral were not observed in the photoelectron spectra, due to negligible vibrational Frank-Condon factors. Instead, transitions were observed to the neutral complex at the anion geometry.

The ground electronic state of CuH_2O was found[2] to result from removal of an electron localized on copper, correlating to the Cu 4s orbital, based on an angular photoelectron anisotropy parameter of $\beta = 2$. Excited electronic states of CuH_2O were accessed via removal of electrons from the copper 3d orbital. Electrons photodetached from this state had an angular anisotropy parameter of $\beta = 0.2$. The electronic binding energies of these orbitals is very similar to that of the electron binding energies of the observed in the copper anion 355 nm photoelectron spectrum presented in Figure 7.1. Also presented in Figure 7.1 is an energy level diagram showing the transition energies and term symbols for transitions from the copper anion ground state to the three lowest lying electronic states of neutral copper.
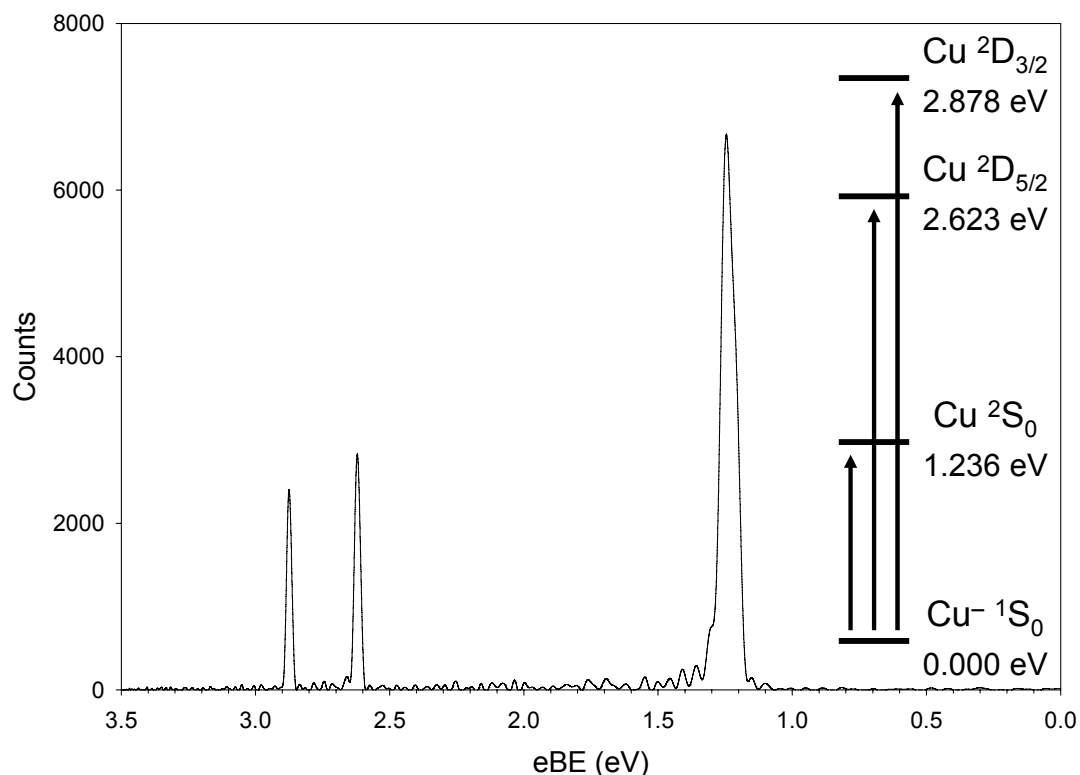
Figure 7.1 Atomic copper anion 355 nm photoelectron spectrum showing transitions from the anion ground state to the three lowest lying electronic states of atomic copper neutral. Transition energies and electronic term symbols are included for reference.

The 355 nm photoelectron imaging spectrum of $Cu^- H_2O$ is presented in Figure 7.2. The pattern of the electronic states accessed in this spectrum clearly follows the pattern seen in the copper anion photoelectron spectrum. The low binding energy feature is a transition to the $Cu(^2S_0) H_2O$ complex, while the higher binding energy features are transitions to the $Cu(^2D_{5/2}) H_2O$ and $Cu(^2D_{3/2}) H_2O$ complexes.
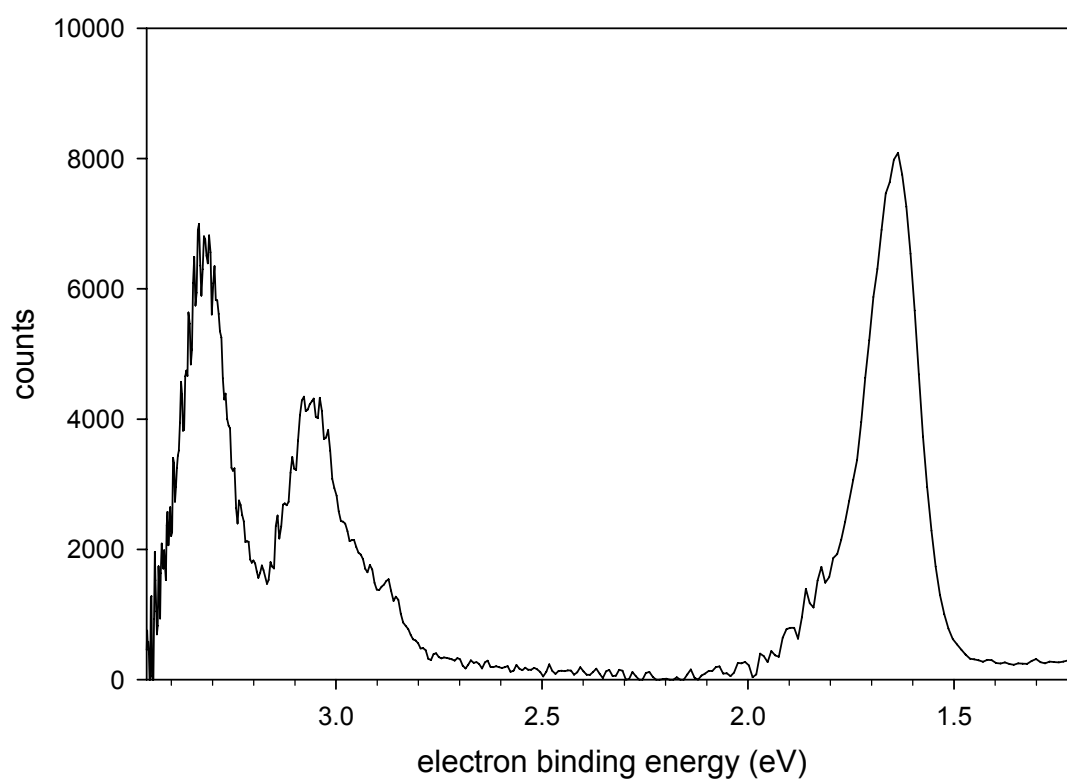
Figure 7.2 $Cu^- H_2O$ 355 nm photoelectron spectrum as reported in reference ## (^{2}).

Optimized geometries for the copper d4-methanol anion and neutral complexes have been calculated elsewhere,[5] and the structures are presented in Figure 7.3 along with symbolic radial Cu – O potential curves for the anion, neutral at anion geometry, and neutral lowest energy geometry. The calculated radial Cu – O well depth for the copper d4-methanol

system at the anion geometry of 650 cm^{-1} is about twice as deep as the analogous calculated[4] copper water well depth of 300 cm^{-1}. One aim of the photoelectron imaging spectra of Cu$^-$CD$_3$OD reported here is to determine if the photoelectron spectrum simulated using the calculated well depth compares favorably with the measured photoelectron imaging spectrum.
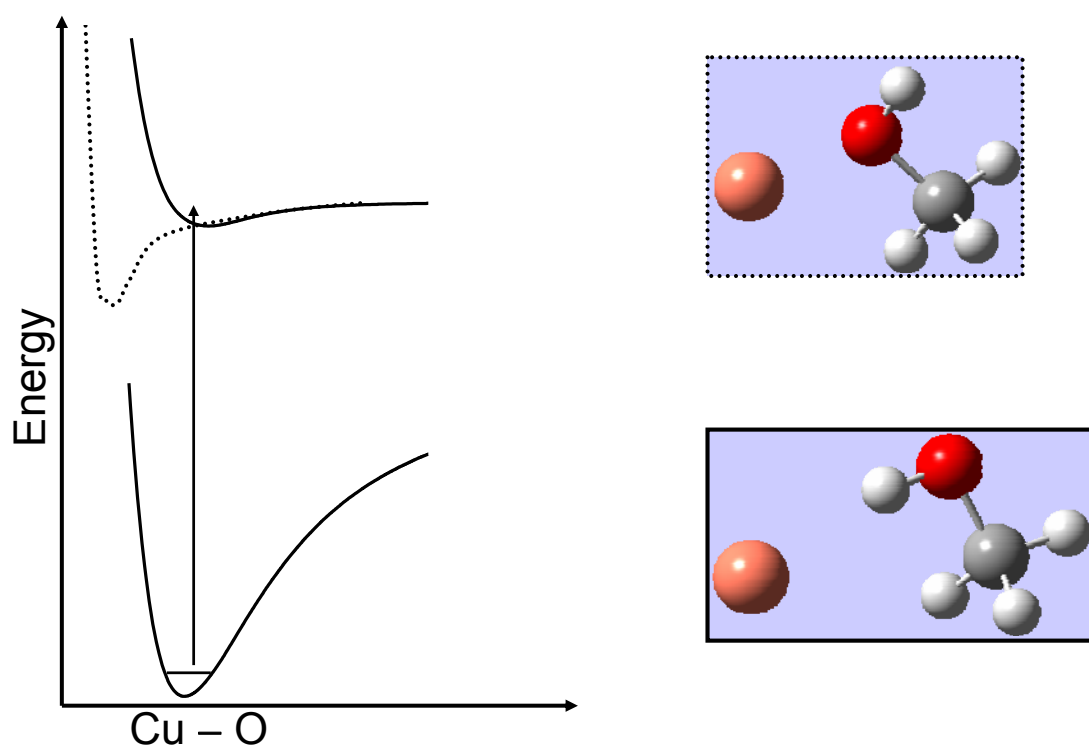
Figure 7.3 Calculated anion (lower) and neutral (upper) structures for the copper d4-methanol complexes. Symbolic radial Cu – O potential curves for the anion (lower solid curve), neutral at anion geometry (upper solid curve), and neutral lowest energy geometry (upper dotted curve) are also presented. The arrow shows the vertical photoelectron transition to the neutral ground electronic state surface.

The CuCD$_3$O$^-$ complex was studied, and its spectra included here, for several reasons. The first is that the mass of ^{65}CuCD$_3$O$^-$ is very close in mass to that of

[63]Cu[-]CD$_3$OD, thus initially the spectrum was taken to insure that there was no spectral contamination of [63]Cu[-]CD$_3$OD by [65]CuCD$_3$O[-]. Once the spectra were taken, however, there appeared to be a very similar vibrational progression in the excited ^{2}D$_{5/2}$ portion of the 355 nm spectra of both complexes. A very similar vibrational progression was also observed in transitions to the ground state of CuCD$_3$O[-]. Since the only difference between the two complexes is that of the OD proton, it is assumed that the very similar vibrational progressions observed in the spectra arise from the same excited vibrational mode. Further more, it is much easier to simulate the spectra for ground electronic to ground electronic state transitions that to or from excited electronic state transitions. Therefore, simulation of the CuCD$_3$O[-] ground state portion of the photoelectron spectrum using the methods described in chapter 2 should elucidate the nature of the vibrational features in both spectra.

The photoelectron spectrum of a similar system, CuOH[-], was measured by Misaizu[6]. Due to poor mass resolution, this photoelectron spectrum contains photodetachment features from both CuOH[-] and Cu[-]H$_2$O. The Cu[-]H$_2$O features were identified in our previous[2] Cu[-]H$_2$O study, thus the CuOH[-] features can also be identified. These features include peaks with unresolved structure at 0.98 eV eBE, 2.97 eV eBE, 3.25 eV eBE, and 3.43 eV eBE. The feature at 0.98 eV eBE is assigned as the transition to ground state CuOH, while the features at 3.25 eV eBE and 3.43 eV eBE are assigned as transitions to the well known[7] low lying singlet excited states of CuOH. The feature at 2.97 eV eBE is unassigned, but may be a transition to an unobserved or calculated low lying triplet excited state. [Note: This feature was assigned to Cu[-]H$_2$O photodetachment by Misaizu. Photodetachment near 2.7 eV eBE may be attributed to CuOH[-] photodetachment.] The electronic structure of CuCD$_3$O is assumed to be very similar to that of CuOH, and thus the electronic structure of CuCD$_3$O is compared to that of CuOH in the discussion section.

7.2   Experimental Methods

The photoelectron images were obtained using the photoelectron imaging spectrometer described in chapter 2. Completely deuterated methanol (CD_3OD) was introduced into the dc sputter discharge source by passing argon over a liquid sample (Aldrich, 97%) of neat d4-methanol. An ion signal of several hundred mV was measured from the inline MCP ion detector for both $^{65}Cu^-CD_3OD$ and $^{63}CuCD_3O^-$ anions. The time-of-flight mass spectrum labeled with anions of interest is presented in Figure 7.4. Spectra of the copper hydrides, $CuH(D)^-$ and $CuH_2(D_2)^-$, and analysis are presented in chapter 6.
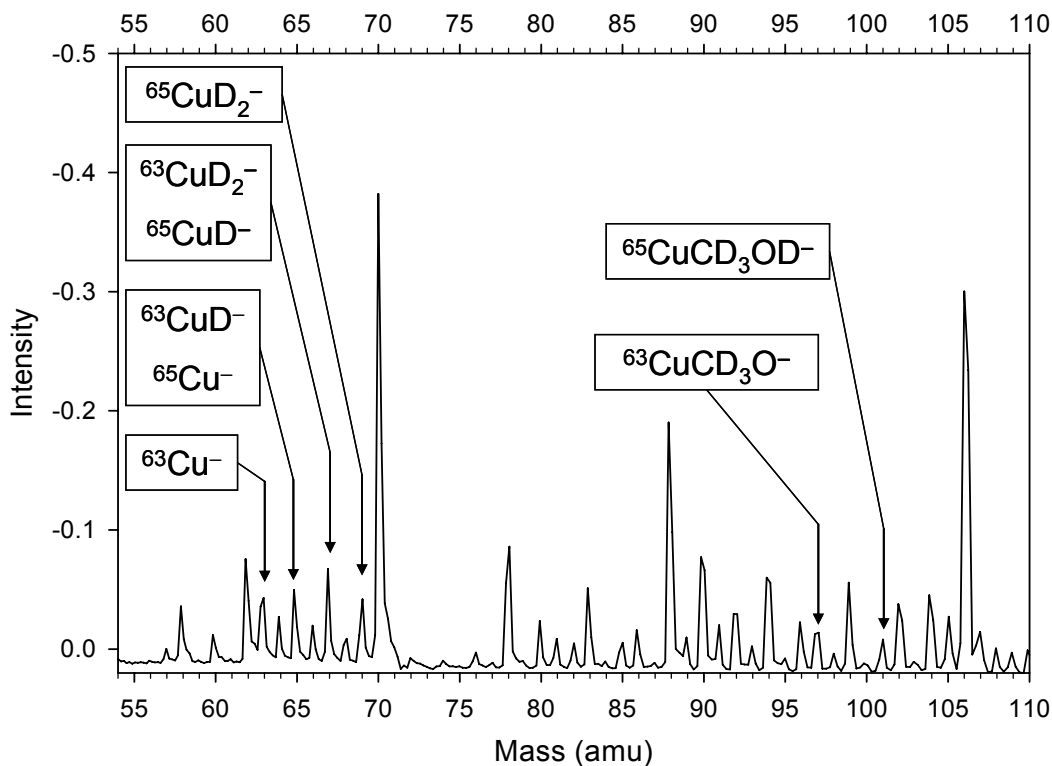
Figure 7.4   Time-of-flight mass spectrum obtained with the dc sputter ion source with relevant species labeled. Photoelectron imaging spectra of the copper hydrides are presented in chapter 6.

The tripled light (355 nm) from the Infinity laser system was used to take survey scans of the Cu^-CD_3OD and $CuCD_3O^-$ photoelectron spectra by setting the electron imaging optics such that 3.5 eV photoelectrons filled the detector area. The laser power used at 355 nm was $1 - 2$ mJ per pulse at a repetition rate of 50 Hz. In order to better resolve the low electron binding energy portions of the photoelectron imaging spectra of Cu^-CD_3OD and $CuCD_3O^-$, images were taken using the 600 nm (for Cu^-CD_3OD) and 500 nm (for $CuCD_3O^-$) laser pulses at 50 Hz produced by the Infinity OPO laser system. Typical pulse energies used were around 1 mJ. In these experiments the electron imaging optics were set such that 2.5 eV (500 nm) and 2.0 eV (600 nm) photoelectrons filled the detector. The photoelectron images presented here were averaged over $50,000 - 100,000$ laser shots. For images taken at 355 nm, observation of transitions to the three lowest lying electronic states[8] of copper neutral were used to calibrate the electron energy scale and to find the optimum electron imaging optics values at each magnification. Images taken at 500 nm and 600 nm were calibrated and focused using the transition to the ground state of copper neutral.

7.3   Results

The 355 nm raw photoelectron image, BASEX reconstructed photoelectron image, and photoelectron spectrum of Cu^-CD_3OD are presented in Figure 7.5. The images are of sufficient quality that some qualitative information may be extracted from them. Examination of the BASEX reconstructed photoelectron image (top right panel, Figure 7.5) clearly shows a high electron velocity feature (outer ring) and an extended progression at low electron velocity (inner features). Additionally, the lowest velocity feature has a much different angular distribution (nearly isotropic) when compared with the angular distribution of the other features (aligned with the electric field of the laser, which is vertical in the image). In contrast to the 355 nm Cu^-H_2O photoelectron imaging spectrum presented in

Figure 7.2 above, there is a clear vibrational progression in the reconstructed photoelectron image a low electron kinetic energies.

Examination of the photoelectron spectrum in Figure 7.5 shows the photoelectron spectrum to be similar to that of the $Cu^- H_2O$ 355 nm spectrum. Both spectra contain a sharp feature at low binding energy which is assigned as the vertical detachment energy (VDE) of the complexes (peak a) which arise from transitions to the neutral complex at the anion geometry. Both also include broad features at higher electron binding energies which correlate to the excited ^2D states of copper atom. There are several main differences, however. One is the partially resolved 519 (15) cm^{-1} vibrational progression (peaks d – g) in the $Cu^- CD_3OD$ spectrum. While there is significant broadening in the high electron binding energy region of the 355 nm $Cu^- H_2O$ spectrum, there are no resolved vibrational progressions. Peaks b and c are assigned as a hot band progression with a vibrational frequency of 770 cm^{-1}. A second difference is that the relative intensity of the features near 2.9 eV electron binding (peaks d – h) is much greater than the relative intensity of the VDE peak in $Cu^- CD_3OD$, while the relative intensities of these features in $Cu^- H_2O$ are comparable.

Figure 7.5   CuCD$_3$OD$^-$ 355 nm full scale raw photoelectron image (top left), BASEX reconstructed photoelectron image (top left), and photoelectron spectrum (bottom).

A third major difference is the value of the angular anisotropy parameter for the features in the spectra. For $Cu^- H_2O$, $\beta = 2$ for the VDE peak, suggesting detachment from an unperturbed copper 4s orbital, and $\beta \approx 0.2$ for both high electron binding energy features, suggesting that these electrons are photodetached from copper 3d orbitals. For $Cu^- CD_3OD$ the case is slightly different. The VDE peak has an angular anisotropy parameter of $\beta = 1.8$, which suggest that the anion orbital is not a pure copper 4s orbital, but rather has some small contribution from an orbital of different character. The higher binding energy features containing the vibrational progression (peaks d – h) have angular anisotropy parameters around $\beta = 1.4$, suggesting that the anion orbital from which these electrons are detached is very different than the corresponding orbital (nearly pure Cu 3d) in $Cu^- H_2O$. Furthermore, the highest binding energy feature in the 355 nm $Cu^- CD_3OD$ photoelectron spectrum (peak i) has an angular anisotropy parameter of $\beta = 0.6$, suggesting that these electrons originate from an anion orbital much more similar in character to an atomic copper 3d orbital.

It is possible, now, to assign peak d as the vibrational origin of the $Cu(^2D_{5/2})CD_3OD$ electronic state as 2.877 (4) eV, and assign peak i as the vertical detachment energy for the $Cu(^2D_{3/2})CD_3OD$ state as 3.297 (15) eV. When combined with the electron affinity estimated below, the electronic term energies for these states are 1.422 (30) eV [11,470 (242) cm^{-1}] for the $^2D_{5/2}$ state and 1.842 (30) eV [14,857 (242) cm^{-1}] for the $^2D_{3/2}$ state. The large uncertainty in these values is due to the uncertainty in the calculated difference between the VDE and the EA for $Cu^- CD_3OD$.

The $Cu^- CD_3OD$ 600 nm raw photoelectron image, BASEX reconstructed photoelectron image, and photoelectron spectrum are presented in Figure 7.6, along with the spectral simulation mentioned in the introduction. A cursory look at the images immediately shows that there is negligible vibrational structure, i.e. a single peak. The spectrum shows this as well, but it also shows that there is some asymmetry in the peak shape, and some

subtle shoulders on the low electron binding energy side of the peak. The shoulders, or ripples, on the high electron binding energy side of the peak are clearly due to the periodic center line noise caused by the image reconstruction. This noise is seen as a vertical line of dots in the reconstructed image, but is most intense on the inside (high binding energy) of the main image feature, and much less intense to the outside (low binding energy) of the feature. The simulation beautifully reproduces the peak asymmetry and the low electron binding energy shoulders, confirming that the photodetachment signal carrier is the $Cu^- CD_3OD$ anion complex in the geometry presented in Figure 7.3. The vertical detachment energy is assigned as 1.642 (6) eV. The calculations predict that the difference in energy between the VDE and the electron affinity approximately 0.187 eV, which sets the electron affinity of $CuCD_3OD$ as 1.455 (30) eV. As stated above, the error in the EA is largely due to the uncertainty of the calculation.
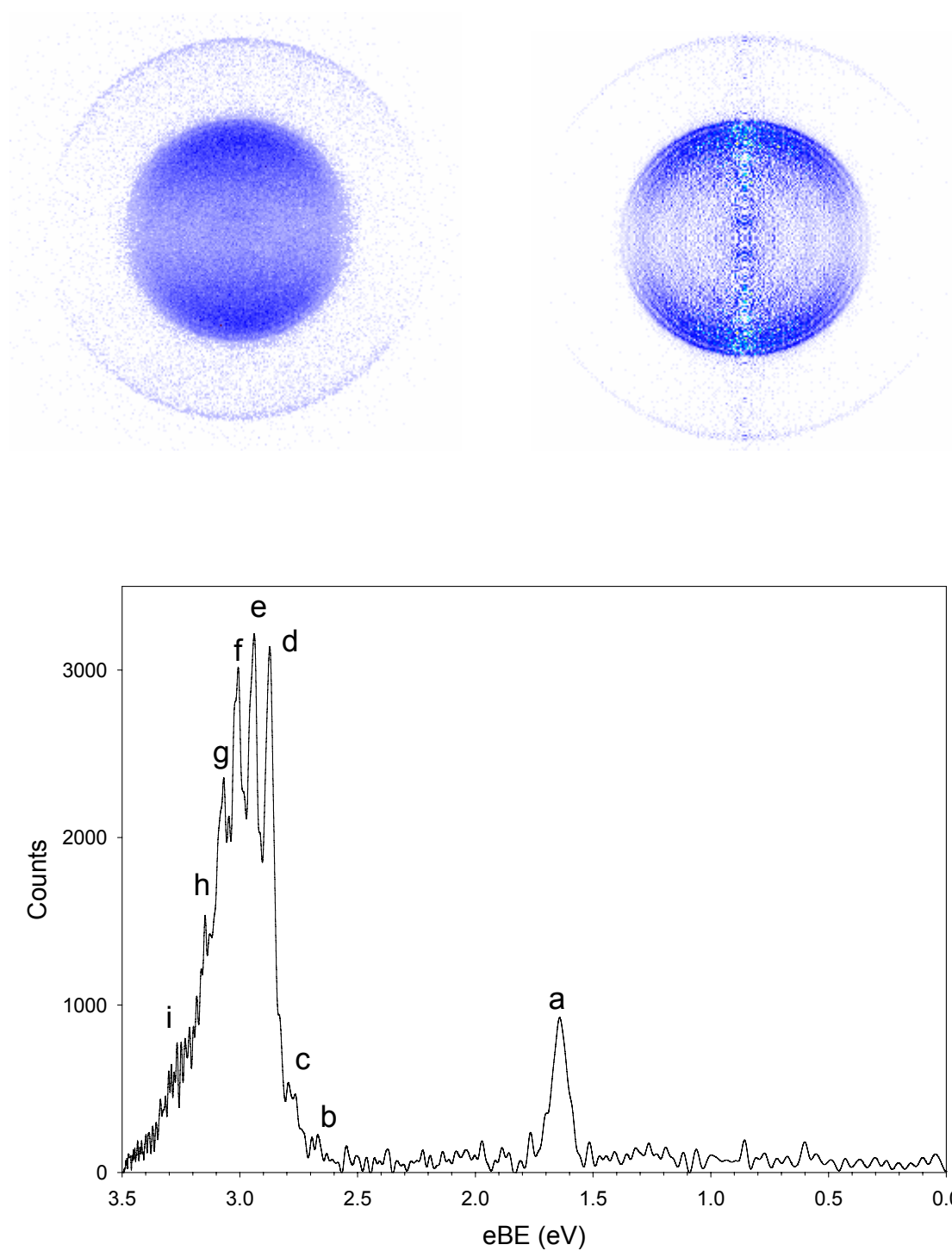
Figure 7.6 CuCD$_3$OD$^-$ 600 nm raw photoelectron image (top left), BASEX reconstructed photoelectron image (top right), and photoelectron spectrum (bottom). The points in the spectrum are the experimental data and the solid line is a simulation as explained in the text.

The CuCD$_3$O$^-$ 355 nm raw photoelectron image, BASEX reconstructed image, and photoelectron spectrum are presented in Figure 7.7. The images are very similar to those of Cu$^-$CD$_3$OD taken at 355 nm. Like the Cu$^-$CD$_3$OD images, the CuCD$_3$O$^-$ images contain a high electron velocity feature as well as several complicated low electron velocity features.

In contrast to the Cu^-CD_3OD images, however, the $CuCD_3O^-$ images contain three distinct features at low electron kinetic energy. The image reconstruction clearly shows that the lowest and highest electron velocity features of these three have extended vibrational progressions as well as angular anisotropies aligned with the electric field of the laser (vertical in the images). In contrast, the middle feature appears to have no vibrational structure and little to no angular anisotropy.

The 355 nm photoelectron spectrum shows some unresolved vibrational features in the low electron binding region, labeled "a" in Figure 7.7. These features are resolved in the 500 nm photoelectron spectrum presented in Figure 7.8 and discussed below. The high electron binding energy portion of the spectrum clearly shows what appear to be three electronic states. The angular anisotropy parameters for these features support this as $\beta \approx 1.2$ for peaks b – d, $\beta = 0.3$ for peak e, and $\beta \approx 1$ for peaks f – h. The angular anisotropy parameters clearly show that these three low electron binding energy features are produced by removal of electrons from different orbitals in the anion, thus producing different electronic states of the neutral.

Peak b is assigned as the vibrational origin of the first excited state of $CuCD_3O$ with an electron binding energy of 2.778 (5) eV. When combined with the electron affinity of $CuCD_3O$ (reported below) the electronic term energy of this state is measured to be 1.701 (2) eV, or 13,720 (16) cm^{-1}. A vibrational progression (peaks b – d) of 520 (50) cm^{-1} is also seen in the transitions to this electronic state. Peak e is assigned as the second excited electronic state of $CuCD_3O^-$ with an electron binding energy of 3.133 (6) eV and an electronic term energy of 2.056 (4) eV, or 16,583 (32) cm^{-1}. Peak f is assigned as the vibrational origin of the third excited electronic state of $CuCD_3O$ with an electron binding energy of 3.271 (6) eV and an electronic term energy of 2.194 (4) eV or 17,696 (32) cm^{-1}. This electronic state also has a vibrational progression (peaks f – h) of 335 (60) cm^{-1}.
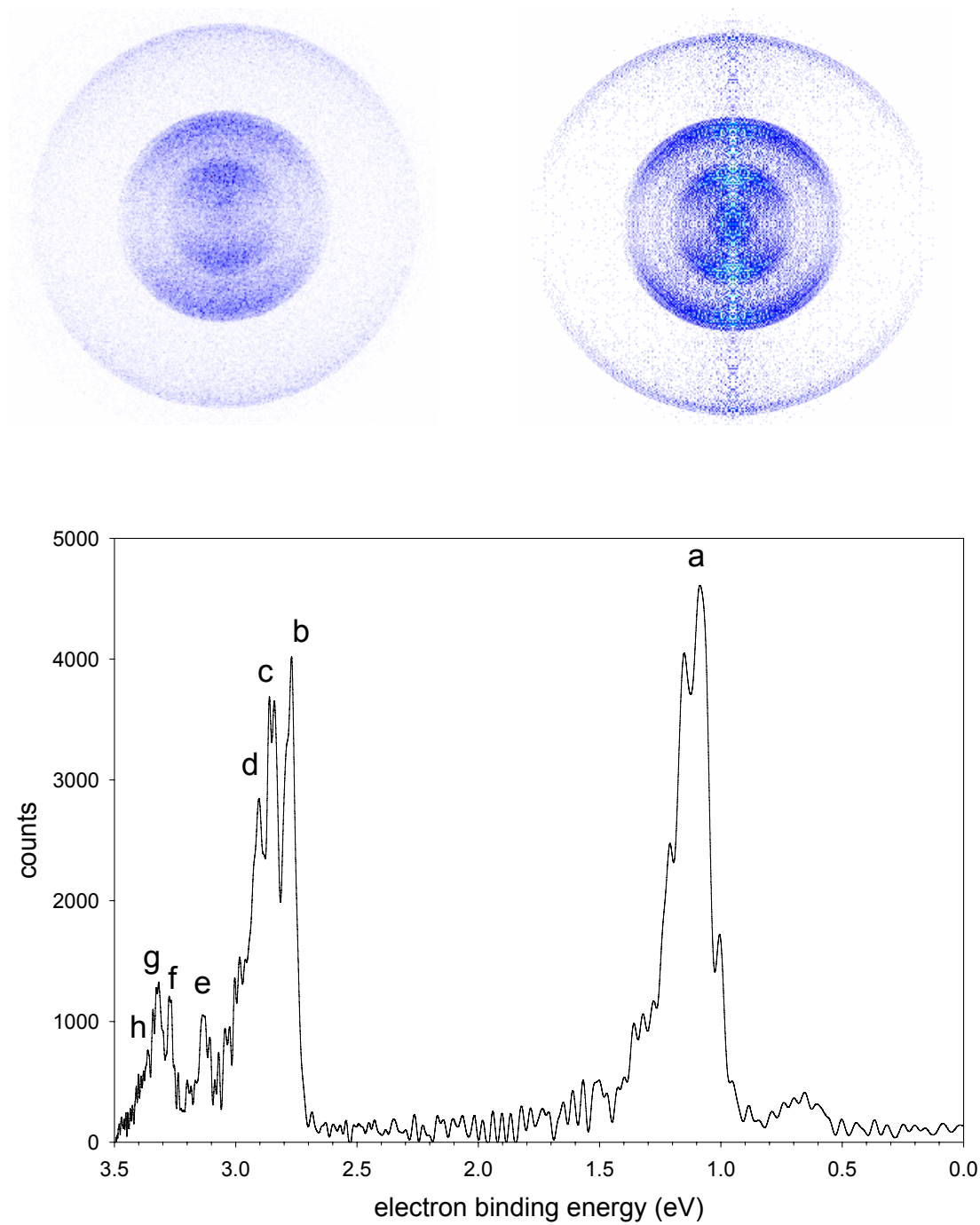
Figure 7.7 CuCD$_3$O$^-$ 355 nm raw photoelectron image (top left), BASEX reconstructed photoelectron image (top right), and photoelectron spectrum (bottom).

The CuCD$_3$O$^-$ 500 nm raw photoelectron image, BASEX reconstructed image, and photoelectron spectrum are presented in Figure 7.8. At this photodetachment wavelength the resolution of the ground state features labeled "a" in Figure 7.7 is much improved. The reconstructed image shows clear vibrational structure in the outmost (high electron velocity) portion of the image. The angular anisotropy of the image is again aligned with the electric field of the laser pulse, which is vertical in the images. In addition, both the raw image and reconstruction show significant detachment at the very center of the image, which corresponds to near zero kinetic energy electrons. The images clearly show electron detachment up to the energy of the photodetachment laser pulse. The photoelectron spectrum has a very clear and short vibrational progression (peaks a – d) of 528 (50) cm^{-1}. The origin of this vibrational progression is peak "a" and is assigned as the electron affinity of CuCD$_3$O with a value of 1.077 (4) eV. The angular anisotropy values for peaks a – d are very near β ≈ 1.2, confirming the assignment that these transitions are to and from the same electronic state.
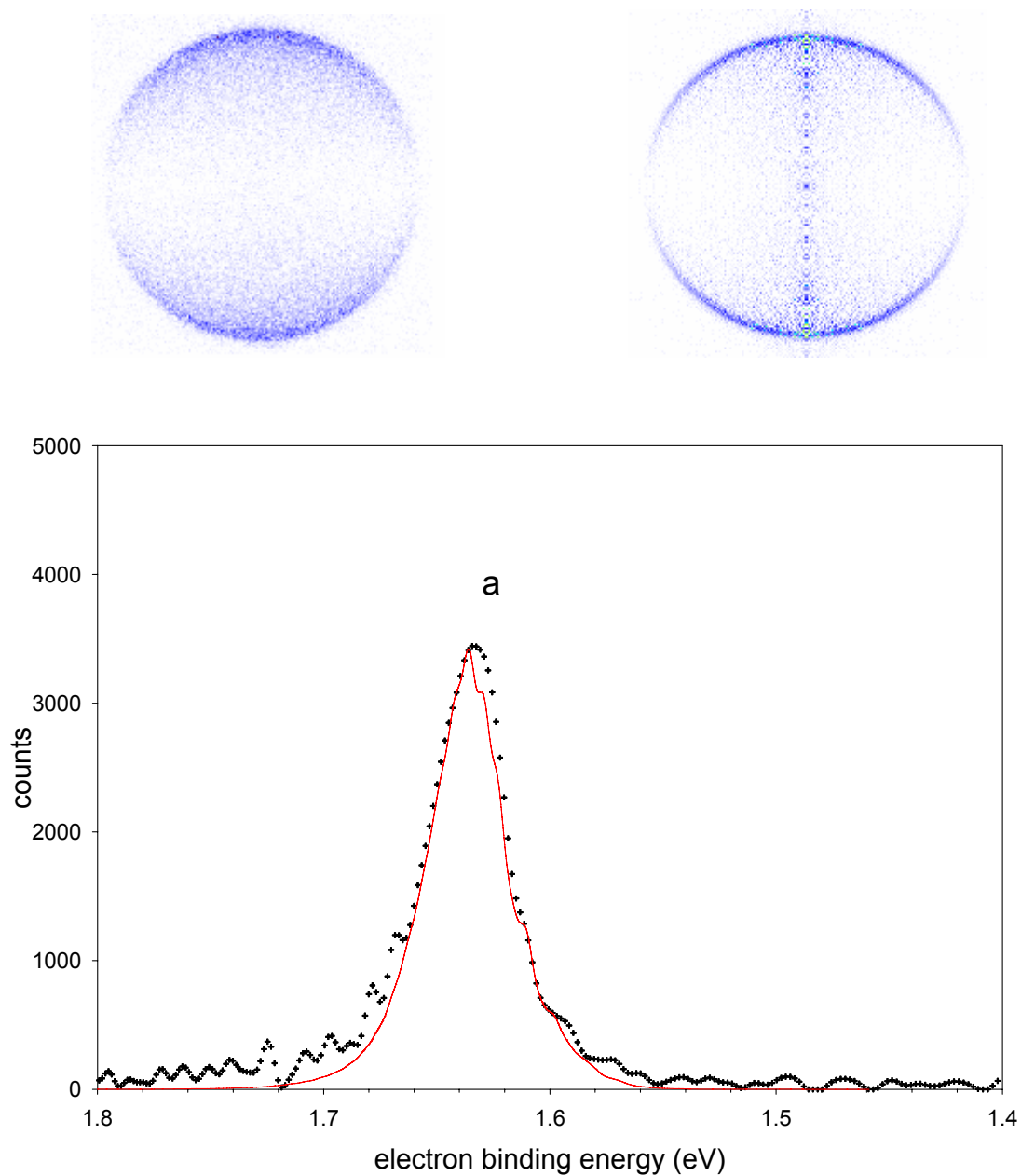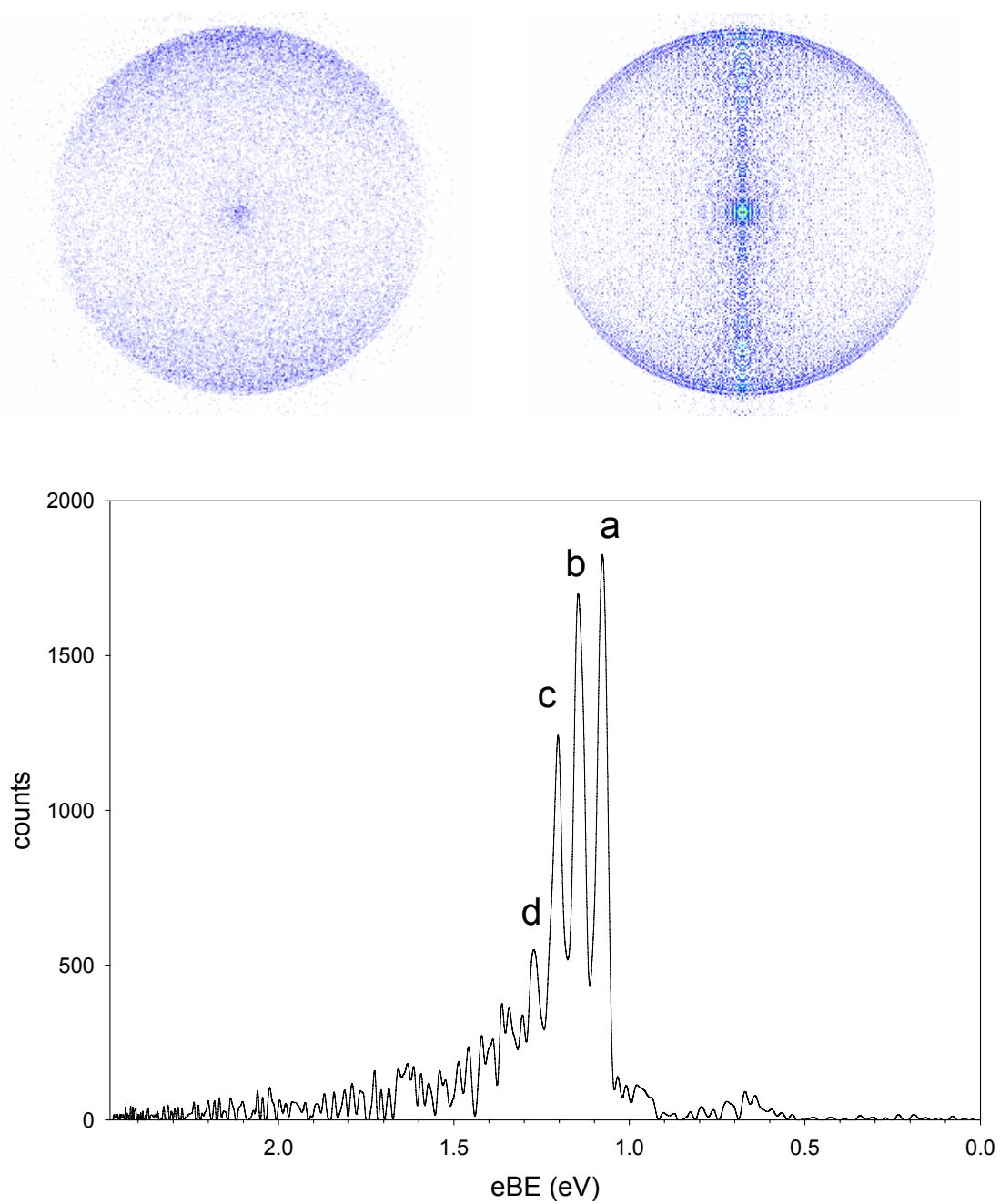
Figure 7.8 CuCD$_3$O$^-$ 500 nm raw photoelectron image (top left), BASEX reconstructed photoelectron image (top right), and photoelectron spectrum (bottom).

7.4   Discussion

As mentioned in the introduction, the electronic structure of the neutrals created upon photodetachment of the copper ligand complexes studied here essentially follows the atomic copper netural electronic structure (see Figure 7.1). Table 7.1 compares the electron affinities and electronic term energies for the first two electronic excited states, corresponding to $Cu(^2D_{5/2,\ 3/2})$, of Cu, CuH_2O, and $CuCD_3OD$. Immediately noticeable from Table 7.1 is that the addition of both water and methanol to copper anion increases the neutral electron affinity by ~ 230 meV. The binding energies for the first excited state (correlating to $^2D_{5/2}$ in copper neutral) of the complexes, however, are all increased by the addition of the different ligands. The "$^2D_{5/2}$" electron binding energies for $CuCD_3OD$ and CuH_2O differ by $200 - 300$ meV. It is possible that this is due to this value being the vertical detachment energy (VDE) in the case of CuH_2O, as the origin is certainly lower in energy. This strongly suggests that the $Cu(^2D_{5/2})H_2O$ origin is the shoulder feature at 2.85 eV electron binding energy in Figure 7.2. In the case of the "$^2D_{3/2}$" state features, the features in the Cu^-H_2O and Cu^-CD_3OD spectra have no obvious origin and are thus reported as vertical detachment energies.

Table 7.1   Measured electron affinities and anion electron binding energies for photodetachment of Cu^-, Cu^-H_2O, and Cu^-CD_3OD to the neutral states which correlate to the $^2D_{5/2}$ and $^2D_{3/2}$ electronic states of copper atom.

species	electron affinity (eV)	$^2D_{5/2}$ eBE derived from Origin or VDE (eV)	$^2D_{3/2}$ eBE derived from Origin or VDE (eV)
Cu	1.236^a	2.623^a	2.878^a
CuH₂O	$1.480^{b,c}$	3.050 (VDE)^c	3.313 (VDE)^c
CuCD₃OD	1.455^b	2.877 (Origin)	3.297 (VDE)

^{a} From reference 7

^{b} Estimated from calculated difference between vertical detachment energy and electron affinity

^{c} From reference 2

As mentioned in the introduction, spectral simulation of the ground state portion of the $CuCD_3O^-$ photoelectron spectrum will allow an assignment of the ~ 520 cm^{-1} vibrational progression seen in the Cu^-CD_3OD and $CuCD_3O^-$ excited state portions of the photoelectron spectra. The simulation was conducted as described in chapter 2, using the B3LYP method with the aug-cc-pvtz basis set for carbon, oxygen, and hydrogen, and the $(7s,7p,6d,3f)$ basis set of Wang and coworkers[9] for copper. The vibrational mode excited in the simulation is a $\sim$ 720 cm^{-1} methyl rock motion which contracts the O – C – H bond angle. No other motions had any appreciable excitation in the simulation, thus the ~ 520 cm^{-1} vibrational progression observed in the photoelectron spectra of Cu^-CD_3OD and $CuCD_3O^-$ are assigned to this motion. The same vibrational excitation is assigned in the photoelectron spectrum of CH_3O^- recorded by Ramond and coworkers.[10]

The electronic structure of $CuCD_3O$ is very different from the electronic structure of CuH_2O and $CuCD_3OD$. Both water and methanol are closed shell polar molecules, thus the complexes are best described as having dipole-induced dipole interactions. In $CuCD_3O$ a

bonding interaction occurs between the copper 4s electron and the oxygen 2p electron, thus the $CuCD_3O$ electronic structure is compared to that of CuOH. Table 7.2 presents the measured electron affinities and low-lying electronic state term energies for CuOH and $CuCD_3O$. As mentioned in the introduction, the photoelectron spectrum of $CuOH^-$ and Cu^-H_2O measured by Misaizu may have been assigned incorrectly. The electron affinities of the two species differ by less than 10 meV, and the 2nd and 3rd excited electronic state term energies are very similar as well. However, the first excited state of CuOH may be overlapped by the excited states of CuH_2O in the Misaizu spectrum. If there is a low-lying CuOH excited state it is most likely a triplet state, as the observed electronic transitions[11,12] were observed between the singlet ground state and excited singlet states. The low-lying singlet states have also been calculated recently,[13] but no calculations of the low-lying triplet states have been reported. A high mass and high energy resolution photoelectron spectrum of $CuOH^-$ would certainly detect the presence or absence of a low-lying triplet state, and such an experiment is certainly possible using the photoelectron imaging apparatus described here.

Table 7.2 Measured anion electron binding energies for detachment to the three lowest lying neutral electronic states of CuOH and $CuCD_3O$.

species	electron affinity (eV)	1st excited state T_e (eV)	2nd excited state T_e (eV)	3rd excited state T_e (eV)
CuOH	0.98 [a]	see note [b]	1.973 [c]	2.282 [d]
$CuCD_3O$ [e]	1.077 (4)	1.701 (2)	2.056 (4)	2.194 (4)

[a] From reference 5

[b] Assumed to be unreported and uncalculated low lying triplet excited state of CuOH, see text

[c] From reference 11

[d] From reference 10

[e] This work

References for Chapter VII

[1] F. Muntean, M. S. Taylor, A. B. McCoy, and W. C. Lineberger, *The Journal of Chemical Physics* **121**, 5676 (2004).

[2] G. J. Rathbone, T. Sanford, D. Andrews, and W. C. Lineberger, *Chemical Physics Letters* **401** (4-6), 570 (2005).

[3] M. S. Taylor, J. Barbera, C.-P. Shulz, F. Muntean, A. B. McCoy, and W. C. Lineberger, *The Journal of Chemical Physics* **122**, 05431 (2005).

[4] M. S. Taylor, F. Muntean, W. C. Lineberger, and A. B. McCoy, *The Journal of Chemical Physics* **121**, 5688 (2004).

[5] J. Barbera, S. Horvath, V. Dribinski, A. B. McCoy, and W. C. Lineberger, (In Preparation).

[6] F. Misaizu, K. Tsukamoto, M. Sanekata, and K. Fuke, *Surface Review and Letters* **3** (1), 405 (1996).

[7] NIST, *NIST Chemistry Webbook, NIST Standard Reference Database Number 69, June 2005 Release.*

[8] J. Sugar and A. Musgrove, *Journal of Physical and Chemical Reference Data* **19**, 527 (1990).

[9] X.-B. Wang, L.-S. Wang, R. Brown, P. Schwerdtfeger, D. Schroder, and H. Schwarz, *The Journal of Chemical Physics* **114** (17), 7388 (2001).

[10] T. M. Ramond, G. E. Davico, R. L. Schwartz, and W. C. Lineberger, *The Journal of Chemical Physics* **112** (3), 1158 (2000).

[11] C. N. Jarman, W. T. M. L. Fernando, and P. F. Bernath, *Journal of Molecular Spectroscopy* **144** (2), 286 (1990).

[12] C. N. Jarman, W. T. M. L. Fernando, and P. F. Bernath, *Journal of Molecular Spectroscopy* **145**, 151 (1991).

[13] S. Wang, A. Paul, N. J. DeYonder, Y. Yamaguchi, and H. F. Shaefer, *The Journal of Chemical Physics* **123**, 014313 (2005).

_____

Conclusions

_____

This thesis presented the results of anion photoelectron spectroscopy experiments conducted on three classes of anions. One class is that of heteronuclear coinage metal diatomic molecules. These include AgO^-, AuO^-, AuS^-, CuH^-, and CuD^-. The photoelectron spectra of these molecules are characterized by short vibrational progressions in transitions to the ground electronic states and confident assignments of the electronic state origins and electron affinities. The photoelectron spectra of these molecules measured for the first time the electron affinities of the corresponding neutral molecules. Frank-Condon simulation of the observed ground state vibrational structure coupled with observation of a well characterized excited state allowed for the assignment of the anion equilibrium bond lengths for AgO^-, CuH^-, and CuD^-. Because no excited electronic states were observed in the photoelectron spectra of AuO^- and AuS^-, only the magnitude of the bond length change between the anion and the neutral molecules was assigned. Observation of hot-bands in the photoelectron spectra allowed for the first assignment of anion harmonic vibrational frequencies for AgO^- and AuS^-. In addition, a predicted, yet previously unobserved, $^3\Sigma^+$ excited electronic state of CuD and CuH was observed in the photoelectron spectra of CuD^- and CuH^-.

The second class of molecules studied was that of copper anion complexes. These included $Cu^- CD_3OD$, $CuCD_3O^-$, CuH_2^-, and CuD_2^-. The photoelectron spectra of these complexes are characterized by extended vibrational progressions in transitions to nearly all the electronic states observed. These extended vibrational progressions are the product of

large geometry changes between the anion and neutral complexes. In the case of Cu^-CD_3OD, the geometry change is so significant that ground electronic state photodetachment is only observed which produces a higher energy, yet stable, conformer of $CuCD_3OD$. Thus, only the vertical detachment energy was experimentally determined, with the adiabatic electron affinity assigned on the basis of a high level spectral simulation. The geometry change for transitions to the excited states electronic states of $CuCD_3OD$ is less severe, which allowed for the assignment of the excited electronic state origins. The geometry difference between the anion and neutral $CuCD_3O$ is also small enough such that all the electronic state origins in the photoelectron spectrum were assigned. A vibrational mode excited in the ground electronic state of $CuCD_3O$, and in the excited states of $CuCD_3O$ and $CuCD_3OD$ was identified. It was found to be very similar to a vibrational mode excited in the photoelectron spectrum of CH_3O^-.

The geometry change between the anion and neutral of CuH_2 and CuD_2 is also very severe, as the anions are linear and the neutrals are very bent (bond angle of $\sim 122°$). However, the geometry change is so great in the bending coordinate that the vibrational overlap of this mode between the anion and neutral in the energy region studied produced very weak features in the photoelectron spectrum. The spectra, then, are dominated by a short vibrational progression in the symmetric stretch mode which allows determination of the electron affinities of CuH_2 and CuD_2.

The photoelectron spectra of two related organic compounds were also taken. Photoelectron spectra of the 1,2,3-triazolide anion were recorded and show signatures of strong vibronic coupling of the low lying electronic states of the neutral. Still, the vibrational origin of transitions to the ground electronic state of the neutral allowed for easy assignment of the neutral electron affinity. Combination of the measured electron affinity with the gas phase acidity measured elsewhere allowed for determination of the N-H bond dissociation

energy of the parent molecule 1H-1,2,3-triazolide. In addition, the heat of formation of the 1,2,3-trizolyl radical was also determined. It was also found that, under the experimental source conditions used in these experiments, about 40% of the 1,2,3-triazolide anions ring open to form the E-iminodiazomethide anion, the structure of which was assigned on the basis of a simulation of the measured photoelectron spectrum. The simulation also allowed assignment of several normal mode frequencies of the anion and neutral. It is interesting to note that the lower azole anions (pyrolide, pyrazolide, and imidazolide) were found not to ring-open under similar experimental conditions.

Bibliography

_____

T. Andersen, H.K. Haugen, and H. Hotop, *Binding energies in atomic negative ions: III.* Journal of Physical and Chemical Reference Data, 1999. **28**(6): p. 1511-1533.

D.H. Andrews, A.J. Gianola, and W.C. Lineberger, *On the photoelectron spectrum of AgO⁻.* Journal of Chemical Physics, 2002. **117**(8): p. 4074 - 4076.

D.H. Andrews, T. Ichino, R.M.D. Calvi, A.J. Gianola, S. Kato, G.J. Rathbone, F. Misaizu, V.M. Bierbaum, and W.C. Lineberger, *Photoelectron Spectroscopy of 1,2,3-Triazolide Isomers and Gas Phase Acity Bracketing of 2H-1,2,3-Triazole.* 2006(In Preparation).

L. Andrews and X. Wang, *Infrared Spectra and Structures of the Stable CuH₂⁻, AgH₂⁻, AuH₂⁻, and AuH₄⁻ Anions and the AuH₂ Molecule.* Journal of the American Chemical Society, 2003. **125**(38): p. 11751-11760.

J. Andzelm, E. Radzio, and D.R. Salahub, *Model Potential Calculations For 2nd-Row Transition-Metal Molecules Within the Local-Spin-Density Method.* Journal of Chemical Physics, 1985. **83**(9): p. 4573-4580.

A.M. Antic-Jovanovic and D.S. Pesic, *Emission spectra of copper(I) hydroxide and deuterated copper(I) hydroxide in the regions between 5100-5600 Ang. and 6150-6300 Ang.* Glasnik Hemijskog Drustva Beograd, 1969. **34**(2-4): p. 163-9.

M. Arai, T. Tsukahara, and M. Tamura, *Deflagration properties of triazoles and their compositions as candidates for new gas generating agent of the air bag system.* Proceedings of the International Pyrotechnics Seminar, 1999. **26th**: p. 7-14.

K. Babic-Samardzija and N. Hackerman, *Triazole, benzotriazole and substituted benzotriazoles as corrosion inhibitors of iron in aerated acidic media.* Journal of Solid State Electrochemistry, 2005. **9**(7): p. 483-497.

M.M. Balkis, S.D. Leidich, P.K. Mukherjee, and M.A. Ghannoum, *Mechanisms of fungal resistance - An overview.* Drugs, 2002. **62**(7): p. 1025-1040.

V. Barone and C. Adamo, *Validation of Hybrid Density Functional/Hartree-Fock Approaches for the Study of Homogeneous Catalysis.* Journal of Physical Chemistry, 1996. **100**(6): p. 2094-9.

V. Barone and C. Adamo, *First-row transition-metal hydrides: a challenging playground for new theoretical approaches.* International Journal of Quantum Chemistry, 1997. **61**(3): p. 443-451.

C.W. Bauschlicher, C.J. Nelin, and P.S. Bagus, *Transition-Metal Oxides - CrO, MoO, NiO, PdO, AgO.* Journal of Chemical Physics, 1985. **82**(7): p. 3265-3276.

C.W. Bauschlicher, H. Partridge, and S.R. Langhoff, *An Abinitio Study of the Low-Lying Doublet States of AgO and AgS.* Chemical Physics, 1990. **148**(1): p. 57-68.

P. Belohorec, S.M. Rothstein, and J. Vrbik, *Infinitesimal, differential, diffusion-quantum-Monte-Carlo study of copper hydride (CuH) spectroscopic constants.* Journal of Chemical Physics, 1993. **98**(8): p. 6401-5.

V.N. Belyaev, N.L. Lebedeva, K.S. Krasnov, and L.V. Gurvich, *Flame spectrophotometric determination of the dissociation energy of copper oxide and hydroxide.* Izvestiya Vysshikh Uchebnykh Zavedenii, Khimiya i Khimicheskaya Tekhnologiya, 1978. **21**(11): p. 1698-700.

P.F. Bernath, *Laser and Fourier transform spectroscopy: diatomics to organometallics.* AIP Conference Proceedings, 1986. **146**(Adv. Laser Sci. - 1): p. 443-6.

R.C. Bilodeau, M. Scheer, and H.K. Haugen, *Infrared laser photodetachment of transition metal negative ions: studies on Cr-, Mo-, Cu- and Ag.* Journal of Physics B-Atomic Molecular and Optical Physics, 1998. **31**(17): p. 3885-3891.

S.J. Blanksby and G.B. Ellison, *Bond dissociation energies of organic molecules.* Accounts of Chemical Research, 2003. **36**(4): p. 255-263.

C. Blondel, P. Cacciani, C. Delsart, and R. Trainham, *HIGH-RESOLUTION DETERMINATION OF THE ELECTRON-AFFINITY OF FLUORINE AND BROMINE USING CROSSED ION AND LASER BEAMS.* Physical Review A, 1989. **40**(7): p. 3698 - 3701.

J.C.A. Boeyens and R.H. Lemmer, *Valence bond studies. Part 2. Diatomic compounds of copper, silver and gold.* Journal of the Chemical Society, Faraday Transactions 2: Molecular and Chemical Physics, 1977. **73**(3): p. 321-6.

V. Bojovic, A. Antic-Jovanovic, M.M. Stoiljkovic, M. Miletic, and D.S. Pesic, *Vibrational structure of the B-X system of isotopic AgO molecules.* Spectroscopy Letters, 1999. **32**(5): p. 875-882.

G. Bravo-Perez and I.L. Garzon, *Ab initio study of small Au_nS, (n=1-5), and Au_nS_2, (n=1-4), clusters.* Theochem, 2002. **619**: p. 79-89.

C.M. Brown and M.L. Ginter, *The absorption spectrum of copper(I) hydride in the 2350- to 1890 angstrom region.* Journal of Molecular Spectroscopy, 1980. **80**(1): p. 145-57.

D. Buchel, C. Mihalcea, T. Fukaya, N. Atoda, J. Tominaga, T. Kikukawa, and H. Fuji, *Sputtered silver oxide layers for surface-enhanced Raman spectroscopy.* Applied Physics Letters, 2001. **79**(5): p. 620-622.

S.B. Bulgarevich, V.S. Bolotnikov, V.N. Sheinker, O.A. Osipov, and A.D. Garnovskii, *Structure and properties of heterocyclic compounds and their complexes. XIX. Vector additive system for calculating the dipole moments of azoles.* Zhurnal Obshchei Khimii, 1975. **45**(8): p. 1821-6.

R. Burtovyy, E. Utzig, and M. Tkacz, *Studies of the thermal decomposition of copper hydride.* Thermochimica Acta, 2000. **363**(1-2): p. 157-163.

R. Burtovyy, D. Wlosewicz, A. Czopnik, and M. Tkacz, *Heat capacity of copper hydride.* Thermochimica Acta, 2003. **400**(1-2): p. 121-129.

K. Cashion, *Calculating vibrational transition probabilities.* Journal of Molecular Spectroscopy, 1963. **10**: p. 182-231.

J. Catalán, R.M. Claramunt, J. Elguero, J. Laynez, M. Menéndez, F. Anvia, J.H. Quian, M. Taagepera, and R.W. Taft, *Basicity and Acidity of Azoles: The Annelation Effect in Azoles.* J. Am. Chem. Soc., 1988. **110**(13): p. 4105-4111.

Z.X. Chen and H.M. Xiao, *Theoretical study on tetrazole and its derivatives: 4. Ab initio study on hydroxyl derivatives of tetrazole.* Propellants Explosives Pyrotechnics, 1999. **24**(5): p. 319-324.

C.L. Collins, K.G. Dyall, and H.F. Schaefer, III, *Relativistic and correlation effects in CuH, AgH, and AuH: comparison of various relativistic methods.* Journal of Chemical Physics, 1995. **102**(5): p. 2024-31.

J. Cooper and R.N. Zare, *Angular distribution of photoelectrons.* Journal of Chemical Physics, 1968. **48**: p. 942-943.

G. Das, *A pseudopotential study of the iron-series transition metal hydrides.* Journal of Chemical Physics, 1981. **74**(10): p. 5766-74.

Y. Ding, S.A. Hofstadler, E.E. Swayze, L. Risen, and R.H. Griffey, *Design and synthesis of paromomycin-related heterocycle-substituted amino-glycoside mimetics based on a mass spectrometry RNA-binding assay.* Angewandte Chemie, International Edition, 2003. **42**(29): p. 3409-3412.

V. Dribinski, A. Ossadtchi, V.A. Mandelshtam, and H. Reisler, *Reconstruction of Abel-transformable images: The Gaussian basis-set expansion Abel transform method.* Review of Scientific Instruments, 2002. **73**(7): p. 2634 - 2642.

M. Ebben, G. Meijer, and J.J. Ter Meulen, *Laser evaporation as a source of small free radicals.* Applied Physics B: Photophysics and Laser Chemistry, 1990. **B50**(1): p. 35-8.

A.A. El-Azhary, H.U. Suter, and J. Kubelka, *Experimental and Theoretical Investigation of the Geometry and Vibrational Frequencies of 1,2,3-Triazole, 1,2,4-Triazole, and Tetrazole Anions.* Journal of Physical Chemistry A, 1998. **102**(3): p. 620-629.

A.T.J.B. Eppink and D.H. Parker, *Velocity map imaging of ions and electrons using electrostatic lenses: Application in photoelectron and photofragment ion imaging of molecular oxygen.* Review of Scientific Instruments, 1997. **68**(9): p. 3477 - 3484.

K.M. Ervin, J. Ho, and W.C. Lineberger, *A study of the singlet and triplet states of vinylidene by photoelectron spectroscopy of $H_2C=C^-$, $D_2C=C^-$, and $HDC=C^-$. Vinylidene–acetylene isomerization.* Journal of Chemical Physics, 1989. **91**: p. 5974.

K.M. Ervin and W.C. Lineberger, *Photoelectron Spectroscopy of Negative Ions*, in *Advances in Gas Phase Ion Chemistry*, N.G. Adams and L.M. Babcock, Editors. 1992, JAI Press: Greenwich. p. 121-166.

K.M. Ervin, *PESCAL*. 2001: Reno, NV.

K.M. Ervin, T.M. Ramond, G.E. Davico, R.L. Schwartz, S.M. Casey, and W.C. Lineberger, *Naphthyl radical: Negative ion photoelectron spectroscopy, Franck-Condon simulation, and thermochemistry.* Journal of Physical Chemistry A, 2001. **105**(48): p. 10822-10831.

K.M. Ervin, *PESCAL, Fortran program.* 2003.

W.M.F. Fabian, V.A. Bakulev, and C.O. Kappe, *Pericyclic versus Pseudopericyclic 1,5-Electrocyclization of Iminodiazomethanes. An ab Initio and Density Functional Theory Study.* Journal of Organic Chemistry, 1998. **63**(17): p. 5801.

P. Fantucci, S. Polezzo, G. Morosi, and V. Valenti, *Valence-Only Model Potential Calculations on Copper Hydride Molecule.* Theoretica Chimica Acta, 1985. **67**(3): p. 245-253.

M.J. Frisch, G.W. Trucks, H.B. Schlegel, G.E. Scuseria, M.A. Robb, J.R. Cheeseman, J.A. Montgomery, Jr. , T. Vreven, K.N. Kudin, J.C. Burant, J.M. Millam, S.S. Iyengar, J. Tomasi, V. Barone, B. Mennucci, M. Cossi, G. Scalmani, N. Rega, G.A. Petersson, H. Nakatsuji, M. Hada, M. Ehara, K. Toyota, R. Fukuda, J. Hasegama, M. Ishida, T. Nakajima, Y. Honda, O. Kitao, H. Nakai, M. Klene, X. Li, J.E. Knox, H.P. Hratchian, J.B. Cross, C. Adamo, J. Jaramillo, R. Gomperts, R.E. Stratmann, O. Yazyev, A.J. Austin, R. Cammi, C. Pomelli, J.W. Ochterski, P.Y. Ayala, K. Morokuma, G.A. Voth, P. Salvador, J.J. Dannenberg, V.G. Zakrzewski, S. Dapprich, A.D. Daniels, M.C. Strain, O. Farkas, D.K. Malick, A.D. Rabuck, K. Raghavachari, J.B. Foresman, J.V. Ortiz, Q. Cui, A.G. Baboul, S. Clifford, J. Cioslowski, B.B. Stefanov, G. Liu, A. Liashenko, P. Piskorz, I. Komaromi, R.L. Martin, D.J. Fox, T. Keith, M.A. Al-Laham, C.Y. Peng, A. Nanayakkara, M. Challacombe, P.M.W. Gill, B. Johnson, W. Chen, M.W. Wong, C. Gonzalez, and J.A. Pople, *Gaussian 03, Revision B.05*. 2003, Gaussian, Inc.: Pittsburgh, PA.

R. Georgiadis, E.R. Fisher, and P.B. Armentrout, *Neutral and ionic metal-hydrogen and metal-carbon bond energies: reactions of cobalt, nickel, and copper with ethane, propane, methylpropane, and dimethylpropane.* Journal of the American Chemical Society, 1989. **111**(12): p. 4251-62.

A.J. Gianola, T. Ichino, R.L. Hoenigman, S. Kato, V.M. Bierbaum, and W.C. Lineberger, *Thermochemistry and Electronic Structure of the Pyrrolyl Radical.* J. Phys. Chem. A., 2004. **108**(46): p. 10326-10335.

A.J. Gianola, T. Ichino, R.L. Hoenigman, S. Kato, V.M. Bierbaum, and W.C. Lineberger, *Photoelectron Spectra and Ion Chemistry of Imidazolide.* J. Phys. Chem. A., 2005. **109**(50): p. 11504-11514.

A.J. Gianola, *Photoelectron Spectroscopy of Negative Ions*, in *Department of Chemistry and Biochemistry*. 2006, University of Colorado: Boulder.

A.J. Gianola, T. Ichino, S. Kato, V.M. Bierbaum, and W.C. Lineberger, *Thermochemical Studies of Pyrazolide.* J. Phys. Chem. A., 2006: p. (in press).

K.A. Gingerich, *Mass-spectrometric determination of the bond energies of the molecules AuS, BS, and BS$_2$.* Journal of the Chemical Society [Section] D: Chemical Communications, 1970(10): p. 580-1.

M.J. Griffiths and R.F. Barrow, *Observations On a $^2\Pi_i$ - X $^2\Pi_i$ Transition in Gaseous AgO.* Journal of Physics B, 1977. **10**(5): p. 925-930.

M.J. Griffiths and R.F. Barrow, *Observations on Electronic-Spectra of CuO AgO and AuO Isolated in Rare-Gas Matrices.* Journal of the Chemical Society-Faraday Transactions Ii, 1977. **73**: p. 943-951.

J.D. Grunwaldt and A. Baiker, *Gold/Titania Interfaces and Their Role in Carbon Monoxide Oxidation.* Journal of Physical Chemistry B, 1999. **103**: p. 1002 - 1012.

J.D. Grunwaldt, M. Maciejewski, O.S. Becker, P. Fabrizioli, and A. Baiker, *Comparative Study of Au/TiO$_2$ and Au/ZrO$_2$ Catalysts for Low-Temperature CO Oxidation.* Journal of Catalysis, 1999. **186**(2): p. 458 - 469.

H.M. Guardiola-Diaz, L.A. Foster, D. Mushrush, and A.D.N. Vaz, *Azole-antifungal binding to a novel cytochrome P450 from Mycobacterium tuberculosis: implications for treatment of tuberculosis.* Biochemical Pharmacology, 2001. **61**(12): p. 1463-1470.

M. Haruta, N. Yamada, T. Kobayashi, and S. Iijima, *Gold catalysis prepared by coprecipitation for low-temperature oxidation of hydrogen and of carbon monoxide.* Journal of Catalysis, 1989. **115**(2): p. 301 - 309.

M. Haruta, *Size- and support-dependency in the catalysis of gold.* Catalysis Today, 1997. **36**(1): p. 153 - 166.

P.J. Hay and R.L. Martin, *All-Electron and Valence-Electron Calculations On AgH, Ag$_2$, and AgO.* Journal of Chemical Physics, 1985. **83**(10): p. 5174-5181.

A. Hecq, M. Vandy, and M. Hecq, *Determination of Au$-$O bond energy by glow discharge mass spectrometry.* Journal of Chemical Physics, 1980. **72**(4): p. 2876 - 2878.

M. Hliwa, J.C. Barthelat, M. Pelissier, and F. Spiegelmann, *Calculation and Analysis of the Low-Lying Excited $^{3,1}\Sigma^+$ States of Copper Hydride.* Chemical Physics Letters, 1986. **132**(2): p. 205-208.

J. Ho, K.M. Ervin, and W.C. Lineberger, *Photoelectron-Spectroscopy of Metal Cluster Anions - Cu$_n^-$, Ag$_n^-$, and Au$_n^-$.* Journal of Chemical Physics, 1990. **93**(10): p. 6987-7002.

S. Hoyau and G. Ohanessian, *Complexation of small organic molecules by Cu$^+$*. Chemical Physics Letters, 1997. **280**(3,4): p. 266-272.

J. Hrusak, S. Ten-No, and S. Iwata, *Quadratic configuration interaction versus coupled-cluster theory: importance of orbital relaxation phenomena in CuH and CuF*. Journal of Chemical Physics, 1997. **106**(17): p. 7185-7192.

K. Huber and G. Herzberg, *Molecular Spectra and Molecular Structure, Constants of Diatomic Molecules*. 1979, New York: Van Nostrand-Reinhold.

E.P. Hunter and S.G. Lias, *Proton Affinity Evaluation*, in *NIST Chemistry WebBook, NIST Standard Reference Database Number 69*, P.J. Linstrom and W.G. Mallard, Editors. 2005, National Institute of Standards and Technology: Gaithersburg MD, 20899.

T. Ichino, A.J. Gianola, D.H. Andrews, and W.C. Lineberger, *Photoelectron Spectroscopy of AuO$^-$ and AuS$^-$*. Journal of Physical Chemistry A, 2004. **108**(51): p. 11307 - 11313.

G. Igel, U. Wedig, M. Dolg, P. Fuentealba, H. Preuss, H. Stoll, and R. Frey, *Cu and Ag As One-Valence-Electron Atoms - Pseudopotential CI Results For CuO and AgO*. Journal of Chemical Physics, 1984. **81**(6): p. 2737-2740.

C.N. Jarman, W.T.M.L. Fernando, and P.F. Bernath, *Further analysis of the ~B1A''-~X1A' system of copper hydroxide (CuOH) and copper deuteroxide (CuOD)*. Journal of Molecular Spectroscopy, 1990. **144**(2): p. 286-303.

C.N. Jarman, W.T.M.L. Fernando, and P.F. Bernath, *A to X CuOH system*. Journal of Molecular Spectroscopy, 1991. **145**: p. 151.

T. Joseph-Horne and D.W. Hollomon, *Molecular mechanisms of azole resistance in fungi*. Fems Microbiology Letters, 1997. **149**(2): p. 141-149.

S.A. Kaluzhina and G.V. Shatalov, *Triazole derivatives as inhibitors of general and thermogalvanic corrosion of iron in a 0.1N sulfuric acid solution. II. Effect of triazole derivatives on thermogalvanic corrosion of iron in a 0.1N sulfuric acid solution*. 1975, Voronezh. Gos. Univ.,Voronezh,USSR. p. 9 pp.

A. Kant and K.A. Moon, *Dissociation energies of gaseous copper, silver, gold, and nickel hydrides*. High Temperature Science, 1979. **11**(1): p. 55-62.

V.V. Karasiev, *Parameter-free local exchange and Pade approximation for correlation: application to diatomic molecules*. Theochem, 1999. **493**: p. 21-28.

V. Kello and A.J. Sadlej, *Electron correlation and relativistic effects in the coinage metal compounds. I. The coinage metal hydrides*. Theoretica Chimica Acta, 1995. **92**(4): p. 253-67.

V. Kello and A.J. Sadlej, *The change of picture of the Hellmann-Feynman force operator in approximate relativistic methods*. Theochem, 2001. **547**: p. 35-53.

V. Kelloe and A.J. Sadlej, *Quadrupole moments of copper hydride, silver hydride, and gold hydride (CuH, AgH, and AuH). A study of the electron-correlation and relativistic effects.* Journal of Chemical Physics, 1991. **95**(11): p. 8248-53.

V. Kelloe and A.J. Sadlej, *Standardized basis sets for high-level correlated relativistic calculations of atomic and molecular electric properties in the spin-averaged Douglas-Kroll (no-pair) approximation. Part 1. Groups Ib and IIb.* Theoretica Chimica Acta, 1996. **94**(2): p. 93-104.

V. Kelloe, A.J. Sadlej, and B.A. Hess, *Relativistic effects on electric properties of many-electron systems in spin-averaged Douglas-Kroll and Pauli approximations.* Journal of Chemical Physics, 1996. **105**(5): p. 1995-2003.

H. Kusama, M. Kurashige, and H. Arakawa, *Influence of nitrogen-containing heterocyclic additives in I-/I3- redox electrolytic solution on the performance of Ru-dye-sensitized nanocrystalline TiO2 solar cell.* Journal of Photochemistry and Photobiology, A: Chemistry, 2005. **169**(2): p. 169-176.

D.G. Leopold, K.K. Murray, A.E. Stevens-Miller, and W.C. Lineberger, *Methylene: A study of the $X\,^3B_1$ and a $^1A_1$ states by photoelectron spectroscopy of CH_2^- and CD_2^-.* Journal of Chemical Physics, 1985. **83**: p. 4849.

Z.P. Liu, P. Hu, and A. Alavi, *Catalytic role of gold in gold-based catalysts: A density functional theory study on the CO oxidation on gold.* Journal of the American Chemical Society, 2002. **124**(49): p. 14770-14779.

F.W. Loomis and T.F. Watson, *Band Spectra of AgO and CuO.* Physical Review, 1935. **48**: p. 280-282.

N. Lopez and J.K. Norskov, *Catalytic CO oxidation by a gold nanoparticle: A density functional study.* Journal of the American Chemical Society, 2002. **124**(38): p. 11262-11263.

C.M. Marian, *Theoretical study of the spectra of CuH and CuD.* The Journal of Chemical Physics, 1991. **94**(8): p. 5574.

C.M. Marian, *Theoretical study of the spectra of copper hydride and copper deuteride (CuH and CuD).* Journal of Chemical Physics, 1991. **94**(8): p. 5574-85.

M.C. McCarthy and R.W. Field, *Frequency-modulation enhanced magnetic rotation spectroscopy of PdH, PdD, NiH, and CuH.* Journal of Chemical Physics, 1994. **100**(9): p. 6347-58.

M. Merchan, J.P. Daudey, R. Gonzalez-Luque, and I. Nebot-Gil, *On the dissociation energy of the copper dimer and copper hydride (CuH) using a differential correlation approach.* Chemical Physics, 1990. **148**(1): p. 69-76.

J. Micanko and S. Biskupic, *Relativistic and correlation study of coinage metal hydrides.* ACH - Models in Chemistry, 2000. **137**(5-6): p. 753-766.

N. Minh Tho, M.A. McGinn, and N.J. Fitzpatrick, *A theoretical characterization of some diatomic copper species.* Journal of the Chemical Society, Faraday Transactions 2: Molecular and Chemical Physics, 1986. **82**(9): p. 1427-43.

F. Misaizu, K. Tsukamoto, M. Sanekata, and K. Fuke, *Photoelectron spectroscopy of mass-selected metal-water cluster negative ions: Cu-(H2O)n and Na-(H2O)n.* Surface Review and Letters, 1996. **3**(1): p. 405-410.

C.E. Moore, *Atomic Energy Levels.* NSRDS-NBS. 1952, Washington: US GPO Circular No. 467.

F. Muntean, M.S. Taylor, A.B. McCoy, and W.C. Lineberger, *Femtosecond study of Cu(H_2O) dynamics.* The Journal of Chemical Physics, 2004. **121**: p. 5676.

M.E. Nadal, P.D. Kleiber, and W.C. Lineberger, *Photofragmentation of mass-selected ICl^- $(CO_2)_n$ cluster ions: Solvation effects on the structure and dynamics of the ionic chromophore.* The Journal of Chemical Physics, 1996. **105**(2): p. 504 - 514.

A. Nakajima, T. Taguwa, K. Nakao, K. Hoshino, S. Iwata, and K. Kaya, *Photoelectron spectroscopy of binary-metal cluster anions containing sulfur atom.* Surface Review and Letters, 1996. **3**(1): p. 417-421.

D.M. Neumark, K.R. Lykke, T. Andersen, and W.C. Lineberger, *Laser Photodetachment Measurement of the Electron Affinity of Atomic Oxygen.* Physical Review A, 1985. **32**(3): p. 1890-1892.

NIST, NIST Chemistry Webbook, NIST Standard Reference Database Number 69, June 2005 Release.
.

L.C. O'Brien, S.J. Wall, and M.K. Sieber, *Fourier transform spectroscopy of the $A\ ^2\Sigma^+ - X$ $^2\Pi_i$ transition of AgO.* Journal of Molecular Spectroscopy, 1997. **183**(1): p. 57-60.

L.C. O'Brien, S.J. Wall, and G.L. Henry, *The $A\ ^2\Sigma^+ - X\ ^2\Pi_i$ (0, 1) band and reanalyses of the blue and ultraviolet transitions of AgO.* Journal of Molecular Spectroscopy, 1998. **191**(1): p. 218-220.

L.C. O'Brien, S.C. Hardimon, and J.J. O'Brien, *Spectroscopy of AuO: Identification of the $^2\Pi_{1/2}$ to $X\ ^2\Pi_{3/2}$ Transition.* Journal of Physical Chemistry A, 2004. **108**(51): p. 11302 - 11306.

J. Onoe, H. Nakamatsu, T. Mukoyama, R. Sekine, H. Adachi, and K. Takeuchi, *Relativistic change in bond overlap population for the study of relativistic effect on bond length of diatomic molecules.* Journal of the Physical Society of Japan, 1996. **65**(8): p. 2459-2462.

J. Onoe, *Atomic-number dependence of relativistic effects on chemical bonding.* Advances in Quantum Chemistry, 2001. **37**: p. 311-323.

C. Opitz and H.H. Dunken, *Extended Hueckel calculations for first-period transition-metal hydroxides.* Zeitschrift fuer Physikalische Chemie (Leipzig), 1972. **249**(3-4): p. 154-60.

M. Pelissier, J.P. Daudey, J.P. Malrieu, and G.H. Jeung, *The electronic structure of transition metal atoms and diatoms through pseudopotential approaches.* NATO ASI Series, Series C: Mathematical and Physical Sciences, 1986. **176**(Quantum Chem.: Challenge Transition Met. Coord. Chem.): p. 37-51.

K.S. Pitzer, *Relativistic Effects on Chemical Properties.* Accounts of Chemical Research, 1979. **12**(8): p. 272-276.

M.L. Polak, M.K. Gilles, J. Ho, and W.C. Lineberger, *Photoelectron Spectroscopy of CuO⁻.* Journal of Physical Chemistry, 1991. **95**(9): p. 3460-3463.

L.A. Posey, M.J. DeLuca, and M.A. Johnson, *DEMONSTRATION OF A PULSED PHOTOELECTRON SPECTROMETER ON MASS-SELECTED NEGATIVE IONS O⁻, O₂⁻, AND O₄⁻.* Chemical Physics Letters, 1986. **131**(3): p. 170 - 174.

R. Pou-Amerigo, M. Merchan, I. Nebot-Gil, P.A. Malmqvist, and B.O. Roos, *The chemical bonds in CuH, Cu₂, NiH, and Ni₂ studied with multiconfigurational second order perturbation theory.* Journal of Chemical Physics, 1994. **101**(6): p. 4893-902.

P. Pyykko and J.P. Desclaux, *Relativity and the Periodic System of Elements.* Accounts of Chemical Research, 1979. **12**(8): p. 276-281.

P. Pyykko, *Relativistic Effects in Structural Chemistry.* Chemical Reviews, 1988. **88**(3): p. 563-594.

D. Radisic, S.J. Xu, and K.H. Bowen, *Photoelectron spectroscopy of the anions, CH3NH- and (CH3)(2)N- and the anion complexes, H-(CH3NH2) and (CH3)(2)N-(CH3)(2)NH).* Chemical Physics Letters, 2002. **354**(1-2): p. 9-13.

K. Raghavachari, K.K. Sunil, and K.D. Jordan, *Theoretical study of the bonding in copper(I) hydride and copper dimer (Cu₂).* Journal of Chemical Physics, 1985. **83**(9): p. 4633-40.

T.M. Ramond, G.E. Davico, R.L. Schwartz, and W.C. Lineberger, *Vibronic structure of alkoxy radicals via photoelectron spectroscopy.* The Journal of Chemical Physics, 2000. **112**(3): p. 1158.

T.M. Ramond, *Negative Ion Photoelectron Spectroscopy of Alkyl Peroxides, Alkoxides, and Group VIII Transition Metal Oxides*, in *Department of Physics.* 2001, University of Colorado: Boulder. p. 237.

T.M. Ramond, G.E. Davico, F. Hellberg, F. Svedberg, P. Salen, P. Soderqvist, and W.C. Lineberger, *Photoelectron spectroscopy of nickel, palladium, and platinum oxide anions.* Journal of Molecular Spectroscopy, 2002. **216**(1): p. 1 - 14.

V.M. Rao, M.L.P. Rao, and P.T. Rao, *Dissociation energy of the ground state of the copper(I) hydride molecule.* Journal of Quantitative Spectroscopy & Radiative Transfer, 1981. **25**(6): p. 547-9.

G.J. Rathbone, T. Sanford, D. Andrews, and W.C. Lineberger, *Photoelectron imaging spectroscopy of $Cu^-(H_2O)_{1,2}$ anion complexes.* Chemical Physics Letters, 2005. **401**(4-6): p. 570-574.

G. Rauhut, *Modulation of reaction barriers by generating reactive intermediates: double proton transfer reactions.* Physical Chemistry Chemical Physics, 2003. **5**(5): p. 791-800.

P.J. Renders and T.M. Seward, *The stability of hydrosulfido- and sulfido-complexes of gold(I) and silver(I) at 25 DegC.* Geochimica et Cosmochimica Acta, 1989. **53**(2): p. 245-53.

U. Ringstroem, *New band system of copper hydride in the far ultraviolet.* Canadian Journal of Physics, 1968. **46**(20): p. 2291-300.

U. Ringstrom, *On the spectra of copper hydride and copper deuteride.* Arkiv For Fysik, 1966. **32**: p. 211.

S.M. Rothstein, *Valence energy in variational Monte Carlo: CuH dissociation energy.* International Journal of Quantum Chemistry, 1996. **60**(4): p. 803-808.

T.J. Sanford, *Photodissociation Dynamics and Photoelectron Imaging Spectroscopy of Anions and Anion Clusters*, in *Department of Chemistry and Biochemistry*. 2004, Colorado: Boulder. p. 212.

A. Sanov, T. Sanford, S. Nandi, and W.C. Lineberger, *Spin-orbit relaxation and recombination dynamics in $I_2^-(CO_2)_n$ and $I_2^-(OCS)_n$ cluster ions: A new type of photofragment caging reaction.* The Journal of Chemical Physics, 1999. **111**(2): p. 664 - 675.

P. Schwerdtfeger, M. Dolg, W.H.E. Schwarz, G.A. Bowmaker, and P.D.W. Boyd, *Relativistic effects in gold chemistry. I. Diatomic gold compounds.* Journal of Chemical Physics, 1989. **91**(3): p. 1762 - 1774.

J.M. Seminario, A.G. Zacarias, and J.M. Tour, *Molecular Alligator Clips for Single Molecule Electronics. Studies of Group 16 and Isonitriles Interfaced with Au Contacts.* Journal of the American Chemical Society, 1999. **121**: p. 411 - 416.

G. Simons and E.R. Talaty, *FSGO model for core d electrons: Optimized structures for third row hydrides.* Journal of Chemical Physics, 1977. **66**(6): p. 2457-61.

D.F. Smith, G.R. Graybill, R.K. Grubbs, and J.A. Gucinski, *New developments in very high rate silver oxide electrodes.* Journal of Power Sources, 1997. **65**(1-2): p. 47-52.

J.R. Smith, J.B. Kim, and W.C. Lineberger, *High-Resolution Threshold Photodetachment Spectroscopy of OH^-.* Physical Review A, 1997. **55**: p. 2036.

H. Smithson, C.A. Marianetti, D. Morgan, A. Van der Ven, A. Predith, and G. Ceder, *First-principles study of the stability and electronic structure of metal hydrides.* Physical Review B: Condensed Matter and Materials Physics, 2002. **66**(14): p. 144107/1-144107/10.

S. Smoes, F. Mandy, A. Vander Auwera-Mahieu, and J. Drowart, *Determination by the mass-spectrometric Knudsen cell method of the dissociation energies of the Group IB chalcogenides.* Bulletin Des Societes Chimiques Belges, 1972. **81**(1-2): p. 45-56.

J.F. Stanton, J. Gauss, J.D. Watts, M. Nooijen, N. Oliphant, S.A. Perera, P.G. Szalay, W.J. Lauderdale, S.A. Kucharski, S.R. Gwaltney, S. Beck, A. Balková, D.E. Bernholdt, K.K. Baeck, P. Rozyczko, H. Sekino, C. Hober, and R.J. Bartlett, *ACES II*, R.J. Bartlett, Editor. 2006, Quantum Theory Project, University of Florida.

J.F. Stanton, T. Ichino, A.J. Gianola, and W.C. Lineberger, *Nonadiabatic effects in the photoelectron spectrum of the pyrazolide anion: Three-state interactions of the pyrazolyl radical.* 2006.

T. Steimle, M. Tanimoto, K. Namiki, and S. Saito, *The millimeter wave spectrum of silver monoxide, AgO.* Journal of Chemical Physics, 1998. **108**(18): p. 7616-7622.

E. Stenz, G. Menzel, and G. Schuster, *Effect of triazoles on DNA- and RNA-containing bacteriophages and their hosts.* Mikrobiologicheskii Zhurnal (1978-1993), 1980. **43**(2): p. 239-42.

J. Sugar and A. Musgrove, *Energy Levels of Copper, Cu I through Cu XXIX.* Journal of Physical and Chemical Reference Data, 1990. **19**: p. 527.

E. Surber, R. Mabbs, and A. Sanov, *Probing the Electronic Structure of Small Molecular Anions by Photoelectron Imaging.* Journal of Physical Chemistry A, 2003. **107**(40): p. 8215 - 8224.

T. Suzumura, T. Nakajima, and K. Hirao, *Ground-state properties of MH, MCl, and M_2 (M = Cu, Ag, and Au) calculated by a scalar relativistic density functional theory.* International Journal of Quantum Chemistry, 1999. **75**(4/5): p. 757-766.

M.S. Taylor, F. Muntean, W.C. Lineberger, and A.B. McCoy, *A theoretical and computational study of the anion, neutral, and cation $Cu(H_2O)$ complexes.* The Journal of Chemical Physics, 2004. **121**: p. 5688.

M.S. Taylor, J. Barbera, C.-P. Shulz, F. Muntean, A.B. McCoy, and W.C. Lineberger, *Femtosecond Dynamics of $Cu(H_2O)_2$.* The Journal of Chemical Physics, 2005. **122**: p. 05431.

C. Toernkvist, J. Bergman, and B. Liedberg, *Geometry and vibrations of the 1,2,3-triazole anion. A theoretical and experimental study.* Journal of Physical Chemistry, 1991. **95**(8): p. 3119-23.

C.W. Tornoe, S.J. Sanderson, J.C. Mottram, G.H. Coombs, and M. Meldal, *Combinatorial Library of Peptidotriazoles: Identification of [1,2,3]-Triazole Inhibitors against a*

Recombinant Leishmania mexicana Cysteine Protease. Journal of Combinatorial Chemistry, 2004. **6**(3): p. 312-324.

R.E. Trifonov, I. Alkorta, V.A. Ostrovskii, and J. Elguero, *A theoretical study of the 1,2,3-triazolo-iminodiazomethane isomerism in the gas phase.* Heterocycles, 2000. **52**(1): p. 291-302.

U. Uhler, *On the Band Spectra of Silver Oxide.* Arkiv For Fysik, 1953. **7**(12): p. 125-147.

M. Valden, X. Lai, and D.W. Goodman, *Onset of Catalytic Activity of Gold Clusters on Titania with the Appearance of Nonmetallic Properties.* Science, 1998. **281**(5383): p. 1647 - 1650.

C. van Wullen, *Molecular density functional calculations in the regular relativistic approximation: method, application to coinage metal diatomics, hydrides, fluorides and chlorides, and comparison with first-order relativistic calculations.* Journal of Chemical Physics, 1998. **109**(2): p. 392-399.

T.D. Varberg and K.M. Evenson, *The pure rotational spectra of CuH and CuD in their ground states measured by tunable far-infrared spectroscopy.* Journal of Molecular Spectroscopy, 1994. **164**(2): p. 531-5.

R. Vianello and Z.B. Maksic, *Acidities of azoles in the gas phase and in DMSO: an ab initio and DFT study.* Molecular Physics, 2005. **103**(2-3): p. 209-219.

B.R. Vujisic, J.J. Savovic, V. Bojovic, and D.S. Pesic, *Blue (a − X) System of AgO ($Ag^{107}O^{18}$) Molecule.* Spectroscopy Letters, 1993. **26**(8): p. 1529-1535.

S. Wang, A. Paul, N.J. DeYonder, Y. Yamaguchi, and H.F. Shaefer, *The ground and two lowest-lying singlet excited electronic states of copper hydroxide (CuOH).* The Journal of Chemical Physics, 2005. **123**: p. 014313.

X.-B. Wang, L.-S. Wang, R. Brown, P. Schwerdtfeger, D. Schroder, and H. Schwarz, *The electronic structure of $CuCl_2$ and $CuBr_2$ from anion photoelectron spectroscopy and ab initio calculations.* The Journal of Chemical Physics, 2001. **114**(17): p. 7388.

X. Wang and L. Andrews, *Gold is noble but gold hydride anions are stable.* Angewandte Chemie, International Edition, 2003. **42**(42): p. 5201-5206.

X. Wang, L. Andrews, L. Manceron, and C. Marsden, *Infrared Spectra and DFT Calculations for the Coinage Metal Hydrides MH, $(H_2)MH$, MH_2, M_2H, M_2H^-, and $(H_2)CuHCu$ in Solid Argon, Neon, and Hydrogen.* Journal of Physical Chemistry A, 2003. **107**(41): p. 8492-8505.

E.P. Wigner, *On the behavior of cross sections near thresholds.* Physical Review, 1948. **73**: p. 1002-1009.

W.C. Wiley and I.H. McLaren, *Time-of-flight mass spectrometer with improved resolution.* Journal of Mass Spectrometry, 1997. **32**(1): p. 4-11.

R.B. Wright, J.K. Bates, and D.M. Gruen, *Matrix-isolation spectroscopy of aluminum, copper, and nickel hydrides and deuterides produced in a hollow-cathode discharge.* Inorganic Chemistry, 1978. **17**(8): p. 2275-8.

Z.J. Wu, *Density Functional Study of AuX^q (X = O, S, Se, Te, q = +1, 0, -1) Molecules.* Journal of Physical Chemistry A, 2005. **109**(26): p. 5951-5955.

C. Yang and Z.Y. Meng, *Side-Chain Alkylation of Para-Xylene With Methanol On Alkali Cation Zeolites.* Applied Catalysis, 1991. **71**(1): p. 45-54.

C. Zhang and A. Alavi, *First-Principles Study of Superabundant Vacancy Formation in Metal Hydrides.* Journal of the American Chemical Society, 2005. **127**(27): p. 9808-9817.

Z. Zhou, R. Liu, J. Wang, S. Li, M. Liu, and J.-L. Bredas, *Intra- and Intermolecular Proton Transfer in 1H(2H)-1,2,3-Triazole Based Systems.* Journal of Physical Chemistry A, 2006. **110**(7): p. 2322-2324.

T. Ziegler, V. Tschinke, and A. Becke, *Theoretical study on the relative strengths of the metal-hydrogen and metal-methyl bonds in complexes of middle to late transition metals.* Journal of the American Chemical Society, 1987. **109**(5): p. 1351-8.

_____

Appendix A. Detector Chamber Vacuum Interlock System

_____

After photoelectron velocity map imaging capability was added to the pulsed source instrument described in chapter 2, it became clear that a smart vacuum interlock was needed. Because the imaging microchannel plates require two days of conditioning if the pressure rises above $1x10^{-6}$ torr, a vacuum interlock system was designed and built to prevent the detector region from venting due to short power or cooling water outages, while still venting in the event of a vacuum accident. The system monitors the turbo roughing pump line pressure, cooling water flow rate, and building AC power. The roughing line pressure is monitored by set point of a thermocouple gauge, the water flow rate is monitored from a flow meter in the cooling water line, and the building AC power is monitored via a standard two pronged plug. The interlock box receives its power from an uninterruptible power supply (UPS) and distributes it to the turbo pump controller, turbo pump rough valve, and the turbo pump vent valve. The operation of the system is laid out in the flow chart in Figure A.1, with the interlock code presented at the end. What follows are two procedures. The first is the procedure to turn off the turbo pump and vent the detection region, while the second is the procedure to pump the system down and reset the interlock.

The procedure to properly vent the detection chamber is very simple. First, make sure that there is plenty of pressure in the nitrogen vent cylinder and that it is supplying gas to the vent line. Change the number of minutes the system will run off of the UPS to "1", then unplug the AC sensor. The system will close the roughing valve, wait ~ 1 minute, turn off power to the turbo pump controller, wait ~ 15 minutes for the turbo pump to slow down, then open the vent valve. The system should take about 20 minutes to vent. In order to close the

vent valve, remove the vent valve power plug from the interlock socket and insert into building power outlet.

The procedure for pumping down the detection region is as follows. If the system has vented due to a fault (bad power, bad pressure, bad cooling water), fix the cause of the fault. Be sure that the vent valve power plug is inserted into the corresponding outlet in the back panel of the interlock box. Also be sure that the power button on the turbo pump controller is in the off position. Enable the "override" switch on the front panel of the interlock box. Toggle the "reset" switch also found on the front panel. At this point the system will close the vent valve, open the turbo rough line valve, and supply power to the turbo pump controller. Wait until the pressure of the turbo pump rough line, as read on the thermocouple gauge controller, is well below the set point (currently 100 mTorr). Note that this may take as long as 25 minutes. Press and hold the turbo pump controller power button for 3 – 4 seconds until the pump starts (as evidenced by the RPM meter increasing). The pressure in the turbo pump roughing line will increase and may briefly go above the set point, but should decrease in a short amount of time (less than one minute). Once the turbo rough line pressure is well below the set point, disable the override switch. The system is now in its normal state.

A.1   Detection region interlock flowchart

"start"

The initial power-on mode of the interlock is to check the turbo backing line pressure (Press), AC power (AC), and water flow (H_2O). If any are bad, the corresponding LED is illuminated and the program will continue to illuminate the LED until it is good. When Press, AC, and H2O are good, the program proceeds to "start". The "start" routine monitors PRESS, AC, and H2O at ~ 1 kHz, and is the normal (everything is fine) state of the interlock.

```
           Press  ──Bad──▶  Go to "close"
             │
            Good
             │
             ▼
           H₂O  ──Bad──▶  Go to "H2O"
             │
            Good
             │
             ▼
           AC  ──Bad──▶  Go to "noAC"
             │
           Good
```

"close"
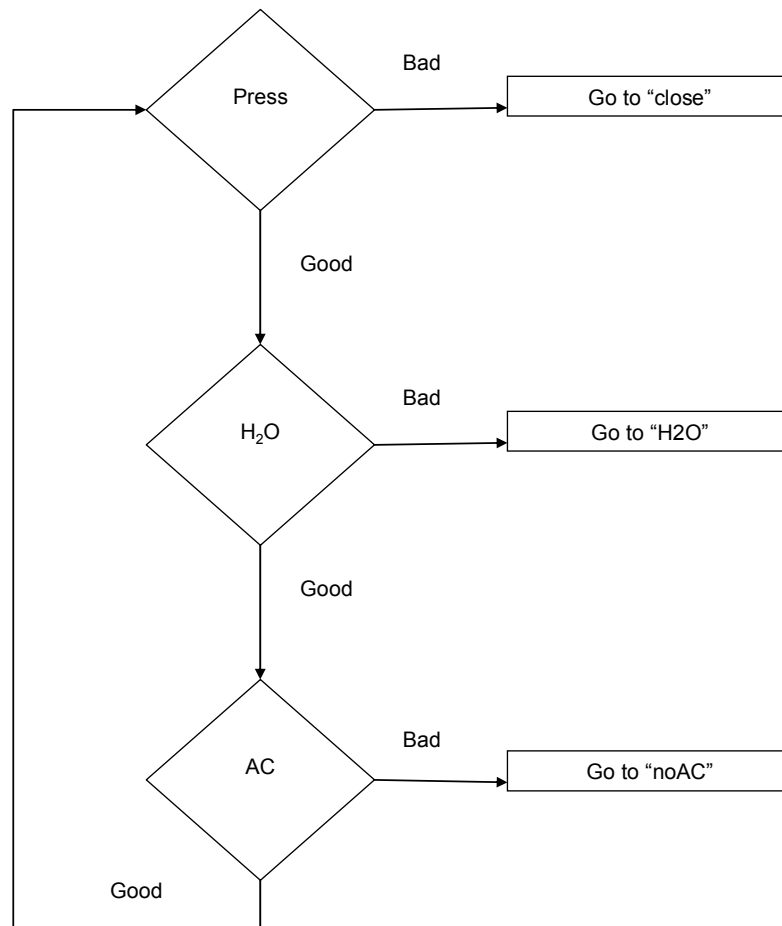
Notes:

- This sub-routine is to determine if pressure is high because of AC off, or vacuum accident

- If vacuum accident, goes to immediate shut-down ("PRfail")

AC

Bad → Go to "noAC"

Good

Go to "PRfail"
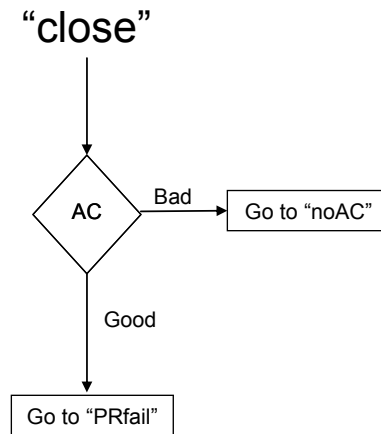
"H2O"

Notes

Checking pressure and power while waiting 15 min for water to come back

After 15 min, checks water again: if it is good, then back to normal mode. If it is not, then goes into water fail mode.

Press — Bad → Go to "close"

Press — Good

AC — Bad → Go to "noAC"

AC — Good

15 min? — NO

15 min? — YES

H_2O — Bad → Go to "H2Ofail"

H_2O — Good

Go to "start"

"noAC"

```
Close Rough Valve
        │
        ▼
   Wait 1 min  ◄──────────────┐
        │                     │
        ▼                     │ Yes
       AC ──Bad──► # Bad ─────┘
        │          ACs <
      Good         T1?  ──No──► Go to "ACfail"
        │
        ▼
   Wait T2 min
        │
        ▼
      Press ──Bad──► Wait T2 ──► Press ──Bad──► Go to "PRbad2"
        │             min          │
      Good                       Good
        │                          │
        ▼                          ▼
       AC ──Bad──► Go to "ACfail"  AC ──Bad──► Go to "ACfail"
        │                          │
      Good                         │
        │                          │
        ▼                          │
   Wait T2 min ◄───────────────────┘
        │
        ▼
      Press ──Bad──► Go to "PRbad2"
        │
      Good
        │
        ▼
       AC ──Bad──► Go to "ACfail"
        │
      Good
        │
        ▼
   Open rough
     valve
        │
        ▼
  Go to "start"
```

Notes

• Checks AC every minute for number of minutes read from front panel T1

• If AC still bad, then shuts down via "ACfail"

• If AC is back, then waits for turbo rough line to pump down

• Two consecutive good pressure reads are necessary to make sure that rough line pressure is well below the TC gauge set point.

"PRfail"
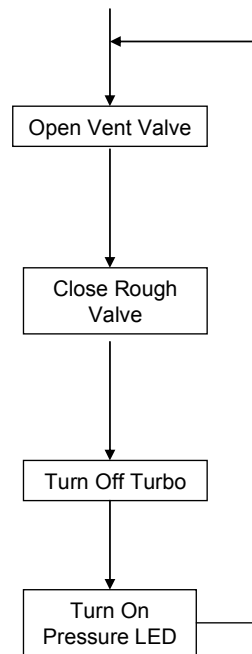
Note:

•Vacuum accident assumed

•No delays

"ACfail"

```
                    ┌──────────────┐
                    │ Turn Turbo Off│
                    └──────────────┘
                           │
                           ▼
                    ┌──────────────┐
                    │  Turn On AC  │
                    │     LED      │
                    └──────────────┘
                           │
                           ▼
                    ┌──────────────┐
                    │  Wait T3 min │
                    └──────────────┘
                           │
                           ▼
                    ┌──────────────┐
                    │  Open Vent   │
                    │    Valve     │
                    └──────────────┘
```
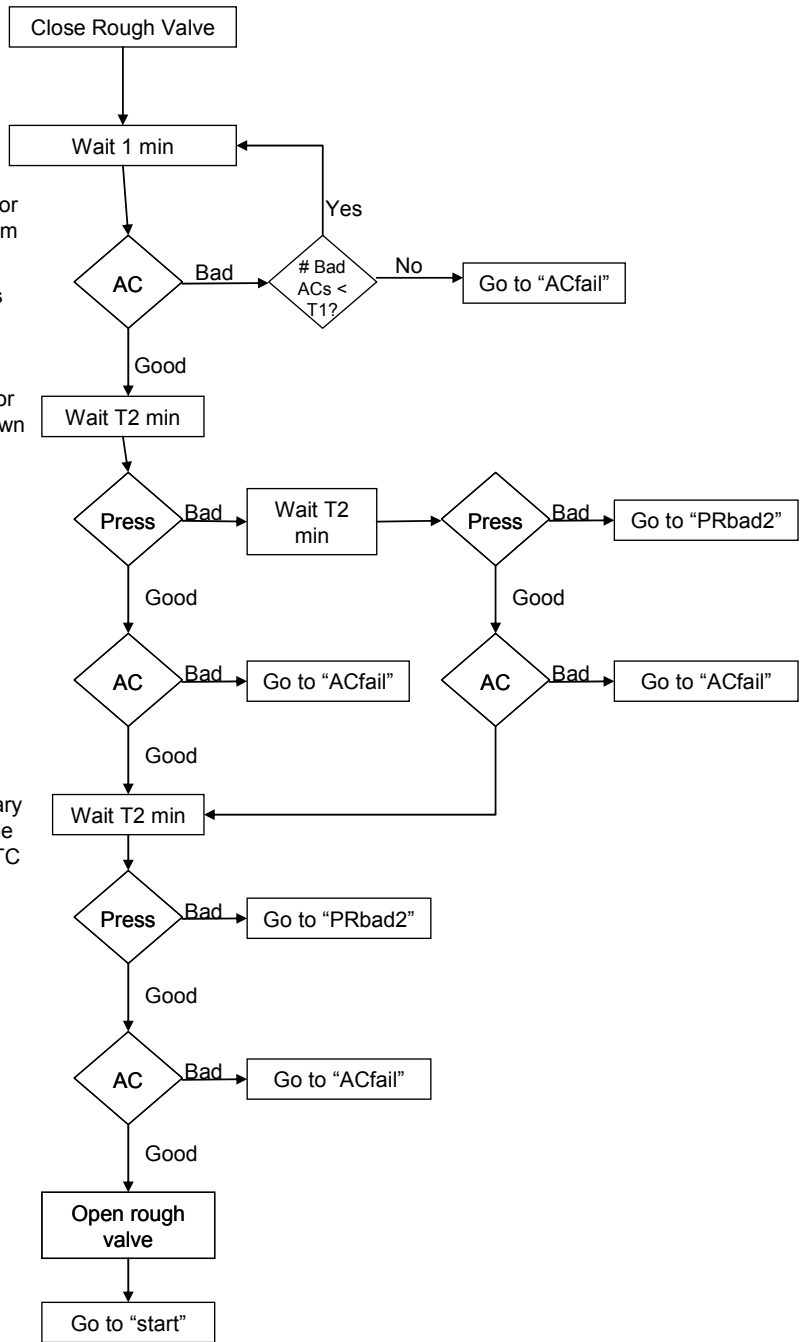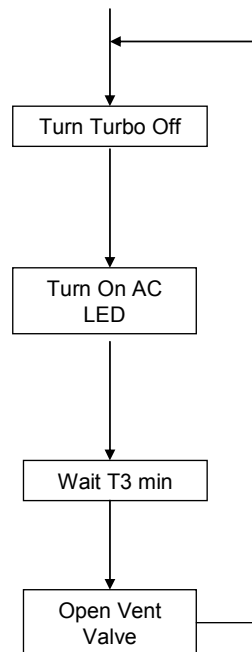
Note:

•Caused by AC off longer than T1 (on front panel)

"PRbad2"
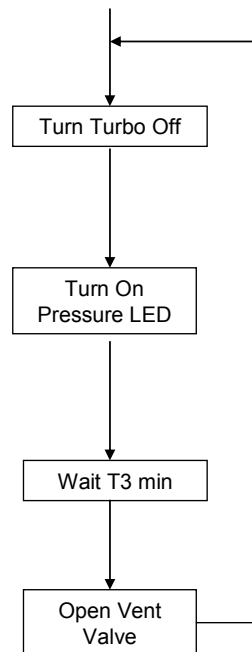
Note:

•Caused by AC outage less than T1, but pressure still high

"H2Ofail"

```
        ┌──────────────┐
        │ Turn Turbo Off │◄──────┐
        └──────┬───────┘         │
               │                 │
        ┌──────▼───────┐         │
        │  Turn On AC  │         │
        │     LED      │         │
        └──────┬───────┘         │
               │                 │
        ┌──────▼───────┐         │
        │  Wait T3 min │         │
        └──────┬───────┘         │
               │                 │
        ┌──────▼───────┐         │
        │  Open Vent   │─────────┘
        │    Valve     │
        └──────────────┘
```
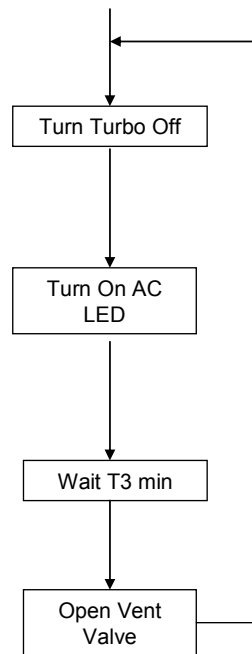
Note:

•Caused by H2O off longer than 15 min

```
;==================LC045V2.ASM============12/15/2004
;
;Configuration Bits
;
;Oscillator RC
;Watchdog Timer Off
;Power Up Timer On
;Brown Out Detect Off
;Low Voltage Program Disabled
;Flash Program Write Write Protection Off
;Background Debug Disabled
;Data EE Read Protect Off
;Code Protect Off
;
;
;
;LC045
;
;this programme reads 2 BCD numbers on Port B and C
;uses them to set time delays for a turbo pump interlock
;
;
;
;
;-----------------------------------------------------
list p=16f873a
radix hex
;-----------------------------------------------------
; cpu equates memory map
optionr equ 0x81
status equ 0x03
rp0 equ 0x05
rp1 equ 0x06
rbpu equ 0x07
adcon1 equ 0x9f
trisa equ 0x85
trisb equ 0x86
trisc equ 0x87
porta equ 0x05
portb equ 0x06
```

```
portc equ 0x07
lobyte equ 0x20
hibyte equ 0x21
times equ 0x22
t equ 0x23
N equ 0x24
NN equ 0x25
T1 equ 0x26 ;Time on Front Panel in minutes
T2 equ 0x27 ;Time between pressure checks after power outage induced
Pressure fault
T3 equ 0x28 ;Time for Turbo Pump to spin down
;--------------------------------------------------------
;setup I/O
bsf status, rp0 ;switch to bank 1
bcf optionr,rbpu ;pullups on port B
movlw 0x06 ;configure port A as digital i/o
movwf adcon1
movlw 0x38
movwf trisa ;A0:A2 outputs, A3:A5 inputs
movlw 0xff
movwf trisb ;port B inputs
clrw
movwf trisc ;port C outputs
bcf status,rp0 ;switch back to bank 0
;
;--------------------------------------------------------
;
movlw 0x07
movwf portc ;turn on "fail" LED's
bcf porta,0x02 ;vent valve LO = open
bcf porta,0x01 ;roughing valve LO = closed
bcf porta,0x00 ;Turbo Pump LO = off
;
;------------T1, T2, T3--------------------
;
call READT1 ;get T1 value
movlw 0x01 ;value to be loaded into T2
movwf T2 ;T2 = 1
movlw 0x0f ;value to be loaded into T3
movwf T3 ;T3 = 15
```

```
;
;initial checks
;
begin movlw 0x03
movwf times ;set times = 3
;
;check pressure
;
btfss porta,0x04 ;is bit 4 HI, HI => GOOD
goto badPR ;
bcf portc,0x02 ;turn off LED
decf times,1
goto ckH2O
badPR bsf portc,0x02 ;turn on LED
;check H2O
;
ckH2O btfss porta,0x05 ;is bit 5 HI, HI => GOOD
goto badH2O ;
bcf portc,0x00 ;turn off LED
decf times,1
goto ckAC
badH2O bsf portc,0x00 ;turn on LED
;
;check AC
;
ckAC btfss porta,0x03 ;is bit 3 HI
goto badAC ;
bcf portc,0x01 ;turn off LED
decfsz times
goto begin
goto GOOD
badAC bsf portc,0x01 ;turn on LED
goto begin
;
;
;
;
;
;
;
;
;
;
;
```

```
GOOD bsf porta,0x02 ;vent valve HI = closed
bsf porta,0x01 ;roughing valve HI = open
bsf porta,0x00 ;Turbo Pump HI = on
;
;check pressure
;
start btfss porta,0x04 ;is bit 4 HI, HI => GOOD
goto close ;close RV
;
;check H2O
;
btfss porta,0x05 ;is bit 5 HI, HI => GOOD
goto H2O ;
;
;check AC
;
btfss porta,0x03 ;is bit 3 HI, HI => GOOD
goto noAC
goto start
;
;close roughing valve
;
close bcf porta,0x01 ;close roughing valve
;
;check AC line
;
btfss porta,0x03 ;is bit 3 HI
goto noAC ;power failure
goto PRfail ;power good
noAC bcf porta,0x01 ;close roughing valve
;start T1 timer
movf T1,0
movwf times
;
wait btfsc porta,0x03 ;check AC
goto ACgood ;if AC good
call MINUTE
decfsz times,1
goto wait
btfss porta,0x03 ;if T1 set to 1
```

```
        goto ACfail
;
;if power good
;
ACgood movf T2,0
movwf times
delay1 call MINUTE ;wait T2 minutes
decfsz times,1
goto delay1
;
btfss porta,0x04 ;check pressure
goto PRbad1
btfss porta,0x03 ;check AC
goto ACfail
;
PRgood movf T2,0
movwf times
delay2 call MINUTE ;wait T2 minutes
decfsz times,1
goto delay2
;
btfss porta,0x04 ;check pressure
goto PRbad2
btfss porta,0x03 ;check AC
goto ACfail
;
;open roughing valve
;
bsf porta,0x01 ;set portA bit 1 HI
;
goto start ;go back to normal operation
;
PRbad1 call MINUTE ;wait 2 minutes
call MINUTE
btfss porta,0x04 ;check pressure
goto PRbad2
btfss porta,0x03 ;check AC
goto ACfail
goto PRgood
;15 minute loop, 900 seconds
```

```
;
H2O
movlw 0x5b ;5b hex is 91
movwf t ;t = 91
loopA
decfsz t,1
goto tensec ;do it 90 times = 1 mimute
goto ckH20
tensec movlw 0x65 ;65h = 101, 10 second delay
movwf N
loopB ;do it 100 times
decfsz N,1
goto tenth
goto loopA
tenth movlw 0x42 ;0.1 sec delay, this value good for 10K, 0.01uF
movwf NN
loopC
btfss porta,0x04 ;check pressure
goto close
btfss porta,0x03 ;check AC
goto noAC
decfsz NN,1
goto loopC
goto loopB
;
;
;
ckH20 btfss porta,0x05
goto H2Ofail
goto start
;
H2Ofail bcf porta,0x01 ;close Roughing Valve
movf T3,0
movwf times
bcf porta,0x00 ;PORTA 0 => LO turn off TP
bsf portc,0x00 ;turn on H2O fail LED
loopX call MINUTE ;wait T3 minutes
decfsz times
goto loopX
bcf porta,0x02 ;open Vent Valve
goto H2Ofail
```

```
;
ACfail movf T3,0 ;wait time for Vent Valve to colse
movwf times
bcf porta,0x00 ;PORTA 0 => LO turn off TP
bsf portc,0x01 ;turn on AC fail LED
loopY call MINUTE ;wait T3 minutes
decfsz times
goto loopY
bcf porta,0x02 ;open Vent Valve
goto ACfail
;
PRfail bcf porta,0x00 ;PORTA 0 => LO
bcf porta,0x02 ;open Vent Valve
bsf portc,0x02 ;turn on PRESSURE fail LED
goto PRfail
;
PRbad2 movf T3,0 ;wait time for Vent Valve to colse
movwf times
bcf porta,0x00 ;PORTA 0 => LO turn off TP
bsf portc,0x02 ;turn on PRESSURE fail LED
loopZ call MINUTE ;wait T3 minutes
decfsz times
goto loopZ
bcf porta,0x02 ;open Vent Valve
goto PRbad2
;SUBROUTINE READT1, reads value on PORT B
;
READT1
movf portb,w ;read port B to W
movwf lobyte ;data in lobyte
movwf hibyte ;data in hibyte
swapf hibyte ;swap bits 0-3 for 4-7
comf lobyte ;complement these bits since switches in 02 and 03
comf hibyte ;are the complement to that of 01, see project notes
movlw 0x0f ;load w = 00001111
andwf lobyte ;clear upper 4 bits
andwf hibyte ;clear upper 4 bits
movlw 0x9 ;multiply hi byte by 10
movwf times ;load times with multiplier-1
movf hibyte,w ;load w with hi byte
```

```
mult1 addwf hibyte ;add hibyte to initial value and store
decfsz times ;is times=0
goto mult1 ;no, do again, hibyte=hibyte*multiplier
movf hibyte,w ;hibyte to w
addwf lobyte,w ;add w to lobyte
movwf T1 ;result in T1
return
;
;
;
;subroutine MINUTE, delays for 60 seconds
;
;
MINUTE
movlw 0x3d ;3d hex is 61
movwf t ;t = 61
loop1
decfsz t,1
goto second ;do it 60 times = 1 mimute
return
second movlw 0x0b ;1 second delay
movwf N
loop2 ;do it 10 times
decfsz N,1
goto inner
goto loop1
inner movlw 0x42 ;0.1 sec delay, this value good for 10K, 0.01uF
movwf NN
loop3
decfsz NN,1
goto loop3
goto loop2
;
;
end
```